Martínez Carmena, Alfonso (2023) *Vortex flows around morphing foils: reshape yourself to effect a change.* PhD thesis.

https://theses.gla.ac.uk/83534/

VORTEX FLOWS AROUND MORPHING FOILS:

reshape yourself to effect a change

Alfonso Martínez Carmena
School of Engineering
University of Glasgow

A dissertation submitted for the degree of
Doctor of Philosophy

April 2023

Declaration

I hereby declare that the work contained in this dissertation is my own except when specific reference is made to the work of others. The content has not been previously submitted, in whole or in part, for consideration for any other academic degree in the University of Glasgow or any other university.

I further declare that images included in this dissertation whose copyright I do not own, but of which I have obtained permission to show here, are not used by myself anywhere else than in the present document.

Alfonso Martínez Carmena
April 2023

Abstract

The unsteady production of vorticity is a unifying principle in biological locomotion in air and water. Shape-tailoring their aerodynamic/hydrodynamic surfaces, natural flyers/swimmers switch with ease between regimes of attached and separated flow. Modern engineering tries to mimic this shape control ability in applications such as micro air vehicles and oscillating energy harvesting devices. Owing to the complexity of morphing, fundamental research merits further efforts, to provide a clearer view of the link between shape variation and unsteady flow response.

In this dissertation, classical theories (potential flow) are combined with numerical methods (vortex methods) in the development of a physics-based low-order model to simulate complex unsteady flows around foils undergoing large camber variations, as a first step towards exploring the capability of camber morphing to alter vortex characteristics, like formation time and strength. Discrete-vortex methods have risen as one of the most suitable numerical tools to establish a relation between camber definition, flow characteristics and aerodynamic loads produced, involving a reasonably low number of parameters. An existing discrete-vortex model for rigid foils is extended to variable-camber foils. A time-varying chord line is proposed, where the boundary condition in thin-aerofoil theory is to be satisfied. This enables large deformations of the camber line to be modelled. Computational fluid dynamics simulations at Reynolds numbers of $\mathcal{O}(10^4)$ are used to test the performance of the model. Furthermore, a new method is introduced to determine the rate at which vorticity is fed into leading-edge vortices in vortex models. The strength of nascent particles at the leading edge is here computed with the velocity at the edge of the shear layer, formulated in terms of the leading-edge suction parameter (an inviscid parameter from unsteady thin-aerofoil theory). This novel formulation allows post-separation flow behaviour, like vortex sheets dynamics, to be correctly captured. Finally, morphing and vortex modelling are combined to demonstrate the potential of this technique to affect leading-edge vortices: the amount of vorticity produced at the leading edge is modulated by suitably tailoring the shape of the camber line.

This research aims to advance our theoretical understanding of the correlation between prescribed deflection at the trailing edge and alteration of flow properties at the leading edge, of interest to the design of flow control strategies inspired by nature.

To the authors of incomplete
or forgotten works

Preface

A few years back, when this journey was still to begin, I was lucky enough to access part of the original Marqués de Saudade's poetic work. Diving for days among poems of the highest literary complexity, I came across what would turn out to be the most precise, yet simple, reflection of what I was to feel the years to come. As if those neat fountain pen strokes were foreshadows of the thoughts I'd have by the time of this writing:

> *"No obstante lo que he gozado*
> *y lo mucho que he sufrido,*
> *por sentir lo que no he dado*
> *apenas sé si he vivido."*

Words that, fully aware of my limitations in dressing with the musicality they were originally endowed with, and at risk of depriving them of their enormous evoking power, I dare to translate for the reader by putting my best effort, for they portray with the finest exactness and lucidity antagonistic feelings I had once and again doing research:

> *No matter how much joy*
> *or pain I undergo,*
> *for feeling I shared not*
> *if I lived fully, I hardly know.*

Passion, suffering, and a scientific responsibility of sharing knowledge have cohabited during the last four years, shaping the personality of he who presents this doctoral dissertation, what a beautiful coincidence, on St Andrew's Day, Scotland's official national day. Aiming to make the reading as enjoyable as possible (within what allows the complexity of mathematics), the elaboration of this text bears the mark of passion, hoping not to have lost technical rigour as a result. May this feeling linger ...

November 2022, Edinburgh
A.M.C.

Acknowledgements

Kiran Ramesh, this journey through the fascinating field of unsteady aerodynamics would have never started if not for the chance you gave me to be part of your research group, for which I am truly grateful. I am also thankful for the theoretical and technical knowledge provided during the initial steps, and the trust placed on me to continue with greater freedom at the end.

Karen Mulleners, I would like to thank you chiefly for the opportunity of joining UNFoLD for a few months, with all the benefits this entailed, such us the snow trip! On the academic side, your orderly method of research is a lesson well worth learning. I enjoyed those discussions over a coffee, and appreciate suggestions made to stimulate my scientific thinking. I hope many more will follow.

Lola Sondesa, in a world where external pressure constantly tempts us to stray from our beliefs, it is difficult to find who does not. I see in you one of those people, and your unnoticed actions remind me this is something worth fighting for, even when it sometimes brings a certain loneliness. Thank you for your example.

Hugh Bird, besides being research colleagues you have been the role model for me. Your attitude as a researcher is exemplary, always prioritising integrity over any need to show "nice" results. A value all good researchers ought to have. I am indebted to you for having selflessly read through the entire first draft of the manuscript, giving valuable suggestions to improve the work.

Alex, Pedro, I wish to acknowledge my debt to you, for your astonishing ability to detect typos that have now been corrected. Any other that might have been overlooked in the final version is my sole responsibility. Thomas, I also thank you for your tips on the post-processing of some figures that have enhanced the final appearance greatly.

Christopher, thanks should also go to you, for having periodically monitored my writing progress, helping to keep the pace going when the countdown began.

Karishma, Hassam, Isa, Julio, Shuji, all this would have been much harder without your support. Having to deal with your own PhDs you perfectly knew how to empathise, so that the process was much more bearable. I am deeply grateful to you and hope you received the same from me.

Thank you UNFoLD group, for providing me with a well-balanced working environment, where the habitual banter atmosphere proved fully compatible with

daily commitment to research, for your contagious enthusiasm showing your experimental rigs, and for so many answers gave to satiate my curiosity. It made the mobility an unforgettable experience, and I'll cling fondly to these memories.

Andy, we met the very first week of our PhD studies, you heard me saying thanks countless times since and I will do it many more. Your generosity and optimistic view of life are inspiring. How fortunate was I to deal with admin paperwork with perfect timing! I hope we keep adding anecdotes from our getaways to the Highlands for years on end.

Alber, sometimes words fall short to express our gratitude. Still, this is the time for having precluded my mind from straying in such a long mental race, being proud during the highs and supportive during the lows. My Jiminy Cricket, like many times before!

León, Ako, Alvarito, and the rest of the family and friends, not even the thousands of kilometres between all of us manage to make one lose the feeling of being home... As great as the distance among us is my thankfulness!

Madre, having taught me with your example the importance of sacrifice in life made the tread much easier during this 4-years journey. But the truth is that this lesson goes with me beyond this trip, it is everlasting, like my gratitude.

Padre, your curiosity for everything in life triggered my own from a very young age. My admiration for natural flight was raised from all those summers grabbing a pair of binoculars to go bird-watching with you as a child (and we still do it). I'm not sure I ever thanked you expressly for that, and although you know how grateful I am now I want to remind you of it. Thinking of it, perhaps this had to do somehow with my decision to pursue research studies on unsteady aerodynamics...

To all of you: me getting to this point is also very much your doing. Thank you!

I would be careless in not mentioning the members of my examination committee, Andrea Da Ronch and Hossein Zare-Behtash, for an invaluable last feedback to give the dissertation its very final form. Also, academic staff from the University of Glasgow: Julia Deans, for having resolved a myriad of administrative doubts; Richard Green and Euan McGookin, for constructive remarks as external reviewers on my annual progress.

I also wish to express my sincere gratitude to Albert Medina, for happily sharing the geometric measures of the model and experimental data used for validation.

Finally, I would like to extend my acknowledgement to the Engineering and Physical Sciences Research Council (EPSRC), the College of Science and Engineering at the University of Glasgow and the Unsteady flow diagnostics laboratory (UNFoLD) at EPFL, for financial support to: this research project (grant number EP/N509668/1), a research mobility and a conference attendance, respectively.

Contents

Appendices

List of Figures

List of Tables

Nomenclature

ACRONYMS

AUV	Autonomous underwater vehicles
CFD	Computational fluid dynamics
DSV	Dynamic-stall vortex
DTEF	Dynamic trailing-edge flap
DVM	Discrete-vortex method
HV	Hinge vortex
LDVM	LESP-modulated discrete-vortex method
LESP	Leading-edge suction parameter
LEV	Leading-edge vortex
LOM	Low-order model
MAV	Micro aerial vehicle
MDVM	Morphing discrete-vortex model
SVDVM	Shear-layer velocity discrete-vortex model
TEV	Trailing-edge vortex
UTAT	Unsteady thin-aerofoil theory

GREEK SYMBOLS

α	pitch angle
$\dot{\alpha}$	pitch rate
α_0	complex pitch amplitude for harmonic motion
α_δ	angle of attack variation due to flap deflection
α_{eff}	effective angle of attack

β	flap deflection angle (Chapter 4 only)
β_0	complex flap deflection amplitude for harmonic motion
γ_0	quasi-steady vortex sheet strength
γ_B	bound vortex sheet strength
γ_{c0}	circulatory vortex sheet strength due to motion
γ_n	non-circulatory vortex sheet strength
γ_w	wake-induced circulatory vortex sheet strength
Γ_B	bound vortex circulation
Γ_i	i-th vortex particle strength
$\dot{\Gamma}_{LE}$	leading-edge vorticity feeding rate
Γ_{LEV}	leading-edge vortex circulation
Γ_{TEV}	trailing-edge vortex circulation
δ	flap deflection angle
$\dot{\delta}$	flap deflection rate
δ_{max}	flap deflection amplitude
η	normal coordinate in body frame of reference
$\eta(\xi)$	chordwise distribution of camber in body frame of reference
η_{pvt}	normal coordinate of pivot point in body frame of reference
θ	transformation variable
θ_f	trigonometric coordinate of the hinge
λ_{sl}	slope of separated shear layer at the leading edge
ξ	chordwise coordinate in body frame of reference
ξ_{hg}	chordwise coordinate of hinge in body frame of reference
ξ_{LE}	chordwise coordinate of leading edge in body frame of reference
ξ_{pvt}	chordwise coordinate of pivot point in body frame of reference
ξ_{TE}	chordwise coordinate of trailing edge in body frame of reference
ϕ	velocity potential; phase between plunge and pitch motions
ϕ_B	velocity potential from bound vorticity
ϕ_{LEV}	velocity potential from leading-edge vorticity
ϕ_{TEV}	velocity potential from trailing-edge vorticity
ψ	phase between plunge motion and flap deflection

ω	angular frequency
ω_z	out-of-plane vorticity (in CFD)

LATIN SYMBOLS

a	non-dimensional coordinate of pitch axis in Theodorsen's theory
$A_0\,, \dots, A_n$	Fourier coefficients
b	half chord length in Theodorsen's theory
c	foil total chord length
c_a	foil's fore element chord length
c_{eff}	foil effective chord length
c_f	flap chord length
c_{pvt}	distance from leading edge to pivot axis
C_D	drag coefficient
C_L	lift coefficient
C_M	pitching moment coefficient
C_N	normal force coefficient
C_S	suction force coefficient
d	average spacing between vortex blobs
$f(k), g(k)$	complex functions of the reduced frequency
$\dot{h}$	plunge rate
h_0	complex plunge amplitude for harmonic motion
k	reduced frequency (harmonic), $k = \frac{\omega c}{2U}$
K_α	reduced pitch rate (ramp), $K_\alpha = \frac{\dot{\alpha} c}{2U}$
K_δ	reduced flap deflection rate (ramp), $K_\delta = \frac{\dot{\delta} c}{2U}$
$L_1\,, L_2$	logarithmic terms
$\mathcal{L}$	leading-edge suction parameter
$p(\xi)$	surface pressure distribution
$Q_n(k)$	wake coefficients
r_{LE}	leading-edge radius
Re	chord Reynolds number, $Re = \frac{\rho U c}{\mu}$

$S(k)$	Sears function
St	Strouhal number, $St = \frac{fA}{U}$
St_{δ}	Strouhal number in terms of bending parameters
$\mathcal{S}_{\beta}$	scale factor for flap motion
t	time
Δt	time step
t^*	non-dimensional time, $t^* = \frac{tU}{c}$
t^*_{LEV}	non-dimensional time of vortex growth
Δt^*	non-dimensional time step, $\Delta t^* = \frac{\Delta t U}{c}$
T	period of harmonic motion
u_{ind}	horizontal vortices-induced velocity in inertial frame
u_{LE}	leading-edge velocity
u_x	horizontal disturbance velocity in inertial frame
u_z	vertical disturbance velocity in inertial frame
U	forward velocity
U_{∞}	free stream velocity
U_{ref}	reference velocity
v_{η}	normal velocity in body frame
v_{ξ}	chordwise velocity in body frame
v_{core}	vortex-blob core radius
V_t	tangential velocity
w_{ind}	vertical vortices-induced velocity in inertial frame
W	local downwash
$\tilde{x}$	non-dimensional chordwise coordinate in Theodorsen's theory

MATH SYMBOLS

$\dot{\bullet}$	time derivative
$\Re$	real part of a complex function

The pleasure lies not in discovering truth, but in searching for it.

— Leo Tolstoy

1

INTRODUCTION

Hundreds of millions of years ago (the fossil age of the evolutionarily oldest species of the extant dragonflies), the benefits of unsteady aerodynamics seemed to be already known for some. In the course of natural evolution, since the first creatures left the ground to stay aloft, flyers have been constantly adapting the morphology and functionality of their winged systems (Alexander, 2015). Their mastery of flight, performing acrobatic manoeuvres which baffle the human eye, made them a source of admiration to mankind since prehistoric times, witnessed on $11,000$ years old cave drawings (Videler, 2006).

Nonetheless, the fascination for winged creatures alone, not walking hand in hand with a proper understanding of the underlying flow physics, has hampered humanity's attempts to embrace the true potential of unsteady aerodynamics. Despite some theoretical endeavours made a century ago (Birnbaum, 1924), the complex features of flapping wings (Shyy et al., 2013) have eluded scientific research until the last half of the 20th century. With the advent of high-speed cameras and other modern techniques for unsteady flow diagnosis, the mystery of flapping flight began to be unveiled (Ellington et al., 1996), revitalising a long-standing hankering to mimic those nimble movements on man-made flight devices.

Efforts in this direction are now blooming with the emergence of new flight technologies, like Micro Aerial Vehicles (MAVs), ideal candidates for emergency situations: to scour areas in search and rescue of missing people without risking human lives, specially across tricky terrain or hazardous environments; or goods delivery in remote places where time is of the essence. Regarding the former application, the rugged terrain of Scotland's natural landscapes is one of the easiest for hikers to go astray or get stranded in. In 2020 alone, Scottish Mountain Rescue received 671 call-outs (Carrell, 2022). Small unmanned vehicles have the potential to reduce risk in these perilous operations. Their role is foreseen to grow further as technology advances and aspects of natural flight such as morphing are incorporated into MAVs. This control technique would allow them to withstand unsteady flow conditions like the wet and gusty weather prevailing in the Scottish Highlands. The usage in the latter scenario was accelerated by the coronavirus outbreak. When COVID-19 struck, emergency supplies (medical equipment and samples) were distributed to isolated locations in Scotland, like the Isle of Mull, helping to bolster the healthcare system capacity to cope with the pandemic (Neate, 2020).

Another sector that benefited greatly from unsteady flows is that of renewable energy. The race for planet decarbonisation, aspiring to eventually eliminate carbon dioxide emissions to the atmosphere, has put the spotlight on clean energy. Potential renewable resources to look at are water and air. Tidal and wind power play a key role in regions with favourable geographical conditions in terms of strong winds and tidal currents. Such is the case of Scotland, whose marine area alone contains 25% of Europe's tidal energy resource. Its most important contribution is the Pentland Firth and Orkney Waters, where some of the fastest tidal stream currents in the world are observed, exceeding 5m/s (Murray & Gallego, 2017). It is here where unsteady flows can lead oscillating energy harvesting devices to sustainably harness tidal power, decreasing the environmental impact.

Unsteady aerodynamics is seeing important advancements. Still, some of its enigmatic nature will endure through time, and natural flyers will keep deftly outmanoeuvring any human-made attempt of small scale flight... or perhaps not?

1.1 Motivation

The benefits of mimicking flapping motion notwithstanding, unsteadiness can sometimes pose a problem rather than give a solution. Unsteady flow fields are characterised by extremely rapid changes, including the formation of vortices due to the moving body or external agents. Whilst the well-known Leading-Edge Vortex (LEV) plays a significant role in lift enhancement for small flappers, and improved performance for oscillating energy harvesters, it also is responsible for a strong non-linear relationship between the kinematics and the forces generated. This can result in highly dynamic loading on the immersed structure, which at best can deteriorate the performance of the device, and at worst can compromise its structural integrity, rendering it useless to fulfil the mission for which it was conceived.

Given the disparate impact of these time-varying flows an improved understanding of unsteady aerodynamics is fundamental, and so is the ability to obtain rapid predictions of flow behaviour. The requirement of almost instantaneous results makes time-consuming analysis tools, such as Computational Fluid Dynamics (CFD) simulations or experiments, impractical. A promising course of action is the development of Low-Order Models (LOMs): the flow physics is distilled into easier problems which are solved with aerodynamic theories. Geometries are simplified and flow properties modelled are reduced to the bare minimum needed. This enables real time flow and force predictions, and allows understanding of the fundamental phenomena at play.

The numerous factors contributing to unsteady flow conditions, from wing kinematics (pitch, plunge or surge motions), through morphing (chordwise, spanwise or sweep angle), to external disturbances (gusts, turbulence or neighbour bodies), renders any endeavour to model all possible combinations unthinkable within the scope of a doctoral dissertation. To complicate matters further, three-dimensional effects can also be important sources of unsteadiness. Because of the very complex nature of the problem, in a bid to simplify the analysis this dissertation restricts itself to two-dimensional flows. To aid gaining a clearer view of some key contributions to flow development and force evolution of unsteady aerodynamics at low Reynolds

Figure 1.1: Natural flyer (from ardmoth.org) and its bionic peer (from www.festo.com).

numbers, only pitch motions of a foil and its temporal camber variations are studied in this thesis.

The long term goal of this research is to characterise vortex dynamics in response to morphing wings. To this end, the main objectives of the dissertation are:

- To develop a low-order model to simulate unsteady flows past deforming foils.
- To explore the capacity of temporal camber variations in altering characteristics of vortex structures like formation time and strength.

The fundamental nature of the work presented here is believed to provide a more thorough vision of the underlying principles of camber morphing, and to serve as a solid basis for the design of unsteady flow control strategies that mimic the capabilities of natural flyers, hoping to see one day their bionic peers aloft (Fig. 1.1).

Having introduced the reasons motivating this research, the state of the art is presented in the following chapter. The research questions sought to be answered are highlighted, and novel contributions from this work in that direction are listed, along with their location within the main text.

Do not go where the path may lead, go instead where there is no path and leave a trail.

— R.W. Emerson

2

BACKGROUND

FLUIDS in nature are continuously subjected to dynamic phenomena. Numerous disciplines of science study these events (Lugt, 1983). Among them, unsteady aerodynamics deals with the formation and development of vortices around aerodynamic surfaces in motion or subjected to flow disturbances.

2.1 Unsteady flows: Leading-edge vortex

The complex flow field of unsteady fluid problems is characterised by rapid changes in circulation bound to the lifting surface, and non-linear phenomena such as flow separation and shedding of vortex structures. The degree of unsteadiness of a fluid problem is generally determined by a parameter known as reduced frequency, $k = \frac{\omega c}{2U}$, that relates oscillatory and linear velocities in the fluid. It was introduced a century ago by Birnbaum (1924).

The impact that unsteady flows produce on immersed bodies can be poles apart: while the formation of vortices can bring a great benefit to biological and bio-inspired manoeuvring (Polet et al., 2015); and the extraction of energy by harnessing environmental vortices can reduce the cost of propulsive locomotion (Liao et al., 2003); possible detrimental effects in man-made technologies, if these varying flows are uncontrolled, range from minor loss of efficiency to violent vibrations and mechanical failure. Thus, the control of unsteady flows has become a topic of great interest for modern aerospace engineering.

2.1.1 Rotary wings

An in depth insight into the physics underlying unsteady flow separation is owed to a phenomenon known as dynamic stall, and a broad body of literature on the matter is available, stemmed especially from investigations in the rotorcraft community, since this phenomenon was identified over the blades of helicopter rotors and has been a major concern since. Aerodynamic bodies undergoing time-dependent motions (pitching, plunging) can delay the onset of stall to incidences far beyond their static stall limits (McCroskey, 1982). The distinctive feature of this process is the formation of a strong vortex at the leading edge, the Dynamic-Stall Vortex (DSV). As the angle of attack increases, a free shear layer forms in the vicinity of the leading edge and rolls-up into a vortex. During this dynamic process the vortex is being fed by the shear layer, building in strength and increasing its size. At some point the vortex has covered the entire chord length of the aerofoil and detaches from the leading edge convecting into the wake (McCroskey, 1981). A boost in lift force is experienced while the DSV remains attached to the aerofoil, but the downstream convection of the vortex produces an aft movement of the centre of pressure, which results in large nose-down pitching moment, and is followed by a large drop in lift when the vortex is shed, marking the onset of unsteady flow separation.

In the same manner, vorticity is produced at the trailing edge induced by the downstream convecting DSV, giving rise to another vortex swirling in the opposite sense, the Trailing-Edge Vortex (TEV), which is also shed into the wake. The alternately vortex shedding process leads to a pattern of counterrotating vortices over the wake, known as the von Kármán vortex street. In accordance with this phenomenon aerodynamic loads oscillate. These undesirable load fluctuations are a limiting factor to the operation of rotary wings, since they are responsible for material fatigue and structural damage. Thence the importance of developing effective control mechanisms that modulate its occurrence and widen the operational

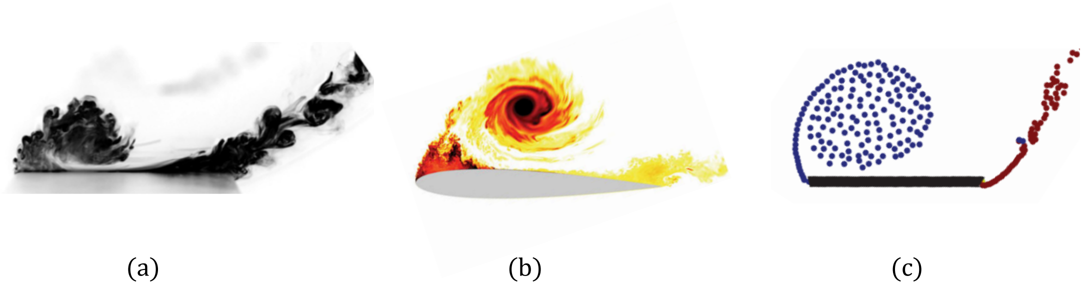
(a) (b) (c)

Figure 2.1: Leading-edge vortex visualisation: (*a*) experiment, (*b*) computational fluid dynamics and (*c*) discrete-vortex model. Images are rotated to present the profile in a horizontal position. Adapted from Benton and Visbal (2019), Granlund et al. (2013), and Ramesh et al. (2014) with permission.

range of these aeronautical systems. On these grounds, diverse semi-empirical methods to predict and model dynamic stall have been developed, such as the well-known model by Leishman (2006).

In consistency with the motion of rotor blades, the majority of research carried out on unsteady foils by that time was mainly focused on oscillatory pitch kinematics with low reduced frequencies at medium to high Reynolds numbers ($\mathcal{O}(10^5)$ to $\mathcal{O}(10^7)$).

2.1.2 Flapping wings

The failure of conventional aerodynamic theories to explain flapping-wing flight prompted the quest for unsteady mechanisms which improve its performance. Biologists revealed that insect flight relied, among others, on unsteady flow separation and associated formation of a strong leading-edge vortex (Ellington et al., 1996). Natural flyers have flaunted their ability to enhance high lift by means of several aerodynamic mechanisms for which there is documented evidence (Sane, 2003; J. Wang, 2005): the clap and fling (Lighthill, 1973; Maxworthy, 1979; Weis-Fogh, 1973), the Kramer effect (Sane & Dickinson, 2002), the wake capture (Birch & Dickinson, 2003; Dickinson et al., 1999; Lehmann et al., 2021), or the leading-edge vortex (Chin & Lentink, 2016; Shyy & Liu, 2007).

Among these mechanisms, the LEV is arguably the most common, and responsible to a large degree for the success of low Reynolds number flapping flight. There are records of its appearance in the flight of all major extant flying taxa: from insects (Bomphrey et al., 2005; Bomphrey et al., 2009; Fuchiwaki et al., 2013; Srygley & Thomas, 2002; Thomas et al., 2004; Willmott et al., 1997); to birds (Muijres et al., 2012; Videler et al., 2004; Warrick et al., 2009); and bats (Muijres et al., 2008). Records cover almost the whole spectrum of flight regimes: from hovering (Swanton et al., 2010; Van Den Berg & Ellington, 1997; Warrick et al., 2009), and slow flight (Muijres et al., 2012; Muijres et al., 2014), to cruising flight (Hubel & Tropea, 2010). The relatively high angle of attack at which the wing operates in these situations promotes flow separation at the leading edge. When this flow reattaches before the trailing edge an LEV is formed (see Fig. 2.1 for LEV visualisation through various techniques). Were it not for this vortex, not enough lift would be generated in flow regimes dominated by strong viscosity effects, which make the generation of lift and thrust challenging. Other than over flapping wings, examples of this unsteady phenomenon are found in fish (Borazjani & Daghooghi, 2013; Bottom II et al., 2016) and rotating plant seeds (Lentink et al., 2009).

The acknowledged benefit these vortices confer to biological flight has given a big impetus to the design of highly-manoeuvrable small-scale aerial vehicles which aim to favourably exploit unsteady flows (Ajanic et al., 2022; Chang et al., 2020; Colorado et al., 2012; Jafferis et al., 2019). Research carried out on dynamic stall until the arrival of these technologies was considered sufficient to illustrate its behaviour. However, unlike rotary-wing mechanisms, flapping-wing systems operate at low Reynolds numbers ($\mathcal{O}(10^2)$ and $\mathcal{O}(10^4)$) and high dimensionless rates of motion (Shyy et al., 2008). Although the characteristic sequence of events observed during the physical process of flow separation and LEV formation is generally shared by most unsteady aerofoils, a thorough examination of the literature reveals the sensitivity of vortex features to the type of motion performed, as well as several parameters involved: amplitude of motion, reduced frequency, Reynolds number (Carr, 1988; Mulleners & Raffel, 2013). Faster motions bring about larger pressure gradients and flow speeds, which results in stronger LEVs formed on aerofoils operating at these flight regimes. If further progress is to be made in the design of applications involving unsteady motions, like MAVs (Mueller, 2001) or oscillating energy harvesting devices, a better comprehension of the viscous flow evolution over the aerofoil under these conditions is needed. Thence the increasing number of studies on the flow physics underlying flapping flight (Akkala & Buchholz, 2017; Ford & Babinsky, 2013; Kissing et al., 2020; Rival et al., 2014; Widmann & Tropea, 2015).

Due to the growing interest in controlling LEV dynamics, either to stabilise the vortex and benefit from its temporary boost in lift, or to mitigate transients in gust encounters, the development of mathematical models is sought after which, by distilling complex unsteady flow problems into simpler ones, allow to capture the essential physics of LEVs in a more tractable way (Eldredge & Jones, 2019; Manar & Jones, 2019).

2.2 Discrete modelling of fluids: Vortex methods

The dynamic behaviour of unsteady flows can be analysed through the evolution of vorticity fields. Continuous distributions of vorticity, like separated shear layers or vortices, can be represented by finite arrays of computational elements which carry a discrete concentration of vorticity. A full description of the flow field is possible by tracking the motion and deformation of these discrete elements according to their local velocities, which includes the free stream velocity and those induced by other vortices through the Biot–Savart's law. This is the basis of Discrete-Vortex Methods (DVMs). Extensive reviews on the subject are found in Cottet and Koumoutsakos (2000) and Spalart (1988).

These numerical methods have the capacity to inform on the physics they aim to reproduce. Contrary to grid-based Euler methods, such as high-fidelity CFD, vortex methods are grid-free, which means there is no need to discretise the entire fluid domain, reducing considerably the computational burden of calculating flow properties at every point of the grid. Instead, the computational effort is concentrated on features of greater interest, such as vortices (flow field regions with non-zero vorticity). This adaptability to sudden changes in flow conditions makes Lagrangian methods ideal for analysis of external unsteady aerodynamics, justifying their application to simulate separated flows.

2.2.1 Steady flow separation

The fundamental problem of two-dimensional vortex sheets was a logical choice for the first studies on the matter. In the 1930's Rosenhead (1931) investigated the break up of a surface of discontinuity owing to instability, and subsequent formation of vortices, by placing a number of point vortices equally spaced along its trace and with the same strength. Several endeavours to numerically compute vortex sheet dynamics in two dimensions arose after his ground-breaking research with varying degrees of success. Moore (1971) and Takami (1964) applied the point vortex approximation to the vortex sheet roll-up process, but did not observe any spiral structure as previous studies managed to achieve, instead vortices moved chaotically, casting a doubt on the validity of results. In an attempt to provide an explanation to such discrepancies between investigations, Chorin and Bernard (1973) conjectured that limited accuracy on pre-computer calculations might act as a smoothing mechanism that obviates the singular character of point vortices, which would otherwise induce unbounded velocities, making them inappropriate to approximate bounded velocity fields. He proved the smoothing effect of numerical error applied to the roll-up of free vortex sheets.

A natural next step in the study of vortex sheet dynamics was the problem of flow separation and vortex shedding over bluff bodies. On this regard, Sarpkaya (1968) applied these methods to predict the development of symmetric flow separation about a circular cylinder immersed in an impulsively started uniform flow. Assumptions about the separation point over this geometry are necessary, for which he hypothesised the point bisecting the feeding zone into the shear layer to be the physical point of separation. To eliminate the need for assumptions about the location of flow separation, and also to avoid dealing with the difficult treatment of oscillating separation points, Clements (1973) considered a squared cylinder. Having right-angle corners, this shape fixes the location from where vortices are introduced into the flow field. He was then capable of predicting the asymmetric interaction of shear layers and the resultant steady vortex shedding.

Notable success was later achieved for inclined flat plates, yet in steady motion. In the manner in which Clements (1973) dealt with the interaction of vortex sheets, Kuwahara (1973) looked at the case of a flat plate at high incidence. The use of the Kutta condition allowed him to fix the position from where the nascent vortices emerged. He further showed that small variation of these points could strongly affect the normal force coefficient. In a later study Sarpkaya (1975) noticed the importance of the oscillation of the position from where vortices enter the flow field to the continuation of oscillations in the drag force. By allowing this point to vary in time, he claimed to have removed the difficulties arising from the use of the Kutta condition. He further computed the vorticity shedding rate by averaging the instantaneous velocities of the first four elements. These studies were complemented with work by Kiya and Arie (1977).

The focus was then moved to more streamlined geometries, with Katz (1981) studying flow separation on cambered aerofoils from a given point over the surface other than the leading edge. The chordwise location of this point was assumed to be known from experiments. Clements and Maull (1975) and Saffman and Baker (1979) provided an excellent historical background on the computation of two-dimensional vortex sheets using vortex methods, whereas Leonard (1980) was concerned with the accuracy and computational efficiency and reviewed advancements up to that date.

2.2.2 Unsteady flow separation

Although the interest in using these vorticity-based methods for rapid flow estimations seemed to wane for some time, their use has received a new impetus in recent years, due to the ever-increasing availability of computational tools for speeding-up simulations, their intrinsic high modularity, and a wider access to resources. To provide an illustrative example of the computational cost reduction achieved in the last half century, to simulate the unsteady flow past a flat plate using ≈ 200 discrete vortices took Kuwahara (1973) ≈ 1 hour, in contrast with

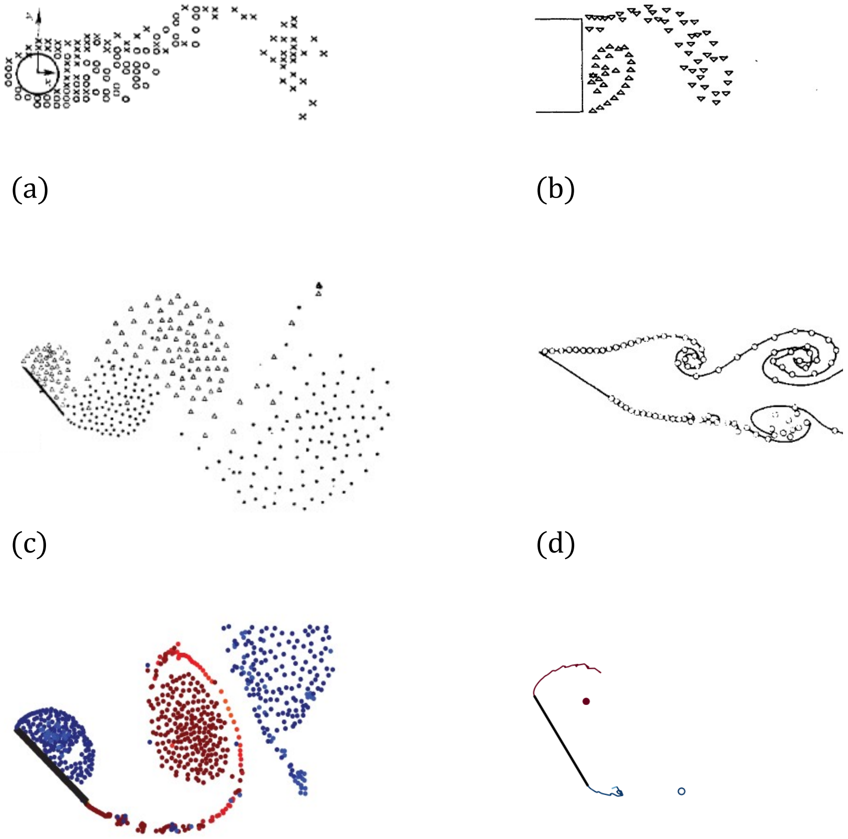

(a) (b)

(c) (d)

(e) (f)

Figure 2.2: Flow representation by different discrete-vortex methods, adapted with permission from: (*a*) Chorin (1973), (*b*) Clements (1973), (*c*) Sarpkaya (1975), (*d*) Katz (1981), (*e*) Ramesh et al. (2014) and (*f*) Darakananda and Eldredge (2019).

the ≈ 6 seconds needed in the present dissertation to recreate the unsteady flow due to a deforming foil using triple the number of vortex elements. Some initial challenges inherent in these methods have also been successfully addressed: the numerical complexity of velocity calculations through the Biot-Savart law (mutual interactions between a huge number of particles) has been reduced by employing adaptive fast summation algorithms (Greengard & Rokhlin, 1987); viscosity effects, such as diffusion of vorticity, are also being included in Lagrangian formulations with random-walk methods (Chorin, 1973). Figure 2.2 provides an illustrative example of the evolution of vortex methods over time: from bluff bodies (a, b), through steady foils (c, d), to unsteady foils (e, f).

The use of vortex models within the field of unsteady aerodynamics is seeing a boost in the last decade, primarily driven by the growing interest in bio-inspired flight and the advent of micro aerial vehicles. Built upon inviscid theories (Munk, 1923; Theodorsen, 1935; Von Karman & Sears, 1938; Wagner, 1925), vortex models might be augmented to include non-linearities arising from viscosity, dominant in these flight regimes, and be successful in modelling unsteady flow problems. Sears (1956) reviewed early investigations on the extension of classical potential flow theories to include viscous phenomena, such as flow separation and stall. Some of the earliest models developed for these scenarios are those by Ansari et al. (2006), Hammer et al. (2014), C. Wang and Eldredge (2013), and Xia and Mohseni (2013).

A critical aspect for the success of vortex models is how to determine the vorticity released into the flow field through the free vortex sheets formed at both edges of the aerofoil. Extensions to the classical steady Kutta condition have been developed to achieve this at the trailing edge. Among the efforts in this direction those by dos Santos et al. (2021), Ramesh (2022), Taha and Rezaei (2019), and Xia and Mohseni (2017) stand out. As for the leading edge, there is an ongoing quest for a universally valid criterion to predict the onset of unsteady flow separation. The documented evidence that the initiation of local reverse flow at the leading edge is correlated with critical flow events in this region (Beddoes, 1978; Ekaterinaris & Platzer, 1998; Evans & Mort, 1959; Shih et al., 1995), has led researchers to look at different leading-edge flow quantities, and several onset criteria are being suggested. On these lines, Narsipur et al. (2020) and Ramesh et al. (2014) examined the leading-edge suction, whereas Ramanathan et al. (2019) studied boundary-layer characteristics, and Kamrani-Fard et al. (2021) considered the wall shear stress.

Among the diverse criteria proposed to determine the onset of dynamic stall, the one by Ramesh et al. (2014) has been widely adopted in the development of low-order models for unsteady flows (Bird et al., 2021; Darakananda & Eldredge, 2019; Faure et al., 2022; Faure et al., 2020; Hirato et al., 2021; Z. Liu et al., 2017; Ramesh et al., 2015; Suresh-Babu et al., 2021). This criterion was defined based on the idea that for a given Reynolds number a rounded leading edge can sustain a limited amount of suction over which flow separates. During the process of vortex shedding that follows the amount of suction at the leading edge is maintained at that maximum value. This concept was used by Ramesh et al. (2018) and Suresh-Babu et al. (2022) to design combinations of pitch and plunge kinematics whose objective was to modulate the formation and shedding of LEVs.

Contrary to the previous assumption, a decay of suction force during the vortex formation process has been observed in recent investigations (Deparday & Mulleners, 2019; He et al., 2020; Narsipur, 2022; Narsipur et al., 2020). If this behaviour were correctly captured the post-separation performance of low-order models augmented with this criterion could be enhanced. But how to reproduce the observed evolution of leading-edge suction is an unanswered question.

In closing this section a last remark must be made: an important asset to evaluate the feasibility of numerical models towards real-time simulations and control is their ability to capture disturbances in the flow field caused by external inputs, as it can be due to the motion or deformation of the immersed body. Vortex methods are advantageous for the study of deforming bodies, or those with multiple elements undergoing independent motions from one another, as is the case of unsteady aerofoils equipped with a trailing-edge flap, the core of this research. Eulerian methods require the use of mesh deformation techniques, like remeshing at every time step of the simulation to adapt the grid to the shape-varying geometry. As far as the numerical computations are concerned, the added cost this operation entails makes Lagrangian methods, like vortex methods, a potential alternative tool for the analysis of flows over surfaces with time-varying shape, showing an excellent balance between reliability and computational time.

2.3 Flow control: Camber morphing

Biomimicry exerts an enormous influence on the design of flow control strategies. The natural ability of biological species to shape their propulsive surfaces, either passively or actively, to safely and efficiently deal with sudden changes in the flow, has inspired numerous investigations. A vast catalogue of bio-inspired control techniques can be found in the literature as a result. Extensive reviews are given by Harvey et al. (2022) and D. Li et al. (2018).

2.3.1 Passive control

Passive deflection of natural aeroelastic devices can improve the behaviour against stalling in feathered flyers. Under certain flight conditions, at high angles of attack, the alula deploys as a response to adverse pressure gradients at the leading edge (Alvarez et al., 2001). A streamwise vortex forms on the tip of this natural structure, and induces strong downwash delaying flow separation farther downstream (S. Lee et al., 2015). In situations when flow separates at the trailing edge, wing feathers rise off the surface in the reversed flow region to beneficially modify the unsteady vorticity field. This action prevents the upwards spread of the recirculating zone, delaying global separation on the suction side, thus increasing the operating angle of attack (Bechert et al., 2000; Carruthers et al., 2007). Emulating these natural reactions, self-deploying structures are becoming popular as a passive mechanism to enhance post-stall behaviour by altering the unsteady flow field they interact with (Brücker & Weidner, 2014; Johnston & Gopalarathnam, 2012; Nair et al., 2022; Rosti et al., 2018).

2.3.2 Active control

Active wing morphing may also lead to major changes in the aerodynamics. In terms of spanwise variations, birds and bats dynamically change their wingspan in flapping flight. By stretching and retracting their wings vortex structures can be intensified (S. Wang et al., 2014, 2015). But perhaps active chordwise morphing has been the bio-inspired flow control strategy most exploited. Figure 2.3 provides an illustrative example of camber morphing in nature.

Fixed-wing aircraft

In steady aerodynamic applications, like aircraft executing low-speed operations, temporary adjustments of the effective camber through deflection of control surfaces

Figure 2.3: Cambered wings of natural flyers: a moth (left) and a barn owl (right). Reproduced from Dalton (1999) with permission.

are known to improve aerodynamic performance during the different flight segments (take-off, cruise and landing).

Movable surfaces have also been applied on highly-manoeuvrable aircraft for transient lift control. For example, Rennie and Jumper (1996) investigated the application of a Dynamic Trailing-Edge Flap (DTEF) to cancel lift associated with the aerofoil's pitching motion; and Rennie and Jumper (1999) to cancel the lift perturbation caused by a gust (gust alleviation).

Rotor blades

Focused on unsteady separation control, the use of these moving surfaces has been widespread within the field of rotary wings, where dynamic stall is a major concern. Aiming to alleviate the undesirable effects of this phenomenon, the DTEF has been extensively used to improve rotor performance. Among the possible ways of altering the camber, acting on the trailing edge of the aerofoil is presumed to be a more appropriate choice for rotor blades, which normally encounter a severe environment at the leading edge. In this field, Feszty et al. (2004) numerically performed a systematic study of actuation parameters for a pulsed DTEF, to suggest optimum strategies which offered a compromise between minimising negative damping and maximising dynamic lift. They attributed the large negative pitching moment and associated negative damping primarily to the TEV, rather than the DSV already detached at this stage. The argument was that a force acting on a long arm to the pivot axis contributes significantly to the pitching moment. An upwards flap deflection displaces the TEV to a higher position, reducing the vertical distance with the DSV, which pushes the TEV off the trailing edge as it convects downstream. Suction due to the TEV thus diminishes, along with the associated negative pitching moment and damping. In an experimental extension of this work, Green et al. (2011) suggested that the favourable effect of a DTEF on dynamic loads was owed to the strong suction generated on its pressure side as a result of shape modification. Similar findings were reported by Gerontakos and Lee (2006) through experimental investigations using surface pressure measurements, upheld in follow-up works adding particle image velocimetry (Gerontakos & Lee, 2008), and harmonic DTEF (T. Lee & Su, 2011). More recently He et al. (2020) turned efforts towards characterising the influence of an oscillating DTEF on the development of dynamic stall, with a special focus on the evolution of the leading-edge suction parameter. Built on prior studies, Samara and Johnson (2020) analysed dynamic stall behaviour on a cambered aerofoil designed for small-scale wind turbines. Investigations on the use of DTEF with application to rotary wings were primarily conducted on oscillating aerofoils about the static-stall angle, intending to simulate the typical angle of attack variations experienced by rotor blades during low-speed forward flight. A mutual goal was the search for optimum combinations of DTEF actuation parameters that provide a good compromise between different aerodynamic requirements.

Micro aerial vehicles

In the last decade, unsteady flow separation at the leading edge has become a research area of general interest within the field of bio-inspired fluid mechanics, largely driven by the advent of MAVs. These new small-size flying devices are often equipped with thinner wings, perform more aggressive motions at higher dimensionless rates, and operate at lower Reynolds numbers than have previously been studied.

Some efforts have been addressed to better understand the effect of camber variation on the unsteady aerodynamics of bio-inspired locomotion. Along these lines, C. Li et al. (2015) performed a parametric study on a hovering plate with a harmonic DTEF superimposed. Including the hinge location, deflection amplitude and phase angle in the analysis, different camber patterns are formed, and a careful

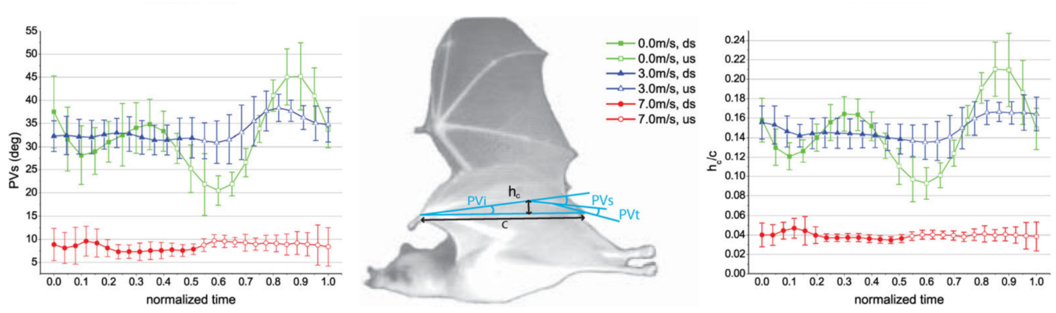

(a) (b)

Figure 2.4: Camber values found on bat wings: (*a*) angle deflected by the trailing edge, and (*b*) camber ratio. Adapted from Von Busse et al. (2012) with permission.

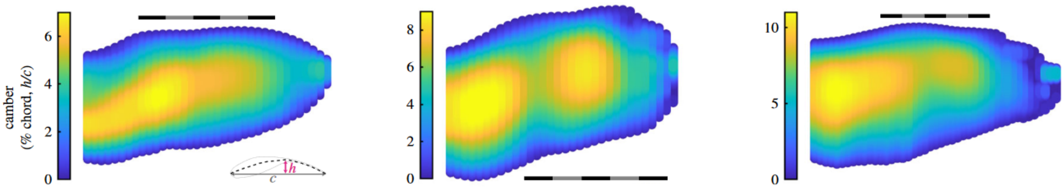

(a) (b) (c)

Figure 2.5: Camber values found on raptor wings, quantified as a percentage of the total chord length: (*a*) barn owl, (*b*) tawny owl and (*c*) goshawk. Adapted from Cheney et al. (2021) with permission.

selection of control parameters was shown to affect the strength of LEVs. The downside of this approach is that a larger parameter space would make finding the optimal impracticable. This led Xu et al. (2015) to develop an adjoint-based approach, with which the same optimal DTEF deflection angle and phase delay as C. Li et al. (2015) were reached at a much lower computational cost. In a similar manner in which previous studies generated different camber patterns by variations of the phase angle on oscillatory motions, Y. Liu et al. (2015) prescribed linear DTEF deflections in a translating wing with different times of actuation, showing that shedding behaviour could be altered by proper tailoring of the flap kinematics. Results obtained from these investigations are clear signs that trailing-edge flexion is directly connected with leading-edge vorticity alteration, and thus with the strength of LEVs. However, a quantitative relation is missing.

Furthermore, the high degree of morphing observed in the performance of many natural species (see Figs. 2.4 and 2.5), and its associated flow control benefits, has fired the interest on this practice, which has been reflected in a higher range of DTEF deflections sought. The degree of deformation of an aerofoil cross section can be quantified through a parameter that relates the maximum camber of the foil, η_{max}, to the total chord length, c (or distance from leading to trailing edge). This parameter is the camber ratio, $\frac{\eta_{max}}{c}$. In animal flight literature, some authors take the maximum camber of the profile to define such ratio (Maeda et al., 2017), whereas others use instead the camber at the mid chord (Walker et al., 2009), or even the average camber of the profile (Cheney et al., 2021). The chordwise coordinate of maximum camber (flexion point for a DTEF) is often located at or close to the mid chord of the aerofoil (Cheney et al., 2022; Cheney et al., 2021; Maeda et al., 2017; Muijres et al., 2008; Von Busse et al., 2012; M. Wolf et al., 2010; T. Wolf & Konrath, 2015), encouraging the use of larger DTEFs.

Attempts are being made to gain further insight into the use of larger DTEFs at high deflection rates. Medina et al. (2017) investigated the response of fast DTEF in separated flows as a possible route towards gust mitigation and to enable aggressive manoeuvres. Mancini et al. (2019) looked into the relationship between force and circulation production on a wing with a rapid DTEF. The transient effects of fast low-amplitude flap deflections on a massively separated flow over an aerofoil were studied by Medina et al. (2020). Medina and Hemati (2021) applied periodic flap deflections to suppress disturbances induced by a plunge motion, including the formation of LEVs.

The use of large camber variations towards unsteady flow control at low Reynolds numbers is proving to be a promising field of research, with still many challenges to face ahead. A summary of all these studies involving DTEFs is provided in Table 2.1, along with the actuation parameters used in each piece of research.

Table 2.1: Summary of studies on unsteady aerofoils with dynamic trailing-edge flap, detailing actuation parameters. Dashed lines separate between: highly manoeuvrable fixed-wing aircraft, rotary-wings, small-scale aerial vehicles.

Ref.	Aerofoil	Main motion	Flap motion	c_f/c [a]	δ_{max} [b]	Re
Rennie and Jumper (1996)	NACA 0009	ramp	ramp-hold	0.27	10°	$2 \cdot 10^5$
Rennie and Jumper (1999)	NACA 0009	ramp	calculated	0.27	calculated	$2 \cdot 10^5$
Feszty et al. (2004)	NACA 0012	oscillatory	pulse	0.16	±20°	$1.46 \cdot 10^6$
Gerontakos and Lee (2006)	NACA 0015	oscillatory	ramp-return	0.25	±15°	$1.65 \cdot 10^5$
Gerontakos and Lee (2008)	NACA 0015	oscillatory	ramp-return	0.25	±12°	$8.7 \cdot 10^4$
T. Lee and Su (2011)	NACA 0015	oscillatory	oscillatory	0.25	15°	$2.51 \cdot 10^5$
Green et al. (2011)	confidential	oscillatory	pulse	0.15	−20°	10^6
Samara and Johnson (2020)	S833	oscillatory	oscillatory	0.2	20°	$1.7 \cdot 10^5$
He et al. (2020)	NACA 0015	oscillatory	oscillatory	0.3	20°	$5.5 \cdot 10^5$
C. Li et al. (2015)	flat plate	hover	oscillatory	0.25	15° to 90°	10^2
Xu et al. (2015)	flat plate	hover	optimal	0.25	calculated	10^2
Su et al. (2017)	flat plate	hover	oscillatory	0.25	15° to 60°	10^2
Y. Liu et al. (2015)	~ NACA 0004	translation	ramp-hold	0.5	40°	$2.5 \cdot 10^2$
Medina et al. (2017)	NACA 0006	-	ramp-hold	0.5	±20°	$4 \cdot 10^4$
Mancini et al. (2019)	NACA 0006	-	ramp-hold	0.5	±40°	$4 \cdot 10^4$
Medina and Hemati (2021)	NACA 0006	plunge	oscillatory	0.5	20°	$4 \cdot 10^4$

---

[a] Flexion ratio

[b] Deflection amplitude

2.4 Research objectives - Original contributions

Itemised below are some gaps identified in the knowledge that are targeted in this dissertation. Each of them is followed by a description of the approach whereby posed questions have been tackled, and a summary of the remaining contents forming the chapter in which these novel findings are located within the main text.

1) Research on morphing strategies inspired by biological shape-adaptations has shown its potential for the control of unsteady flows. The majority of these works are experimental in nature or based on high-fidelity numerical computations, thus being constrained, either physically by the experimental setup, or in terms of time required. Given the fast-changing nature of unsteady flows, if the aim is to explore the control capability of strategies beyond the flow scenario for which they were first conceived, tools are desired to provide quick reliable results in diverse scenarios. The goal is then to introduce the effect of chordwise morphing in a simple mathematical model, leading to the following questions:

> – *To what precision can the behaviour of unsteady flows, including vortex dynamics and loads acting on the surface, be predicted by these means?*
>
> – *What degree of camber morphing can be attained?*

• Chapter 3 takes a step forwards in this direction with the development of a low computational-cost tool to simulate the response of unsteady flows to aerofoils undergoing large-amplitude variations of the camber. While keeping fairly high levels of accuracy, the run-times of this model are on the order of seconds. The first part of the chapter covers a thorough review of the mathematical background of the model. The second part validates its performance for a wide range of cases, combining several parameters involved in the definition of the camber.

• Chapter 4 complements the above efforts by providing an additional validation tool for the low-order model. Analytical expressions for the vortex sheet strength and Fourier coefficients are derived for the problem of a harmonic trailing-edge flap, which are later used as a reference against which to compare the low-order estimations.

2) By capturing the essential flow physics, vortex models can help in gaining fundamental comprehension of the dynamics of vortices. It is however apparent from the foregoing exposition around the latest approaches taken to model viscous phenomena, and the experimentally observed behaviour of the leading-edge suction during vortex formation, that a new method to determine the appropriate vorticity flux through separated shear layers has to be devised, which will make capturing post-separation flow behaviour possible, like the reattachment of shear layers. The questions then arise as to:

> – *Will a new formulation improve unsteady flow modelling?*
>
> – *How can post-stall evolution of flow characteristics be more accurately reproduced?*

• Chapter 5 bridges a gap in the current modelling of post-separation flow behaviour with vortex methods. To solve the existing issue on capturing the appropriate vorticity feeding rate through separated shear layers an alternative formulation is introduced. The strength of vortex particles entering the flow field at the leading edge is now expressed in terms of the velocity at the edge of the shear layer. After introducing this new approach, a thorough analysis is presented on the evolution of leading-edge suction and other flow variables during vortex formation, showing that the reattachment process of separated vortex sheets is now modelled correctly.

3) Considering the scarceness of studies where alteration of LEV development through camber variations has been characterised, there is scope for new contributions in this area. If the flow response to external inputs like surface deformations were successfully incorporated into vortex models (as indicated in the first point), it would allow us to better conceive of control strategies to modulate desired flow features. This leads one to pose the following questions:

> - *Which parameters govern the formation and growth of leading-edge vortices?*
>
> - *Is there hope to control LEV characteristics exploiting the fundamental knowledge procured with these simplified models?*

- Chapter 6 aims to deliver theoretical knowledge on the correlation between prescribed flexion at the trailing edge and alteration of flow properties at the leading edge, allowing for various parameters to be tested independently to quantify their effect on LEV formation and strength. The variable-camber discrete-vortex model is first validated under the presence of a strong leading-edge vortex, and is later used to trigger and delay its formation and to alter its strength, demonstrating the potential of camber morphing in modulating LEV characteristics. Additionally, an expression of the vortex strength is derived in terms of camber-defining parameters, which allows to gain insight into their effect on vortex formation.

It is not the strongest of the species that survives,
not the most intelligent that survives. It is the one
that is the most adaptable to change.

— Charles Darwin

3

MORPHING: MODELLING

3.1 Introduction

MORPHING takes a key role in this research, and the first half of the dissertation is devoted to its study. Shape-tailoring of appendages, like wings or tails, has shown to be influential in the success of biological locomotion. Fundamental insight into the correlation between geometrical changes on surfaces and local characteristics of the fluid around can be gained through mathematical analysis. Simplified aerodynamic models of bodies immersed in unsteady flows which represent this morphing practice are scarce. The dearth of such modelling tools motivates the development of a low-order model to simulate flow response to bodies undergoing arbitrary camber variations in time, which is the first objective of this thesis.

A widely validated discrete-vortex model for rigid wings is leveraged and extended to variable-camber wings in this chapter. The resulting Morphing Discrete-Vortex Model (MDVM) lays the groundwork for vortex-dynamics characterisation in response to shape variations from a theoretical perspective, the last objective of the research and content of Chapter 6.

This chapter is laid out as follows: The fundamentals of the low-order model are covered in §3.2, including an extension of Unsteady Thin-Aerofoil Theory (UTAT) for deformable bodies in §3.2.1, aspects of the numerical scheme in §3.2.2, and the derivation of aerodynamic loads in §3.2.3. The process of building and setting-up the CFD model used for validation is detailed in §3.3. The performance of the low-order model is demonstrated in §3.4, which starts reasoning the practicality of cases chosen (guided by patterns observed in nature) in §3.4.1, followed by a detailed explanation of expected limitations in computing the drag force in §3.4.2, to finally analyse flow and force evolution due to dynamic trailing-edge flexion, with small amplitude in §3.4.3, medium amplitude in §3.4.4, and large amplitude in §3.4.5. A summary to the chapter is given in §3.5.

3.2 Variable-camber discrete-vortex model

The pillars on which the mathematical model used in this research stands, deep-rooted in the concept of vorticity, are set out in this section. Namely, the bound vortex sheet and separated vortex sheets (from both, trailing and leading edge).

Concerning the first part, an adapted potential-flow theory for unsteady aerofoils is further extended to include temporal camber variations. This will constitute the central subject of the chapter, and a detailed elaboration on the underlying mathematics is provided in §3.2.1.

In relation to the second one, a time-stepping scheme is implemented in the discrete-vortex method. In the interest of brevity, only those aspects considered of greater importance for the correct understanding of the model are discussed in §3.2.2, and the interested readers in broadening their knowledge are referred to Katz and Plotkin (2001), Ramesh (2022), and Ramesh et al. (2014), where a good review on the matter is given.

As for the model augmentation to account for viscous effects, such as unsteady flow separation at the leading edge, details on the criterion adopted to determine the onset of LEV formation, and the different approaches considered to calculate the vorticity shedding rate from the separation point, will be extensively covered in Chapter 5 and barely touched upon here. Albeit being an essential question for the ultimate goal of the low-order model, the focus of this first theoretical chapter is on morphing. To avoid the risk of falling into unnecessary repetition, and to make a clear distinction between the modelling targets pursuit on each chapter, separation at the leading edge has been omitted for now, and the cases analysed in §3.4 have been selected accordingly.

3.2.1 Bound vortex sheet

The high complexity of many fluid problems requires simplifying assumptions to be made for their study. Such is the case of a fluid domain enclosing an aerodynamic profile. If the fluid surrounding the body and its wake is considered to be inviscid and incompressible (effects of viscosity and compressibility neglected), the Navier-Stokes continuity equation, which states no fluid is being created or destroyed, takes the form of the Laplace's equation for the velocity potential, ϕ:

$$\nabla^2\phi = 0 \quad . \tag{3.1}$$

Solving this potential flow equation provides the velocity field due to the motion and deformation of the aerofoil.

A fluid parcel in the immediate vicinity of a moving/deforming wall is subjected to the local velocities of the flow and the body. Owing to viscosity, the tangential component of the velocity field across the interface may suffer from a discontinuity. This imparts a rotational motion to the fluid in the boundary layer, in other words, vorticity is created and confined in a thin layer adjacent to the wall. The solution to Eq. (3.1) reduces to finding an appropriate combination of elementary solutions distributed over the chord line, the position and strength of which is adjusted for the no-through-flow boundary condition to be satisfied on the aerodynamic surface being modelled, here the camber line. An arrangement of singularities consisting on vortex elements is traditionally chosen because of their physical character. The resulting line of variable vorticity is known as the bound vortex sheet, and it represents the vorticity created at the boundary layer.

For simplicity, these elements are continuously distributed. The use of continuous chordwise vorticity loading was introduced by Birnbaum (1924). Applying the method of Fourier series to his conception, Glauert (1927) approximated the distribution of bound vorticity, γ_B, by an equivalent trigonometric expansion, which for the general time-dependent problem takes the form:

$$\gamma_B(\theta, t) = 2U_{ref}\left[A_0(t)\frac{1+\cos\theta}{\sin\theta} + \sum_{n=1}^{\infty} A_n(t)\sin(n\theta)\right] \quad , \tag{3.2}$$

with U_{ref} being a reference velocity; $A_0(t)$, $A_1(t)$, ..., $A_n(t)$ time-dependent Fourier coefficients, whose expressions are determined as functions of the instantaneous local downwash (given in Eq. (3.25)); t the time; and θ the variable of transformation used in the discretisation of the chord line, which for mathematical convenience relates Cartesian to trigonometric coordinates according to the Glauert's transform $x = \frac{c}{2}(1 - \cos\theta)$, where c is the chord length. Values of θ vary from 0 at the leading edge to π at the trailing edge.

The first feature of note in Eq. (3.2) is that the steady Kutta condition is automatically satisfied, since zero vorticity at the trailing edge is implicitly enforced, $\gamma_B(\pi) = 0$. Another point to highlight is the singularity of the first term at the leading edge, $\gamma_B(0) \to \infty$, which allows to model the high suction peak in this region observed experimentally. This fact prompted the definition of an inviscid parameter connected to the A_0 Fourier term which serves to predict the onset of flow separation at the leading edge, and will be thoroughly discussed in Chapter 5.

Morphing-defining parameters

Information is needed about the shape of the solid surface on which the boundary condition is to be imposed. In the most general form, a wing can be represented by its upper and lower surfaces, which in a Cartesian coordinate system attached to the wing reads:

$$z(x, y) = \eta_c(x, y) \pm \eta_t(x, y) \quad , \tag{3.3}$$

where η_c symbolises the camber line and η_t the thickness. Positive and negative signs distinguish between suction and pressure surfaces respectively.

If a cross-section at an arbitrary spanwise location is considered (2D simplification) and the thickness effect neglected (thin aerofoil), the wing can be replaced by its camber line, $z = \eta(x)$, the locus of points midway between upper and lower surfaces. Some important aerodynamic characteristics of a wing section, like the chordwise load distribution, are fundamentally associated with that shape, which can vary in time due to deformation. To tackle this problem, the camber line can be broken down into two components, η_{geom} and η_{def}. The former denotes the geometrical camber, whereas the latter accounts for time-dependent chordwise deformations. A general deforming aerofoil can then be expressed according to:

$$\eta(x,t) = \eta_{geom}(x) + \eta_{def}(x,t) \quad . \tag{3.4}$$

The most basic representation of chordwise deformation is the flapped flat plate, this is, a rigid plate (the control surface, such as a trailing-edge flap) hinged at a specific point to another rigid plate (the foil's main element). For this initially uncambered case, symmetric in clean configuration, $\eta_{geom}(x) = 0$ and $\eta_{def}(x,t)$ is a piece-wise-linear function. This mechanism, despite its simplicity, serves to set the basis of morphing modelling with potential flow theory. And the extension to more complex deforming patterns is a promising future line of research, as suggested in Chapter 7.

A classical approach to the flap problem (Katz & Plotkin, 2001) considers a fixed chord line along which bound vorticity is distributed. The chordwise distribution of camber has non-zero value for only those points after the hinge position, and is given by:

$$\eta(x) = \begin{cases} 0 & \text{for} \quad x_{LE} < x < x_{hg} \quad , \\ -(x - x_{hg})\sin\delta & \text{for} \quad x_{hg} < x < x_{TE} \quad , \end{cases} \tag{3.5}$$

where x_{LE}, x_{hg} and x_{TE} are the chordwise coordinates of the leading edge, hinge, and trailing edge respectively; and δ is the flap deflection angle (positive downwards).

Following the assumption of small-disturbance flow in thin-aerofoil theory, the approximation can be made that the boundary condition is transferred from the camber line, $z = \eta(x)$, to the chord line, $z = 0$. This simplification can be demonstrated through a Taylor series expansion of the velocity potential:

$$\frac{\partial \phi}{\partial z}(x, z = \eta) = \frac{\partial \phi}{\partial z}(x, z = 0) + \eta \frac{\partial^2 \phi}{\partial z^2}(x, z = 0) + \mathcal{O}(\eta^2) \quad . \tag{3.6}$$

A first-order approximation to the exact mathematical formulation of the problem enables an easier treatment of the boundary condition. In order to retain only the linear term of the expansion, the camber must be sufficiently small compared to the chord for distances measured along both lines to be similar:

$$\frac{\eta(x)}{c} \ll 1 \qquad \forall x \quad . \tag{3.7}$$

As this ratio increases so does the error introduced in the solution, since higher-order terms are being neglected. If large-amplitude deflections are sought, the camber will be large at the trailing edge (see Eq. (3.5)), and condition (3.7) will be violated. Additionally, for the trailing edge to stay in the perpendicular to its initial position, the flap length needs to be extended as the deflection angle increases. To avoid losing physical sense (chord length must be fixed in the absence of elasticity), and to stay within the applicability bounds of thin-aerofoil theory, deflections are constrained for the traditional fixed chord line approach to rather small values.

A novel approach to the problem, introduced in this thesis, aims to overcome the previous geometrical restriction by proposing a time-varying chord line. This effective chord line, c_{eff}, is defined as the line which connects leading and trailing edges at all times (see Fig. 3.1). Using the law of cosines, which generalises the Pythagorean theorem for non-right triangles, a relation can be obtained between the lengths of the flap and foil's main element, and the angle they form. Observing this angle is $\pi - \delta$, the instantaneous effective chord length can be expressed as:

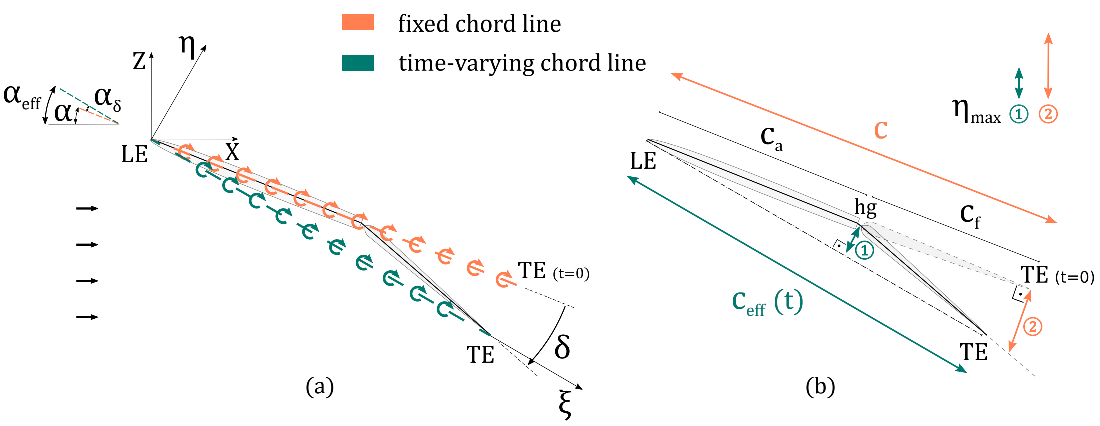

Figure 3.1: Schematic of different approaches to model a variable-camber aerofoil: fixed chord line vs. time-varying chord line. Information displayed includes: frames of reference, spatial distribution of bound vorticity (round arrows) and angles in (a); chord lengths and maximum camber in (b). All parameters are defined in the main text.

$$c_{eff}(t) = \sqrt{{c_a}^2 + {c_f}^2 + 2\, c_a\, c_f \cos\delta(t)} \quad , \tag{3.8}$$

where c_a and c_f represent the fore element and flap chord lengths respectively. The sum of both terms gives the foil total chord length, $c = c_a + c_f$.

In dealing with bodies subject to time-dependent motions and deformations, an appropriate frame of reference is essential. The body-fixed frame $LE\,\xi\,\eta$ is used in this work: pinned at the leading edge of the camber line, with one of its axes along the effective chord line and the other normal to it, as illustrated in Fig. 3.1(a). Any point of the foil is therefore described by its chordwise coordinate, ξ, and its normal coordinate, η, in this frame of reference.

The chordwise axis forms with the horizontal axis of an inertial frame an effective angle of attack, α_{eff}, composed by the pitch angle (positive upwards), α, and an additional contribution due to the flap deflection, α_δ, as shown in Fig. 3.1(a):

$$\alpha_{eff}(t) = \alpha(t) + \alpha_\delta(t) \quad . \tag{3.9}$$

The effect of this last component can be thought of as an increase in effective angle for downwards flap deflections (those leading to an increment of positive camber, or negative camber reduction), and a decrease in effective angle when it deflects upwards (reduction of positive camber, or negative camber increment). Similarly to how Eq. (3.8) has been derived, the law of sines enables to express the instantaneous value of this angle in terms of shape-control parameters:

$$\alpha_\delta(t) = \arcsin\left(\frac{c_f}{c_{eff}(t)}\sin\delta(t)\right) \quad . \tag{3.10}$$

The chordwise coordinate in the new frame of reference is given by the Glauert transform as:

$$\xi = \frac{c_{eff}}{2}(1-\cos\theta) \quad , \tag{3.11}$$

and the camber distribution is derived as a piece-wise function analogous to Eq. (3.5):

$$\eta(\xi) = \begin{cases} \xi\,\tan\alpha_\delta & \text{for} \quad \xi_{LE} < \xi < \xi_{hg} \quad , \\ (c_{eff}-\xi)\,\tan(\delta-\alpha_\delta) & \text{for} \quad \xi_{hg} < \xi < \xi_{TE} \quad , \end{cases} \tag{3.12}$$

with $\xi_{LE} = 0$, $\xi_{TE} = c_{eff}$ and $\xi_{hg} = c_a\,cos\alpha_\delta$ being the chordwise coordinates of the leading edge, trailing edge and hinge respectively. Variation of θ from 0 to π traces the camber line.

Camber is maximum at the hinge location, and its magnitude can be written as a fraction of the effective chord length as:

$$\frac{\eta_{max}}{c_{eff}} = \frac{c_a}{c_{eff}}\frac{c_f}{c_{eff}}\sin\delta \quad . \tag{3.13}$$

With this novel approach the maximum camber ratio is reduced compared to the classical approach, decreasing the departure from small-disturbance assumption, and improving the accuracy on estimation of aerodynamic loads. A comparison of the magnitude of maximum camber obtained in each approach for the same flap deflection is given in Fig. 3.1(*b*).

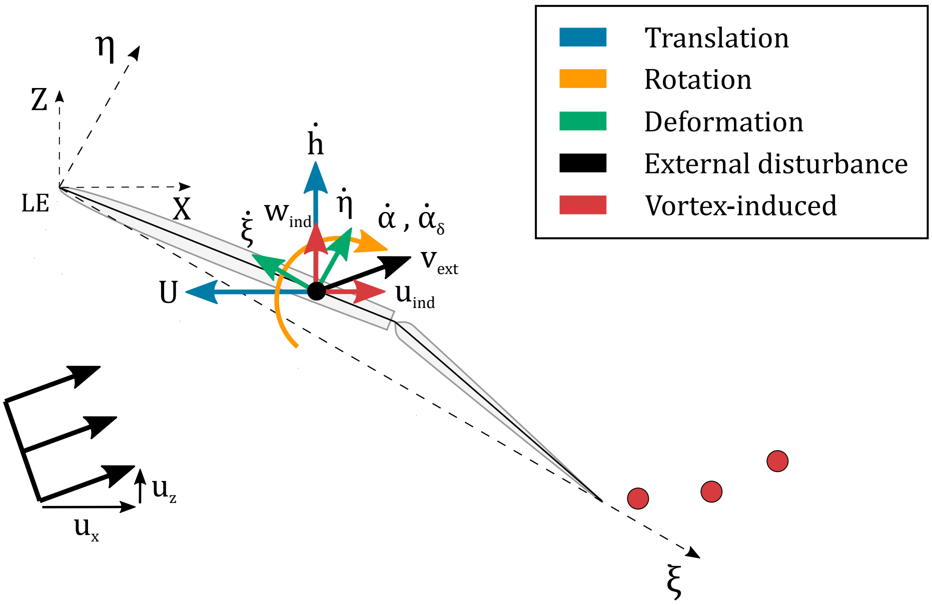

Figure 3.2: Velocity components of an arbitrary point over the foil camber line. The diverse sources of velocity are colour-coded in the box. The orientation of vectors drawn correspond to the following case: a foil moving leftwards, plunging upwards, pitching clockwise, with a flap being deflected clockwise, and a gust coming from the bottom left. Positive axes of each coordinate system are shown for reference.

Unsteady boundary condition

The differential form of the continuity equation as defined in Eq. (3.1) does not depend directly on time. In the treatment of unsteady flows, time dependency comes into play through the boundary condition. Typically, the Neumann form of the present boundary value problem imposes a no-slip boundary condition for a real fluid, which requires it to have zero relative velocity with respect to the solid surface in a frame of reference attached to the body. Since viscous effects of the boundary layer are neglected in potential flows, the tangential component of the local velocity is unrestricted, but zero-normal flow needs to be enforced at each point across the fluid-solid interface, $\mathbf{v} \cdot \mathbf{n} = 0$.

Fluid particles in that region flow tangentially to the camber line. Their velocity stems from a combination of external flow perturbations, velocities induced by vortices in the flow field, body motion and surface deformation, as depicted in Fig. 3.2. From action-reaction principle, the sign is the opposite for those contributions that are due to the interface moving/deforming:

$$\mathbf{v} = -\mathbf{v}_0 - \mathbf{v}_{rot} - \mathbf{v}_{rel} + \mathbf{v}_{ext} + \nabla\boldsymbol{\phi} \quad . \tag{3.14}$$

Coordinates of each velocity contribution expressed in the body-fixed frame are:

1. Velocity of the origin, due to translation

$$\mathbf{v}_0 = \left(-U\cos\alpha_{eff} - \dot{h}\sin\alpha_{eff} \,, 0 \,, -U\sin\alpha_{eff} + \dot{h}\cos\alpha_{eff}\right) \quad . \tag{3.15}$$

2. Velocity as a rigid body, due to rotation

$$\left.\begin{aligned} \mathbf{v}_{rot} = \;& \boldsymbol{\Omega}_1 \times \mathbf{r}_1 + \boldsymbol{\Omega}_2 \times \mathbf{r}_2 \\ & \boldsymbol{\Omega}_1 = (0\,, \dot{\alpha}\,, 0) \quad , \quad \boldsymbol{\Omega}_2 = (0\,, \dot{\alpha}_\delta\,, 0) \\ & \mathbf{r}_1 = (\xi - \xi_{pvt}\,, 0\,, \eta - \eta_{pvt}) \quad , \quad \mathbf{r}_2 = (\xi\,, 0\,, \eta) \end{aligned}\right\} \quad . \tag{3.16}$$

3. Relative velocity, due to deformation

$$\mathbf{v}_{rel} = \left(-\dot{\xi}\,, 0\,, \dot{\eta}\right) \quad . \tag{3.17}$$

4. External velocity, due to flow disturbances like gusts

$$\mathbf{v}_{ext} = (u_x\cos\alpha_{eff} - u_z\sin\alpha_{eff}\,, 0\,, u_x\sin\alpha_{eff} + u_z\cos\alpha_{eff}) \quad . \tag{3.18}$$

5. Vortex-induced velocity, due to TEVs and LEVs

$$\nabla\boldsymbol{\phi} = \left(\frac{\partial\phi_B}{\partial\xi} + \frac{\partial\phi_{TEV}}{\partial\xi} + \frac{\partial\phi_{LEV}}{\partial\xi}\,, 0\,, \frac{\partial\phi_B}{\partial\eta} + \frac{\partial\phi_{TEV}}{\partial\eta} + \frac{\partial\phi_{LEV}}{\partial\eta}\right) \quad . \tag{3.19}$$

A generic pitching and plunging foil moves with a constant horizontal velocity in the inertial frame (no surge motion prescribed), U, and a plunge velocity in the vertical direction, $\dot{h}$. The forward velocity is taken as the reference velocity for Eqs. (3.2) and (3.25), $U_{ref} = U$. The effective angle of attack, α_{eff}, is used to transform between the body-fixed and inertial frames (see Fig. 3.1). For the angular variation terms, $\dot{\alpha}$ is the pitch rate about the pivot axis, of coordinates $\xi_{pvt} = c_{pvt}\cos\alpha_\delta$ and $\eta_{pvt} = c_{pvt}\sin\alpha_\delta$ in the body-fixed frame, where c_{pvt} is the distance from the leading edge to the pivot point; and $\dot{\alpha}_\delta$ is the rotation rate of the coordinate system about the leading edge due to flap deflection. The relative velocity of points along the surface is due to temporal variations in the camber and effective chord length. The sign of its components can be explained as follows: a positive flap deflection growing in magnitude, $\delta > 0$ with $\dot{\delta} > 0$, causes an increase in camber, $\dot{\eta} > 0$, and a reduction in effective chord length, $\dot{\xi} < 0$. Without any loss of generality, it is assumed in this research there are no external flow disturbances, $u_x = u_z = 0$. Finally, it must be pointed out that the velocity potential, ϕ, is comprised of terms associated with bound vorticity, ϕ_B, trailing-edge vorticity, ϕ_{TEV}, and leading-edge vorticity, ϕ_{LEV}. Then, $\frac{\partial \phi}{\partial \xi}$ and $\frac{\partial \phi}{\partial \eta}$ are velocities induced tangential and normal to the effective chord line by all of these vortices. Although cases studied in this chapter do not cover leading-edge vorticity shedding, its contribution is kept in all expressions since these generic forms will be used in later chapters without modifications.

Expressed in the body frame of reference, the chordwise and normal velocity components at an arbitrary point over the camber line are:

$$v_\xi = \frac{\partial \phi}{\partial \xi} + U \cos \alpha_{eff} + \dot{h} \sin \alpha_{eff} - \dot{\alpha}(\eta - \eta_{pvt}) - \dot{\alpha}_\delta \eta + \dot{\xi} \quad , \tag{3.20a}$$

$$v_\eta = \frac{\partial \phi}{\partial \eta} + U \sin \alpha_{eff} - \dot{h} \cos \alpha_{eff} + \dot{\alpha}(\xi - \xi_{pvt}) + \dot{\alpha}_\delta \xi - \dot{\eta} \quad . \tag{3.20b}$$

Surfaces, here reduced to the camber line, can be defined by an implicit function, which in the frame of reference attached to the body is $F(\xi, \eta, t) \equiv \eta - \eta(\xi, t) = 0$. The unit normal vector to this surface (positive outwards) is proportional to the gradient of that function:

$$\mathbf{n} = \frac{\nabla \mathbf{F}}{|\nabla \mathbf{F}|} = \frac{1}{\sqrt{1 + \left(\frac{\partial \eta}{\partial \xi}\right)^2}} \left(-\frac{\partial \eta}{\partial \xi}, 0, 1\right) \quad . \tag{3.21}$$

Adding all the foregoing velocity contributions in Eqs. (3.15) to (3.19) to define the velocity vector of a fluid particle at an arbitrary point over the camber line, applying the boundary condition with the normal vector obtained from the implicit representation of the camber line in Eq. (3.21), and rearranging the solution, yields the instantaneous local downwash or induced velocity normal to the surface, $\frac{\partial \phi_B}{\partial \eta}$. For an arbitrary flapping and simultaneously deforming foil in a generic vortex-dominated scenario (TEVs and LEVs shed) the expression has the general form:

$$\boxed{\begin{aligned} &W(\xi,t) = \\ &\frac{\partial \eta}{\partial \xi}\left(\frac{\partial \phi_{TEV}}{\partial \xi} + \frac{\partial \phi_{LEV}}{\partial \xi} + U\cos\alpha_{eff} + \dot{h}\sin\alpha_{eff} - \dot{\alpha}(\eta - \eta_{pvt}) - \dot{\alpha}_\delta \eta + \dot{\xi}\right) \\ &- \frac{\partial \phi_{TEV}}{\partial \eta} - \frac{\partial \phi_{LEV}}{\partial \eta} - U\sin\alpha_{eff} + \dot{h}\cos\alpha_{eff} - \dot{\alpha}(\xi - \xi_{pvt}) - \dot{\alpha}_\delta \xi + \dot{\eta} \quad . \end{aligned}} \tag{3.22}$$

This general expression of the downwash includes the effects of motion kinematics, camber line deformations and flow induced by vortices. The term $\frac{\partial \phi_B}{\partial \xi}$ has been neglected since it is an order of magnitude smaller than the other terms. Temporal derivatives, $\dot{\alpha}_\delta$, $\dot{\xi}$, and $\dot{\eta}$, are obtained by differentiating Eqs. (3.8) to (3.13):

$$\dot{\alpha}_\delta = \frac{\cos\delta + \frac{c_a}{c_{eff}}\frac{c_f}{c_{eff}}\sin^2\delta}{\frac{c_a}{c_f} + \cos\delta}\dot{\delta} \quad , \tag{3.23a}$$

$$\dot{\xi} = \xi\frac{\dot{c}_{eff}}{c_{eff}} = -\xi\frac{\eta_{max}}{c_{eff}}\dot{\delta} \quad , \tag{3.23b}$$

$$\dot{\eta} = \begin{cases} \tan\alpha_\delta \dot{\xi} + \frac{\xi}{\cos^2\alpha_\delta}\dot{\alpha}_\delta \quad \text{for} \quad \xi < \xi_{hg} \quad , \\ \left(\frac{\xi}{c_{eff}} - 1\right)\eta_{max}\tan(\delta - \alpha_\delta)\dot{\delta} + \frac{c_{eff}-\xi}{\cos^2(\delta-\alpha_\delta)}(\dot{\delta} - \dot{\alpha}_\delta) \quad \text{for} \quad \xi > \xi_{hg} \quad , \end{cases} \tag{3.23c}$$

where $\dot{\delta}$ is the rate of flap deflection.

Velocities induced by vortices in the flow field are converted to the body-fixed frame using the effective angle of attack:

$$\frac{\partial \phi_{TEV,LEV}}{\partial \xi} = u_{ind}\cos\alpha_{eff} - w_{ind}\sin\alpha_{eff} \quad , \tag{3.24a}$$

$$\frac{\partial \phi_{TEV,LEV}}{\partial \eta} = u_{ind}\sin\alpha_{eff} + w_{ind}\cos\alpha_{eff} \quad , \tag{3.24b}$$

with u_{ind} and w_{ind} being the vortex-induced velocities (for both TEV and LEV) in the inertial x and z directions, respectively, obtained in Eq. (3.27).

The Fourier coefficients introduced in Eq. (3.2) are related to the shape of the foil through the boundary condition enforced on its camber line. They are given in terms of the instantaneous local downwash in the body-fixed frame as:

$$A_0(t) = -\frac{1}{\pi}\int_0^{\pi} \frac{W(\xi,t)}{U_{ref}} d\theta \quad , \tag{3.25a}$$

$$A_n(t) = \frac{2}{\pi}\int_0^{\pi} \frac{W(\xi,t)}{U_{ref}} \cos(n\theta) d\theta \quad . \tag{3.25b}$$

Lastly, the bound circulation can be computed by integrating the distribution of bound vorticity in Eq. (3.2) over the time-varying chord line:

$$\Gamma_B(t) = \pi c_{eff} U_{ref} \left(A_0(t) + \frac{A_1(t)}{2} \right) \quad . \tag{3.26}$$

3.2.2 Separated vortex sheets

Creation of vorticity is conceivable without contradicting Helmholtz-Kelvin theorems by changing topological flow properties: vorticity created as a free sheet (Saffman, 1995). Hence, a trailing-edge vortex sheet forms as an aerofoil moves following a prescribed trajectory. Leading-edge vortex sheets can also arise in certain scenarios, but their study is left for Chapter 5.

Within the framework of vortex methods, each of these sheets is approximated by an array of vorticity-carrying elements as depicted in Fig. 3.3 (the complete picture of an unsteady foil with free vortex sheets at both edges is given in Fig. 5.1). The amount of particles representing these sheets is determined in the current model using a time-stepping scheme, as described in Katz and Plotkin (2001) and highlighted in Ramesh et al. (2013). At each time step of the numerical simulation a discrete vortex is shed from the trailing edge (for the leading edge see §5.2).

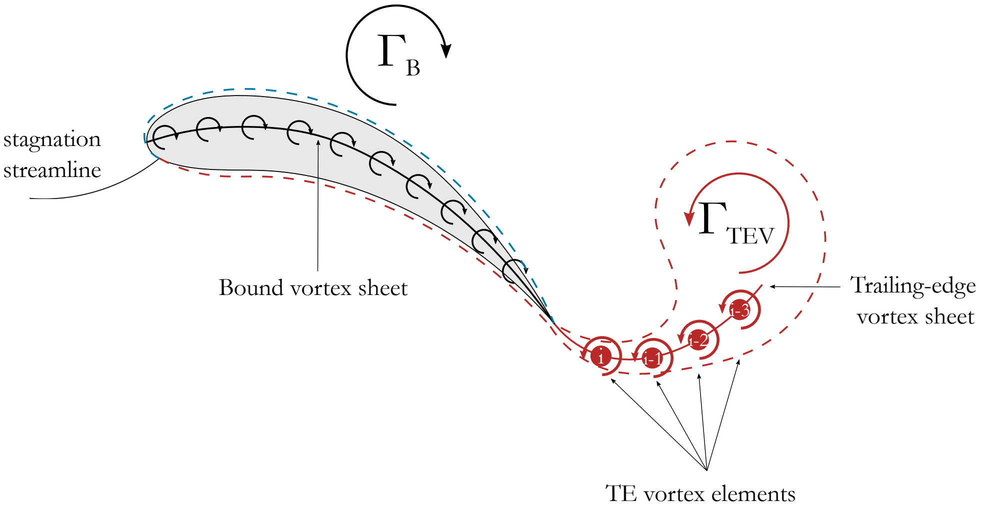

Figure 3.3: Representation of a separated shear layer at the trailing edge of an unsteady foil by vortex elements.

Point vortices were used to represent flows in the earliest discrete-vortex methods (Rosenhead, 1931). Vortices in close proximity could induce artificially large velocities on each other. To eliminate numerical stiffness, the idea of treating vortices as distributed vortex cores, or vortex blobs with finite core radii, was introduced by Chorin (1973). Induced velocities in the flow field are then bounded by including the core radius of the blob, v_{core}, in their calculation. The vortex-core model proposed by Vatistas et al. (1991), based on an empirical formula for the tangential velocity component, is used in this work.

Therefore, knowing the strength of the k-th wake vortex shed at time step $i-1$ (from the trailing edge in this case), Γ_k, the induced downwash components on any point of the aerofoil (x,z), due to this vortex located at (x_k,z_k) in the current time step i, are provided by the Biot-Savart law:

$$u_{ind} = \frac{\Gamma_k}{2\pi} \frac{z - z_k}{\sqrt{\left((x - x_k)^2 + (z - z_k)^2\right)^2 + v_{core}^4}} \quad , \tag{3.27a}$$

$$w_{ind} = -\frac{\Gamma_k}{2\pi} \frac{x - x_k}{\sqrt{\left((x - x_k)^2 + (z - z_k)^2\right)^2 + v_{core}^4}} \quad . \tag{3.27b}$$

Two alternative ways to compute the strength assigned to trailing-edge vortex elements are discussed in what follows.

Many discrete-vortex methods use an iterative process so the Kelvin circulation conservation theorem is fulfilled. This theorem establishes the relationship between the free vortex sheets formed at both edges of the foil and the bound vortex sheet:

$$\frac{d\Gamma_B(t)}{dt} + \frac{d\Gamma_{LEV}(t)}{dt} + \frac{d\Gamma_{TEV}(t)}{dt} = 0 \quad . \tag{3.28}$$

The bound circulation, Γ_B, is taken from Eq. (3.26), and no shedding of leading-edge vorticity is considered in this chapter, $\Gamma_{LEV} = 0$. The strength of trailing-edge vortex elements is then easy to compute.

According to literature on the Kutta condition, velocity being finite at the trailing edge, which is the steady Kutta condition, is necessary but insufficient to correctly determine the circulation for unsteady flows. An additional condition is needed in scenarios where vorticity is continuously shed from the trailing edge. This might be expressed as continuity in the vortex sheet across the trailing edge (non-zero vorticity). If a point vortex or regularised vortex blob is used to represent shed wake vorticity at any discrete time step there is a discontinuity across the trailing edge, and the second condition is not satisfied. The solution is then erroneous. As an alternative, Ramesh (2022) proposed a continuous distribution of vorticity, derived from the exact Wagner solution, to represent the last shed vorticity at any time. This distribution is later converted into a vortex blob placed at its centroid, and the calculation advances as for the other approach. Details on the implementation are provided in that paper. Results from MDVM using both approaches are compared later in §3.4.3.

For convergence of vortex-blob methods, it is necessary that the vortex-core radius be larger than the average spacing between blobs, d, which means they must overlap (Hald, 1979). In this work the radius is taken to be $v_{core} = 1.3d$ following guidelines from Leonard (1980).

Testing different non-dimensional time steps, $\Delta t^* = \frac{\Delta t U}{c}$, proved that 0.015 yielded good results in most simulations (balancing precision-speed), and this value has been used in all results shown in this dissertation. Since a vortex blob is released at every time step of the simulation, Δt, the distance between consecutive blobs is $d = \Delta t U$, or in terms of the non-dimensional time step $d = \Delta t^* c$. Hence the vortex core radius used in this work is $v_{core} = 0.02c$.

The last shed particle in vortex methods is traditionally positioned along the path line of the shedding edge. If it is placed instead at one third of the distance from the edge to the previously shed particle (Ansari et al., 2006), the flow is more accurately described as both effects are taken into account, the motion of the aerofoil and the advection of the previous particle. As for the first shed particle, its position is determined with the velocity at the shedding edge.

To advance the calculation, particles in the flow field are convected with the net velocity induced in their centre (free stream velocity plus mutual interactions), enabling the rolling-up into vortex structures, thus featuring a deforming wake. Particles of the bound vortex sheet move with the aerofoil velocity.

3.2.3 Pressure distribution and aerodynamic coefficients

Once the velocity field is known, the pressure distribution over the aerofoil surfaces is derived by means of Bernoulli's equation modified for the unsteady regime:

$$\Delta p(\xi) = p_l(\xi) - p_u(\xi) = \rho \left[\frac{1}{2}(V_{t_u}^2 - V_{t_l}^2) + \left(\left.\frac{\partial \phi}{\partial t}\right|_u - \left.\frac{\partial \phi}{\partial t}\right|_l \right) \right] \quad . \tag{3.29}$$

The tangential velocity in the first term can be obtained from Eq. (3.20) for points ahead and behind the hinge as:

$$V_t = \begin{cases} v_\xi \cos\alpha_\delta + v_\eta \sin\alpha_\delta & \text{for} \quad \xi < \xi_{hg} \quad , \\ v_\xi \cos(\delta - \alpha_\delta) - v_\eta \sin(\delta - \alpha_\delta) & \text{for} \quad \xi > \xi_{hg} \quad . \end{cases} \tag{3.30}$$

This expression simplifies to $V_t = v_\xi$ after transferring the boundary condition from the camber line to the chord line.

On evaluation of Eq. (3.20a) over the upper and lower sides of the chord line, the only term that differs is the spatial derivative with respect to the chordwise coordinate of the velocity potential due to bound vorticity, $\frac{\partial \phi_B}{\partial \xi}$. Its value above and below a vortex distribution is given by:

$$\left.\frac{\partial \phi_B}{\partial \xi}\right|_u = \frac{\gamma(\xi)}{2} \quad , \quad \left.\frac{\partial \phi_B}{\partial \xi}\right|_l = -\frac{\gamma(\xi)}{2} \quad . \tag{3.31}$$

Bearing in mind that squared terms have the same value on the upper and lower side they cancel out in the pressure difference, and the only contribution is due to double products of summands if $\frac{\partial \phi_B}{\partial \xi}$ is present. Hence, the first term in Eq. (3.29), using the values from Eq. (3.31), becomes:

$$\begin{aligned} \frac{1}{2}(V_{t_u}^2 - V_{t_l}^2) = \Big(& \frac{\partial \phi_{TEV}}{\partial \xi} + \frac{\partial \phi_{LEV}}{\partial \xi} + U \cos \alpha_{eff} + \dot{h} \sin \alpha_{eff} \\ & - \dot{\alpha}(\eta - \eta_{pvt}) - \dot{\alpha}_\delta \eta + \dot{\xi} \Big) \gamma(\xi) \quad . \end{aligned} \tag{3.32}$$

Evaluating in a similar way the second term in Eq. (3.29), only the velocity potential associated to the bound vorticity, ϕ_B, differs for the upper and lower sides. Thus, integrating Eq. (3.31) and deriving in time yields the pressure jump contribution:

$$\left.\frac{\partial \phi}{\partial t}\right|_u - \left.\frac{\partial \phi}{\partial t}\right|_l = \frac{\partial}{\partial t} \int_0^\xi \gamma(\xi) d\xi \quad . \tag{3.33}$$

A final expression for the pressure difference on the aerofoil is attained by substituting Eqs. (3.32) and (3.33) in Eq. (3.29):

$$\begin{aligned} \Delta p(\xi) = \rho \Big[\Big(& \frac{\partial \phi_{TEV}}{\partial \xi} + \frac{\partial \phi_{LEV}}{\partial \xi} + U \cos \alpha_{eff} + \dot{h} \sin \alpha_{eff} \\ & - \dot{\alpha}(\eta - \eta_{pvt}) - \dot{\alpha}_\delta \eta + \dot{\xi} \Big) \gamma(\xi) + \frac{\partial}{\partial t} \int_0^\xi \gamma(\xi) d\xi \Big] \quad . \end{aligned} \tag{3.34}$$

The normal force acting on the aerofoil is obtained by integrating the pressure jump from Eq. (3.34) over the chord line:

$$\begin{aligned} F_N = \rho \Big[\int_0^{c_{eff}} \Big(& \frac{\partial \phi_{TEV}}{\partial \xi} + \frac{\partial \phi_{LEV}}{\partial \xi} + U \cos \alpha_{eff} + \dot{h} \sin \alpha_{eff} \\ & - \dot{\alpha}(\eta - \eta_{pvt}) - \dot{\alpha}_\delta \eta + \dot{\xi} \Big) \gamma(\xi) d\xi + \int_0^{c_{eff}} \frac{\partial}{\partial t} \int_0^{\xi} \gamma(\xi_0) d\xi_0 d\xi \Big] \quad . \end{aligned} \tag{3.35}$$

Contributions to this force can be grouped into non-circulatory and circulatory due to either translation, rotation, deformation or wake vortices (LEVs and TEVs):

$$F_N = F_{N_{nc}} + F_{N_t} + F_{N_r} + F_{N_d} + F_{N_v} \quad . \tag{3.36}$$

Force decomposition serves to give insight into the magnitude of each contribution to aerodynamic loads. Note that flap deflection effect is divided into rotation (as a variation in effective angle of attack, $\dot{\alpha}_\delta$) and deformation (as a change in effective chord length, $\dot{\xi}$). The normal force coefficients for the different components, normalised using $\frac{1}{2}\rho U_{ref}^2 c$, are broken down below:

1. Non-circulatory

$$C_{N_{nc}} = \frac{2\pi c_{eff}^2}{Uc} \left(\frac{3}{4} \dot{A}_0(t) + \frac{1}{4} \dot{A}_1(t) + \frac{1}{8} \dot{A}_2(t) \right) \quad . \tag{3.37}$$

2. Circulatory due to translation

$$C_{N_t} = \frac{2\pi c_{eff}}{Uc} \Big(U \cos \alpha_{eff} + \dot{h} \sin \alpha_{eff} \Big) \Big(A_0(t) + \frac{1}{2} A_1(t) \Big) \quad . \tag{3.38}$$

3. Circulatory due to rotation

$$C_{N_r} = -\frac{2}{U^2 c} \int_0^{c_{eff}} \Big(\dot{\alpha}(\eta(\xi) - \eta_{pvt}) + \dot{\alpha}_\delta \eta(\xi) \Big) \gamma(\xi) d\xi \quad . \tag{3.39}$$

4. Circulatory due to deformation

$$C_{N_d} = \frac{2}{U^2 c} \int_0^{c_{eff}} \dot{\xi} \gamma(\xi) d\xi \quad . \tag{3.40}$$

5. Circulatory caused by vortices

$$C_{N_v} = \frac{2}{U^2 c} \int_0^{c_{eff}} \left(\frac{\partial \phi_{TEV}}{\partial \xi} + \frac{\partial \phi_{LEV}}{\partial \xi} \right) \gamma(\xi) d\xi \quad . \tag{3.41}$$

Time derivatives $\dot{\alpha}_\delta$ and $\dot{\xi}$ are defined in Eq. (3.23).

In addition to this pressure force, a leading-edge suction force acting axial to the aerofoil in the upstream direction will play a role in the generation of aerodynamic loads. It is given by the Blasius formula (Katz & Plotkin, 2001):

$$F_S = \rho \pi c U^2 A_0^2 \quad . \tag{3.42}$$

Using the same factor to normalise it yields the suction force coefficient:

$$C_S = 2\pi A_0^2 \quad . \tag{3.43}$$

Aerodynamic coefficients are normally derived in the free stream coordinate system, so the resulting component normal to the incoming flow is the lift, and the parallel component is the drag:

$$C_L = C_N \cos\alpha_{eff} + C_S \sin\alpha_{eff} \quad , \tag{3.44a}$$

$$C_D = C_N \sin\alpha_{eff} - C_S \cos\alpha_{eff} \quad . \tag{3.44b}$$

Finally, the pitching moment (nose-up positive) is obtained as:

$$M = \int_0^{c_{eff}} \Delta p(\xi)(\xi_{pvt} - \xi) d\xi \quad . \tag{3.45}$$

Upon substituting Eq. (3.34), and normalising with $\frac{1}{2}\rho U_{ref}^2 c^2$, the pitching moment coefficient around the pivot axis results:

$$\begin{aligned}C_M = C_N \frac{c_{pvt}}{c}\cos\alpha_\delta - \frac{2\pi c_{eff}^2}{Uc}\left(\frac{7}{16}\dot{A}_0(t) + \frac{11}{64}\dot{A}_1(t) + \frac{1}{16}\dot{A}_2(t) - \frac{1}{64}\dot{A}_3(t)\right) \\ -\frac{2\pi c_{eff}^2}{Uc^2}\left(U\cos\alpha_{eff} + \dot{h}\sin\alpha_{eff}\right)\left(\frac{1}{4}A_0(t) + \frac{1}{4}A_1(t) - \frac{1}{8}A_2(t)\right) \\ +\frac{2}{U^2c^2}\left[\int_0^{c_{eff}}\left(\dot{\alpha}(\eta(\xi) - \eta_{pvt}) + \dot{\alpha}_\delta\eta(\xi) - \dot{\xi} - \frac{\partial\phi_{TEV}}{\partial\xi} - \frac{\partial\phi_{LEV}}{\partial\xi}\right)\gamma(\xi)\xi d\xi\right] \quad .\end{aligned} \tag{3.46}$$

3.3 Variable-camber CFD model

Reference data is necessary to assess the performance of a low-order model, be it from high-fidelity simulations or from experiments. While it is relatively easy to come by data from the literature for pitching/plunging aerofoils in the flow regime of interest for this work, Reynolds numbers $\mathcal{O}(10^4)$, it is not that common to find similar data for aerofoils undergoing arbitrary variations in camber. To obtain the required data a program for validation was designed based on high-fidelity computational fluid dynamic simulations. A CFD model for a dynamic trailing-edge flap was developed using an in-house version of the open-source software OpenFOAM. Validation of the CFD model itself was constrained to available data in the literature. Considering the framework on which the content of this thesis is placed (low Reynolds number flows and high reduced rates of motion), the best fit was found in the experiments carried out by Medina et al. (2017), where the kinematics profile prescribed to the flap consisted of a smoothed ramp-hold manoeuvre. This was recommended by the AIAA FDTC Low Reynolds Number Discussion Group as a set of canonical motions (see also §5.3.1), in considering harmonic kinematics less conducive to the study of rapid manoeuvres, of interest to MAV applications (Ol et al., 2010).

The aerofoil's geometry for the CFD mesh was hence constructed following the experimental model used in Medina et al. (2017): a NACA 0006 profile with a chord length of 20cm, equipped with a DTEF hinged at the mid-chord, $\frac{c_f}{c} = 0.5$. Details to define the hinge gap were provided by the author of the experiments, and were closely followed to create the mesh, but have not been included here without his consent.

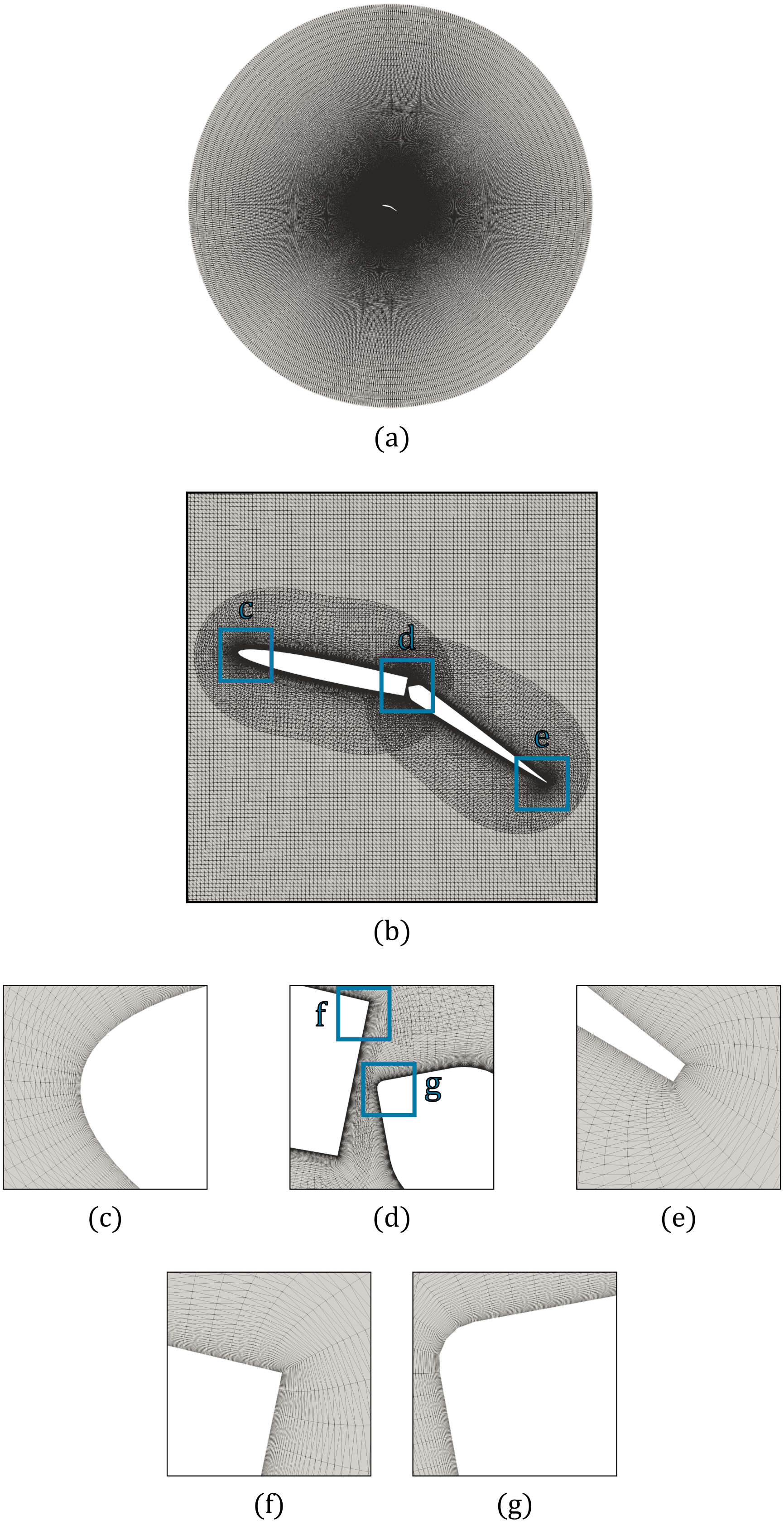

(a)

(b)

(c) (d) (e)

(f) (g)

Figure 3.4: Details of the CFD mesh: (*a*) complete fluid domain, (*b*) overset-mesh strategy adopted for multi-element configurations (body-fitted and background meshes), (*c*) leading edge, (*d*) hinge gap, (*e*) trailing edge, (*f*) rear part of main element and (*g*) front part of flap.

One of the main challenges to be faced in simulating multi-body problems is the meshing. To enable independent prescribed kinematics for each moving part (main element and trailing-edge flap) an overset mesh approach, known as the Chimera technique, was adopted. The grid system is made up of geometrically simple overlapping structured grids. For each moving component a high quality body-fitted curvilinear grid was built, being embedded within a coarser Cartesian grid of circular shape, as depicted in Figure 3.4(a, b). This background mesh has a diameter of 24 chord lengths. The number of cells around the main element of the aerofoil was 176, and 182 around the flap, with a fine resolution near the leading edge, hinge gap and trailing edge. This is illustrated through zoomed-in images around these regions, Figure 3.4$(c-g)$. The overset grids for both front and rear elements extend to 0.2 chord lengths in the wall-normal direction, in which 67 cells are contained. The maximum cell size in these meshes is 0.01 chord lengths. Overall, the number of cells are: $11,792$ cells for the body-fitted mesh around the main element of the aerofoil, $12,194$ cells for the body-fitted mesh around the flap and 82,500 cells for the background mesh.

The Finite Volume Method (FVM) was used to solve the time-dependent incompressible Navier-Stokes equations. A second-order backwards implicit scheme was used to discretise the time derivatives, and second-order limited Gaussian integration schemes were used for the gradient, divergence, and Laplacian terms. Pressure–velocity coupling was achieved using the Pressure Implicit with Splitting of Operators (PISO) algorithm. For turbulence closure the Spalart-Allmaras turbulence model (Spalart & Allmaras, 1992) was chosen because of its extensive and successful use in unsteady separated flow problems. All simulations performed in this work are at low Reynolds numbers, confining the effects of turbulence to the wake and leading-edge vortex.

Using this set-up for the CFD model various flap deflection cases extracted from Medina et al. (2017) were simulated. With the main element fixed at $\alpha = 0°$, a ramp-hold motion was prescribed to the flap with amplitude $\delta = 20°$ and three different reduced rates of flap deflection: $K_\delta = 0.07$ (slow), $K_\delta = 0.27$ (medium) and

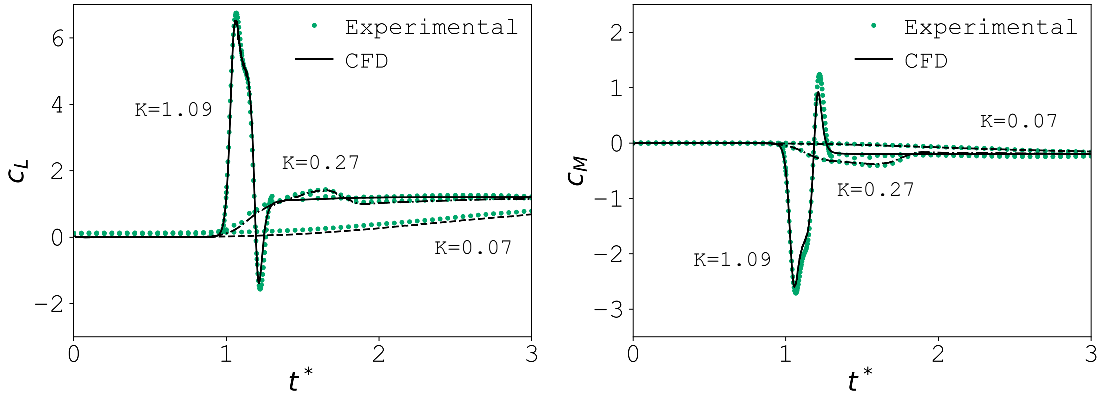

(a) (b)

Figure 3.5: Aerodynamic coefficients time history: (*a*) lift and (*b*) pitching moment. Results are from CFD (curves) and experimental data (markers).

$K_\delta = 1.09$ (fast). Flow conditions of the experiment were also replicated in the simulations: a free stream velocity of 0.2m/s and a Reynolds number based on the chord length $Re = 4 \cdot 10^4$ (experiments were conducted in water). The aerodynamic coefficients obtained for the three cases are compared in Fig. 3.5. The remarkably good agreement with experimental results, observed for all rates of flap motion, was encouraging to use this CFD model as a validation tool for the low-order model.

Finally, in order to broaden the spectrum of shape-defining parameters accessible to study foil morphing, a new arrangement was derived from the previous geometry, keeping the main geometric constraints but changing the flap length to 30% of the aerofoil's total chord (see §3.4.4 and §3.4.5).

3.4 Dynamic trailing-edge flexion

Three different sets of cases for temporal camber variations are analysed in this section to assess the performance of MDVM. Various combinations of shape-control parameters, such as the length of body deflected, the amplitude and the rate of deflection, are included to understand its limitations and prove its capability in modelling deforming foils. Firstly, the reason behind the parameters chosen is explained in detail in §3.4.1. Next, expected limitations to the model predictions are brought out in §3.4.2 based on classical fluid mechanics theory. Finally, results for the three sets are shown and thoroughly discussed in §3.4.3, §3.4.4 and §3.4.5.

3.4.1 Deformations in nature, optimal convergence

Periodic flow motions are typically described using a dimensionless number that relates oscillatory and linear fluid velocities: the Strouhal number, St. To characterise flapping-based mechanisms of locomotion where the orientation of oscillations is normal to the direction of motion, like animal propulsion (cruising bird/bat/insect flight or fish swimming), a form of the Strouhal number can be used which is based on the amplitude of flapping oscillations (Shyy et al., 2013):

$$St = \frac{fA}{U} \quad , \tag{3.47}$$

where f represents the dimensional stroke frequency of the appendage; A the peak-to-peak amplitude of its trailing edge; and U the animal's forward velocity.

If the oscillating flow is caused by trailing-edge flexion, by writing the stroke amplitude in terms of bending parameters as $A = 2\,c_f \sin\delta_{max}$, knowing the relation between angular and linear frequency $\omega = 2\pi f$, and recalling the expression for the reduced frequency $k = \frac{\omega c}{2U}$, a modified expression for the Strouhal number is yielded:

$$St_\delta = \frac{2k_\delta}{\pi}\frac{c_f}{c}\sin\delta_{max} \quad . \tag{3.48}$$

Here k_δ is the non-dimensional trailing-edge flexion frequency (flap deflection reduced frequency in this work); $\frac{c_f}{c}$ is the flexion ratio, defined as the length of appendage/body being flexed, this is from flexion point to trailing edge, relative to the total length of the appendage/body (flap-to-foil ratio in this work); and δ_{max} is the flexion angle, that the line connecting flexion point and trailing edge forms with the appendage/body symmetry line (flap deflection amplitude in this work). Figure 3.6 shows the graphic relation between parameters involved to derive the new expression for the Strouhal number.

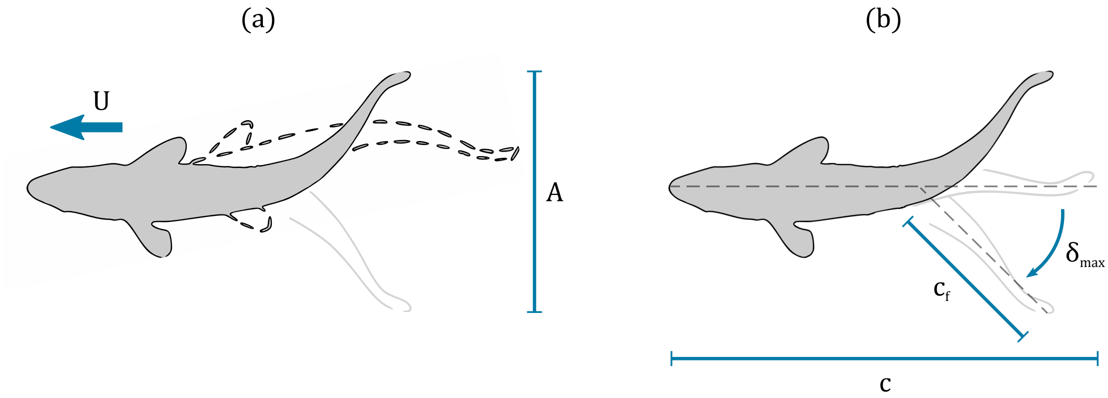

Figure 3.6: Schematic of parameters involved in different definitions of Strouhal number: (*a*) general oscillatory motion and (*b*) adapted for trailing-edge flexion.

Natural selection seems to have tuned animal cruise kinematics for high thrust production and propulsive efficiency, constraining the optimal Strouhal number observed in biological propulsion to a narrow range of $0.2 < St < 0.4$ (Taylor et al., 2003; Triantafyllou et al., 1993). Geometric configurations of natural flexible propulsors also follow similar patterns across animal taxa (Lucas et al., 2014). Existing morphometric data of bending parameters on a number of fish species identified values to which flexion ratio and flexion angle converge for all fish surveyed: bending tends to occur at about one third from the trailing edge of the fish tail, with an angle of 30° (Hang et al., 2022; Lucas et al., 2014). Wing-shape data collected from bats flight revealed the extreme degree of active deformation exhibited in their wings at low flight speeds (Von Busse et al., 2012), with trailing-edge flexion angles as high as 20° to 45° (see Fig. 2.4*a*). Camber corresponding to these values varies from 0.1 to 0.2 (see Fig. 2.4*b*), or from 10% to 20% if expressed as a percentage of the total chord length (Cheney et al., 2022; Muijres et al., 2008; M. Wolf et al., 2010). The chordwise coordinate of maximum camber obtained with the above values is 0.5, or in other words, the flexion point (flap hinge in this work) is located at the mid chord for these wings. Similar deformation traits, camber ≥ 10% around the mid chord, have also been recorded for passively cambered wings (see Fig. 2.5) in all flight modes: gliding raptors (Cheney et al., 2021), flapping owls (T. Wolf &

Table 3.1: Bending parameters used to characterise deformation on each studied case: flexion ratio, flexion amplitude, reduced flexion frequency, Strouhal number.

	$\frac{c_f}{c}$	$\delta_{max}[°]$	k_δ	St_δ
case A	0.5	1	0.5	0.003
case B	0.3	20	π	0.21
case C	0.5	20	π	0.35
case D	0.3	45	$\pi/2$	0.21
case E	0.5	45	$\pi/2$	0.35

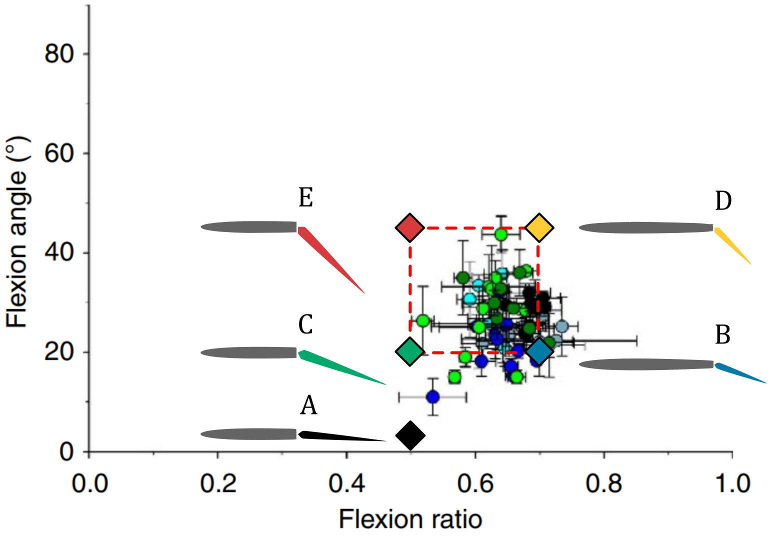

Figure 3.7: Comparison of bending parameters for optimal performance in fish swimming and flapping-wing flight (adapted from Lucas et al. (2014) with permission) and those used for studied cases. Note that the flexion ratio represented in the x-axis is the complementary of that in Eq. (3.48). Rather than the length of propulsor being bent, the distance from the leading edge to the point at which flexion occurs is stated in the graph.

Konrath, 2015), hovering hummingbirds (Maeda et al., 2017); and on aeroelastic insect wings (Walker et al., 2009, 2010; Zheng et al., 2013).

To give an idea of the magnitude of flap deflection needed to achieve equivalent deformations, a camber of $\frac{\eta_{max}}{c} = 0.1$ for a flexion ratio of $\frac{c_f}{c} = 0.5$ translates into a flexion angle of $\delta_{max} = 20°$ (see Eq. (3.13)). This value is used to define medium amplitude deformation cases studied in this section, whereas the maximum value observed in bat flight, $\delta_{max} = 45°$, is taken to show the performance of the low-order model in large-amplitude deformation scenarios. Following guidelines on biological bending parameters, two different flexion ratios are considered for each set of cases, $\frac{c_f}{c} = 0.3$ and $\frac{c_f}{c} = 0.5$. The reduced frequency of trailing-edge flexion is adjusted for each of them in order to keep the Strouhal number given in Eq. (3.48) within the optimal range observed in nature. An additional case for very small deformations at low rate has been included. The aim is to prove the enhancement in aerodynamic loads estimation when the modified Kutta condition (see §3.2.2) is implemented in the model. Since studied cases have been selected aiming to cover as wide a range of real data observed in natural bending as possible, Fig. 3.7 illustrates where these cases lie according to their flexion amplitude and ratio when compared to data from Lucas et al. (2014). Parameters defining all cases are listed in Table 3.1.

The argument in favour of choosing the flexion ratio $\frac{c_f}{c} = 0.5$ is further reinforced by recent experimental investigations involving trailing-edge flap deflections with that configuration (Medina et al., 2017). Research efforts to study the same fluid problem from different perspectives, theoretical and experimental, can be complemented if the same set-up is used for both. Indeed, experimental data generated by one of these research studies has served to build and validate the CFD model, which has itself been used throughout this thesis as a validation tool for the low-order model. All details have been described in §3.3.

3.4.2 Drag on deforming bodies

Looking at the source of aerodynamic drag production, contributions to this load are traditionally divided in two major categories: lift-induced drag, and parasitic or profile drag (Meseguer & Sanz-Andrés, 2012). The former is a direct consequence of the incoming air flow being redirected by the moving object, and it is distinctive of lifting bodies. The two-dimensionality of the problem in question discards this source of drag. To the later belong the so-called skin friction drag and the form drag. The first one is directly proportional to the wetted surface (area, or skin, in contact with the fluid). The second one depends on the body shape (wake width). It is related to flow separation, and characteristic of bluff bodies. In the separated region behind the body a low pressure zone forms, which translates into a backwards force

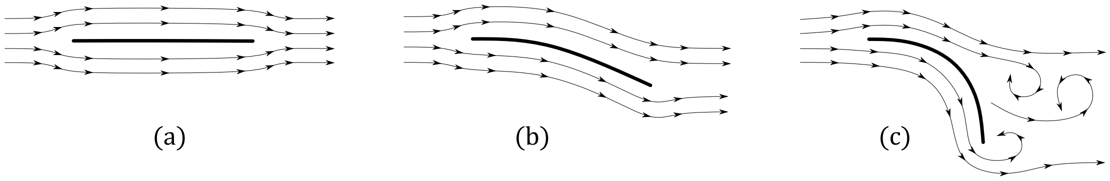

Figure 3.8: Streamlining effect on viscous drag components: (*a*) totally streamlined body over which skin friction drag prevails, (*b*) slightly less streamlined body with both drag components and (*c*) bluff body dominated by form drag.

or drag. The larger the cross-section the wider the wake behind, and the higher the drag. In this sense it is often considered a type of pressure drag due to separation. In this research there are no compressibility effects, so the wave drag contribution, caused by shock waves on transonic and supersonic flight regimes, is null.

Therefore, the only two drag components to be considered in the fluid mechanics problem dealt with in this research seem to be of viscous origin: the skin friction drag and the form drag. In streamlined bodies (an aerofoil at low angle of attack for example) the skin friction drag prevails over the form drag. As the bluntness of the body increases the effect of friction begins to fade and flow separation makes the form drag to dominate. This relation between the shape of the object and its wake is schematised in Fig. 3.8.

Among the assumptions made in the derivation of the theoretical model is that of potential flow. The above-cited components cannot be estimated under this simplification, and the total drag force on an aerofoil moving with a constant velocity relative to the fluid will be zero, statement known as the D'Alembert's Paradox. To mathematically prove that the aerodynamic drag coefficient predicted by the low-order model would indeed be zero in that case, by getting rid of the non-stationary terms in Eqs. (3.35) and (3.42), the normal and suction force coefficients become:

$$C_N = 2\pi \cos\alpha_{eff}\left(A_0 + \frac{A_1}{2}\right) \quad , \tag{3.49a}$$

$$C_S = 2\pi A_0^2 \quad . \tag{3.49b}$$

And bearing in mind that $A_0 = \sin\alpha_{eff}$ and $A_1 = A_2 = ... = 0$ for that case:

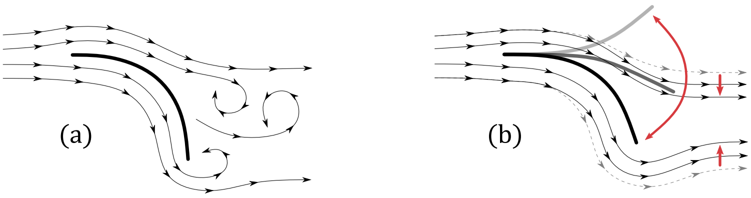

Figure 3.9: Morphing effect on flow separation and wake width: (*a*) steady foil exhibiting separated flow downstream and (*b*) time-varying camber foil avoiding separation and narrowing the wake through dynamic trailing-edge flexion.

$$C_N = 2\pi \cos\alpha_{eff} \sin\alpha_{eff} \quad , \tag{3.50a}$$

$$C_S = 2\pi \sin^2\alpha_{eff} \quad . \tag{3.50b}$$

Hence, the lift and drag coefficients from Eq. (3.44) result:

$$C_L = 2\pi \sin\alpha_{eff} \quad , \tag{3.51a}$$

$$C_D = 0 \quad . \tag{3.51b}$$

In unsteady foils however, integration of the pressure distribution over the surface given in Eq. (3.34) unveils further contributions to the drag force. Motion kinematics and shape variations, along with the wake of vortices developed downstream, deflect the airflow coming in to the foil to generate lift and drag. This combination of unsteady aerodynamics effects gives rise to a drag component whose origin is not viscosity, but can rather be thought of as a potential contribution similar to the lift-induced drag for 3D problems. Non-zero drag predictions are therefore expected with the mathematical model presented in this chapter.

Shaping the body might avoid flow separation and lead to wake narrowing, therefore reducing the form drag. This can be achieved through dynamic deformation, as schematised in Fig. 3.9. Narrower wakes behind deforming bodies are due to the flow turning in the opposite direction to the bending surface (Gerontakos & Lee, 2008; Rennie & Jumper, 1996), resulting in a persistence of the attached flow state. Viscous drag will then be mainly due to skin friction. Unsteady motions selected

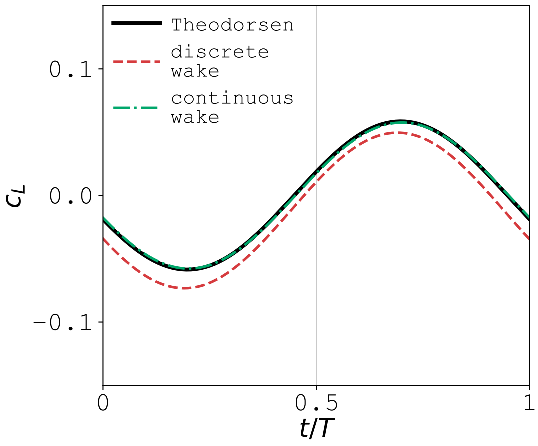

Figure 3.10: Lift coefficient for one cycle of harmonic trailing-edge flap deflections with amplitude $\delta_{max} = 1°$, reduced frequency $k_\delta = 0.5$ and flexion ratio $c_f/c = 0.5$. Results are from Theodorsen's classical theory (—), discrete representation of wake vorticity shed in MDVM (----) and continuous representation (-·-·).

for analysis in this section ensure the flow remains fully attached to the foil, with the exception of the last set of cases, where flow separates either over the moving flap or at the foil's leading edge. The later will be revisited in §5.4 to showcase the improvement in capturing subtle flow separation at the leading edge with the new formulation of vorticity-shedding rate introduced in Chapter 5.

The context on drag modelling provided in this section will ease the aerodynamic drag coefficient analysis carried out in the following sections.

3.4.3 Small-amplitude deformations

Trailing-edge flap deflections are prescribed on an aerofoil moving at a constant velocity with zero angle of attack. Flap kinematics are defined, for all three set of cases, by a sinusoidal wave:

$$\delta = \delta_{max} \sin(\omega t) \quad , \tag{3.52}$$

where δ_{max} represents the amplitude of the motion; and the angular frequency, ω, is twice the value of the reduced frequency, k_δ. The value of each parameter is listed in Table 3.1 for all cases studied.

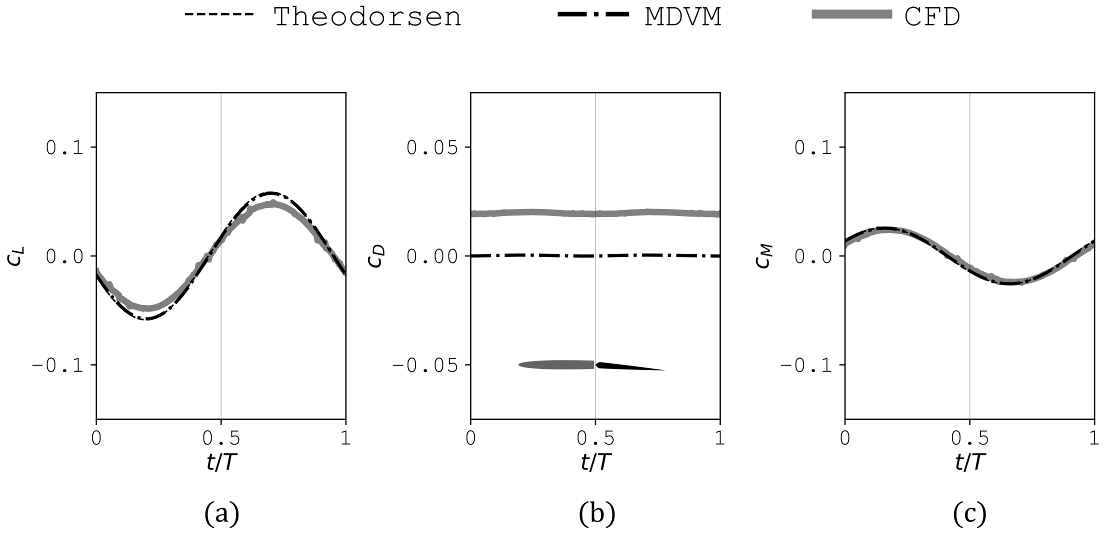

Figure 3.11: Aerodynamic coefficients for one cycle of harmonic trailing-edge flap deflections with amplitude $\delta_{max} = 1°$, reduced frequency $k_\delta = 0.5$ and flexion ratio $c_f/c = 0.5$: (*a*) lift, (*b*) drag and (*c*) pitching moment at the leading edge. Results are from Theodorsen's classical theory (----), MDVM (-·-·) and CFD (——).

Before going into detail, the effect of wake modelling on the aerodynamic loads is analysed in Fig. 3.10, where the lift coefficient is presented for one cycle of flap deflection (after solution has converged) according to parameters under case A in Table 3.1. If a continuous distribution of vorticity is adopted to represent the wake shed at the trailing edge in the current time step, which is derived from the exact Wagner solution (see §3.2.2), the lift coefficient is observed to perfectly match Theodorsen's classical theory. If, instead, a point vortex or regularised vortex blob (discrete representation) is used to account for shed wake vorticity, as is typically formulated in unsteady thin-aerofoil theory (Ramesh et al., 2013), there is a discontinuity in the vortex sheet across the trailing edge. The resultant lift coefficient exhibits an offset compared to the analytical solution.

Because of the very small amplitude and reduced frequency of flap deflection in this first case, the potential contribution to drag from the unsteadiness of the problem is nearly null. On the contrary, as CFD simulations do take viscosity into account, the drag force acting on a real fluid is not zero. The disagreement between the morphing discrete-vortex model and CFD results is evident in Fig. 3.11(*b*). Just as it has been shown for the lift in Fig. 3.10 (which coincides with Fig. 3.11*a*),

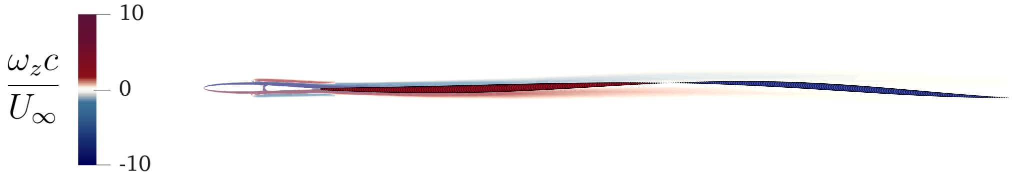

Figure 3.12: Spatial distribution of vortex particles overlapping normalised vorticity contours extracted from CFD simulations, for one cycle of harmonic trailing-edge flap deflections. Kinematics parameters are: amplitude $\delta_{max} = 1°$, reduced frequency $k_\delta = 0.5$ and flexion ratio $c_f/c = 0.5$.

the moment coefficient at the leading edge for the discrete-vortex model and the analytical solution from classical theory matches, presenting a very good agreement with the computational results, as observed in Fig. 3.11(*c*).

Out-of-plane vorticity contours from CFD and vortex particles from MDVM are shown overlaid in Fig. 3.12. The small amplitude of flap deflection does not give rise to wake roll-up into vortices, but the light oscillations are properly reproduced by the low-order model.

3.4.4 Medium-amplitude deformations

As the amplitude or rate of flap deflection increases, the potential contribution to drag due to the deformation of the immersed body becomes more noticeable (recall §3.4.2). To illustrate this, for case C in Table 3.1, drag coefficient estimations from both LOM strategies and CFD simulations are compared in Fig. 3.13. Predictions made by MDVM implemented with the variable chord line get closer to computations made with the viscous CFD model, still being slightly smaller in magnitude. This deviation was expected and attributed to the skin friction drag only accounted for in the high fidelity flow simulation. Some noise is observed in the CFD curve, whose origin is in the interpolations happening at the interfaces between the different overlapping meshes (three grids in some regions, see Fig. 3.4*b*). It could be removed by filtering out high frequencies. Worthy of note is the disparity between predictions made by the new variable chord line and the classical fixed chord line approaches. The new definition of the chord line introduced in this chapter clearly improves upon

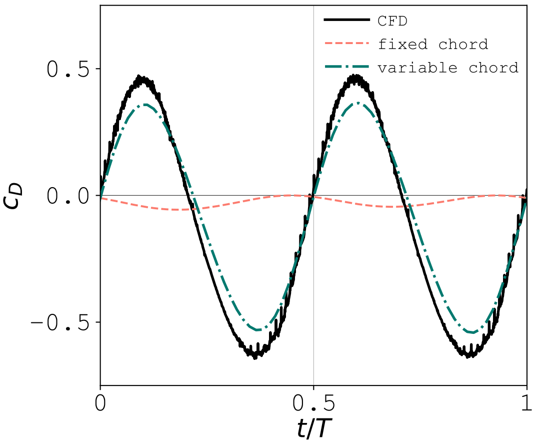

Figure 3.13: Drag coefficient for one cycle of harmonic trailing-edge flap deflections with amplitude $\delta_{max} = 20°$, reduced frequency $k_\delta = \pi$ and flexion ratio $c_f/c = 0.5$. Results are from CFD (——), MDVM with fixed chord line (----) and with time-varying chord line (-·-·).

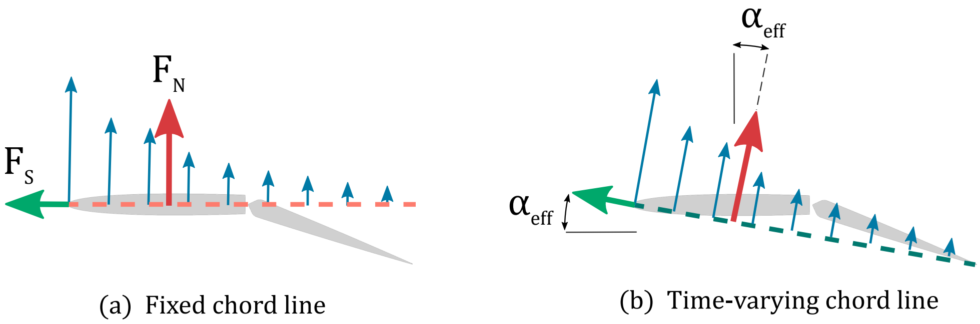

(a) Fixed chord line

(b) Time-varying chord line

Figure 3.14: Chord line definition effect on pressure and suction force vectors orientation. Arrows indicate: pressure distribution (blue), normal force (red) and suction force (green). A fixed chord line approach (*a*) results in lift and thrust generation, whereas a time-varying chord line (*b*) tilts the normal force vector to produce also drag.

the classical method, which provides an almost zero drag coefficient. Furthermore, that value is negative during the complete cycle of flap deflection (pure thrust).

The reason lies behind the orientation of the pressure and suction force vectors relative to the incoming flow, exhibited in the sketch of Fig. 3.14. Observing the pressure distribution (blue arrows) along the foil with a fixed chord line, Fig. 3.14(*a*), in the absence of pitching kinematics the resulting normal force vector (red arrow) stays always perpendicular to the direction of motion. As a consequence only lift force is produced, and the sole contribution to drag is owed to the suction force. Since this other vector has the direction of motion, a propulsive or negative

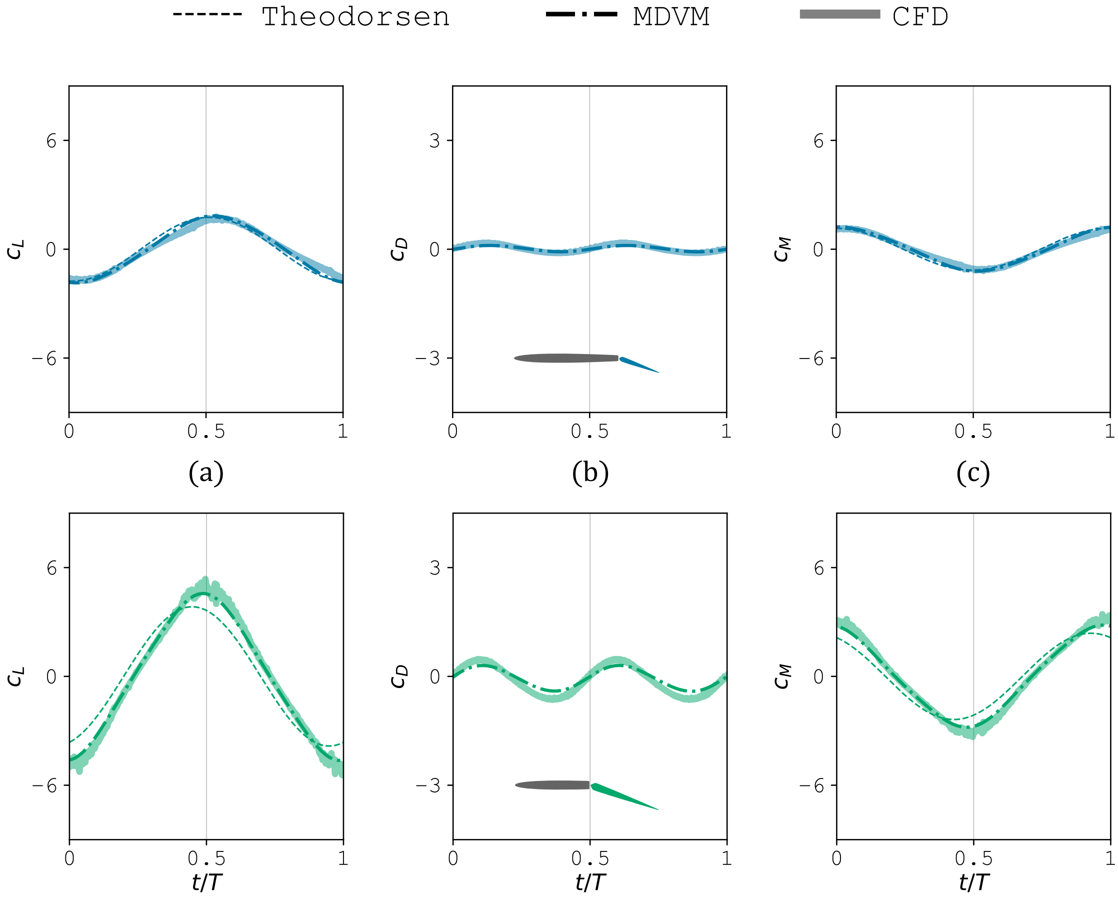

(a) (b) (c)

(d) (e) (f)

Figure 3.15: Aerodynamic coefficients for one cycle of harmonic trailing-edge flap deflections with amplitude $\delta_{max} = 20°$, reduced frequency $k_\delta = \pi$ and flexion ratios $c_f/c = 0.3$ and $c_f/c = 0.5$ (respectively): (a,d) lift, (b,e) drag and (c,f) pitching moment at the leading edge. Results are from Theodorsen's classical theory (----), MDVM (-·-·-) and CFD (——).

drag force is generated, as depicted in Fig. 3.13. If on the contrary the chord line is allowed to rotate with deflections of the trailing-edge flap, in other words, a time-varying chord line is considered, Fig. 3.14(b), the angle of attack of the aerofoil against the free stream direction is modified in time (see Eqs. (3.9) and (3.10)), tilting the pressure force vector to produce both, lift and drag.

Having justified the improvement in aerodynamic performance achieved with a variable chord line definition, this is the strategy implemented in MDVM to provide the remaining results of this section. Examining the lift and moment coefficients in Fig. 3.15, it is observed that both, MDVM and the classical theory, track very closely

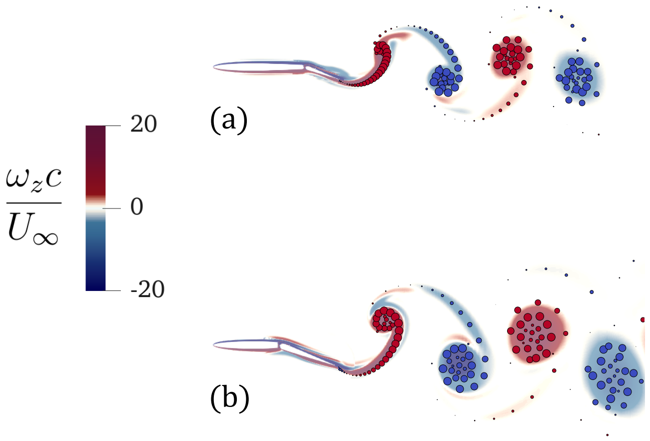

Figure 3.16: Spatial distribution of vortex particles overlapping normalised vorticity contours extracted from CFD simulations, for two cycles of harmonic trailing-edge flap deflections. Kinematics parameters are: amplitude $\delta_{max} = 20°$, reduced frequency $k_\delta = \pi$ and flexion ratios $c_f/c = 0.3$ (a) and $c_f/c = 0.5$ (b).

CFD curves for the smallest flexion ratio, Fig. 3.15(a, c). Whereas for the largest flexion ratio, Fig. 3.15(d, f), Theodorsen theory results deviate from the viscous flow calculations in magnitude and in phase, but MDVM keeps a well agreement.

Representation of the flow field via the spatial distribution of vorticity is exhibited in Fig. 3.16, with low-order predictions and high-fidelity computations overlapping. With the parameters used to define this case, deflection of the trailing-edge flap imparts a rotational motion to the fluid strong enough for the wake to roll-up into coherent structures. Two single vortices with different rotation sense are shed from the trailing edge during each flap deflection cycle, a vortex shedding pattern classified as 2S-mode by Williamson and Roshko (1988). The wake behind the foil exhibits a reverse Bénard–von Kármán vortex street, where vortices are organised in two rows such those with negative vorticity (clockwise rotation) are located below the wake centre line, and those with positive vorticity (counter-clockwise rotation) above it. In this configuration vortices induce on each other a downstream jet-like velocity component (Jones et al., 1998). This thrust-indicative wake pattern is characteristic of flapping-based propulsion, like aquatic-locomotion, and has been documented for pure plunging and pure pitching aerofoils before (Freymuth, 1988). The location and size of each vortex is captured by MDVM with great accuracy.

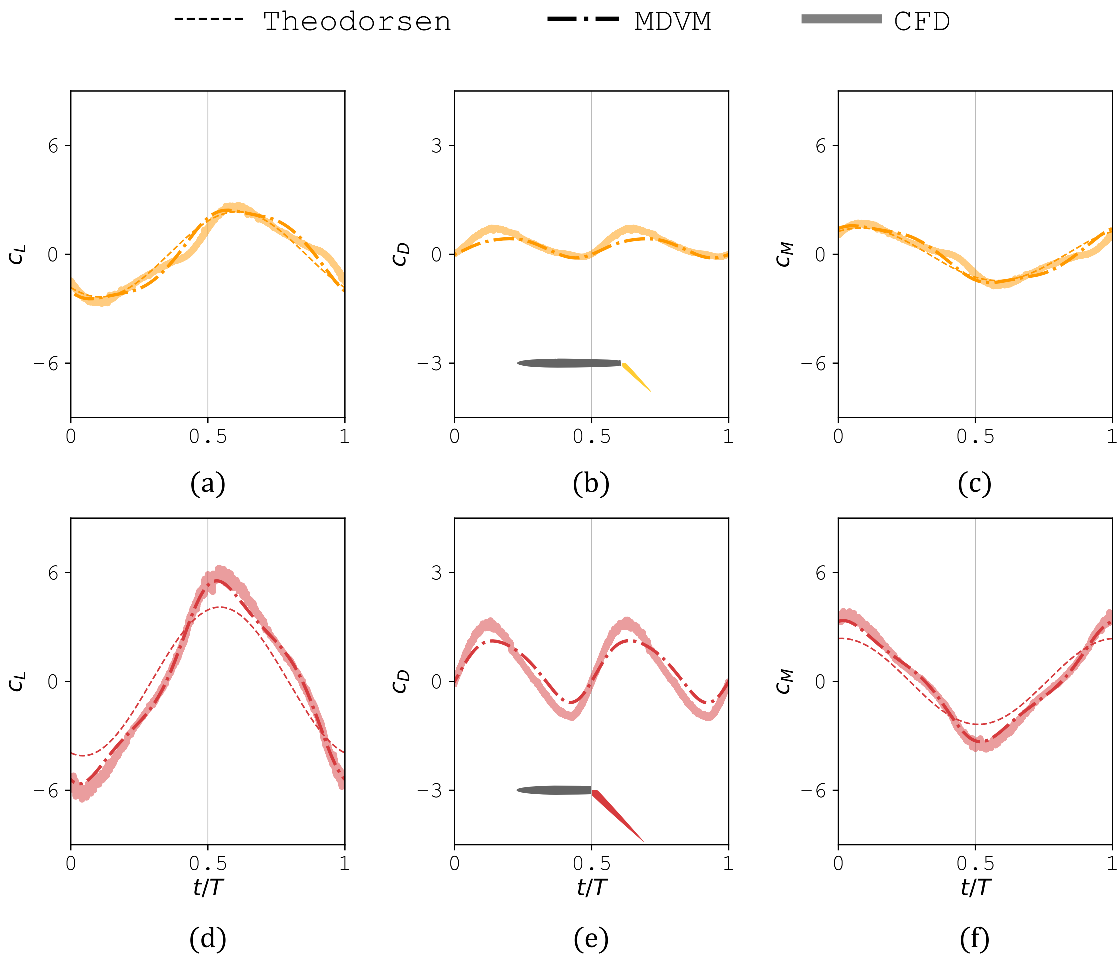

Figure 3.17: Aerodynamic coefficients for one cycle of harmonic trailing-edge flap deflections with amplitude $\delta_{max} = 45°$, reduced frequency $k_\delta = \pi/2$ and flexion ratios $c_f/c = 0.3$ and $c_f/c = 0.5$ (respectively): (a, d) lift, (b, e) drag and (c, f) pitching moment at the leading edge. Results are from Theodorsen's classical theory (----), MDVM (-·-·) and CFD (——).

3.4.5 Large-amplitude deformations

Further increasing the deflection amplitude, the typical sine waveform in the temporal evolution of aerodynamic coefficients, characteristic of harmonic motions with small-medium amplitudes, begins to distort as evinced in Fig. 3.17. For the smallest flexion ratio, lift and moment analytical and numerical calculations exhibit a smoother curve distortion than CFD results, Fig. 3.17(a, c). It is important to note the appearance of flow separation over the aerofoil in CFD simulations for this set of cases, which might be the reason behind the differences observed. For this

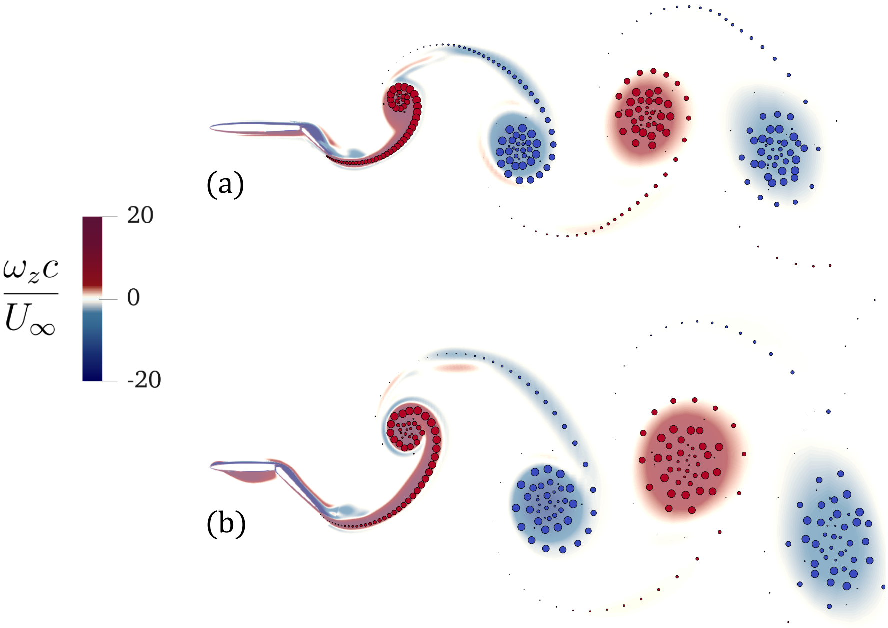

Figure 3.18: Spatial distribution of vortex particles overlapping normalised vorticity contours extracted from CFD simulations, for two cycles of harmonic trailing-edge flap deflections. Kinematics parameters are: amplitude $\delta_{max} = 45°$, reduced frequency $k_\delta = \pi/2$ and flexion ratios $c_f/c = 0.3$ (a) and $c_f/c = 0.5$ (b).

smaller bending ratio separation occurs over the flap (blue region in Fig. 3.18a). The source of separation seems to be the hinge gap, and since the geometry as modelled by theory and MDVM has no discontinuity in this area results are expected to differ to some extent. As for the drag coefficient, Fig. 3.17(b, e), the magnitude predicted by MDVM remains somewhat lower than CFD for the reason explained in §3.4.4. On the other hand, large flexion ratios combined with large trailing-edge deflections increase the effective angle of attack experienced by the foil enough for the flow to separate at the leading edge, as noticed in Fig. 3.18(b). Leading-edge vorticity modelling has been omitted in the development of MDVM presented in this chapter and this phenomenon will be analysed later in §5.4. Nonetheless, the low-order model manages to reproduce CFD results with great success, whereas lift and moment curves from classical theory differ in magnitude and shape, Fig. 3.17(d, f).

Visualisation of vorticity contours reveals again a propulsive vortical signature in the wake. A similar arrangement of vortices to that of medium-amplitude deformation cases is observed in Fig. 3.18, with a slightly larger separation between vortex pairs. Despite flow separation not modelled in MDVM it seems to have a minor effect on vortices shed, and the model reproduces with exactness the wake pattern in terms of placement and size of vortices.

3.5 Summary

The main goal of this chapter has been to develop a low-order aerodynamic model to simulate the unsteady flow response to bodies undergoing arbitrarily large temporal camber variations.

To achieve this, analytical predictions based on an adapted potential-flow theory for unsteady aerofoils have been combined with numerical methods using discrete-vortex elements. Leveraging a widely validated discrete-vortex model for rigid wings, the extension to variable-camber wings has been possible by modifying the boundary condition from unsteady thin-aerofoil theory, where time dependency is accounted for in the study of unsteady flows.

In pursuance of reproducing the extreme degree of bending observed in nature, the majority of the chapter has been devoted to extend the range of applicability of thin-aerofoil theory, originally conceived for small flow disturbances. To address the restriction imposed on chordwise deformation with the small-amplitudes assumption, a time-varying chord line is proposed in this work as the curve where the zero-normal flow boundary condition has to be satisfied. Being defined as the line which connects the instantaneous position of leading and trailing edges, this new effective chord line is allowed to vary in time due to trailing-edge deflection. The maximum camber ratio is thus reduced for large amplitudes, lessening the error associated when transferring the boundary condition from the camber line, and increasing the accuracy on aerodynamic loads estimation.

Furthermore, no assumptions of planar wakes (necessary in fully closed-form theories) are made in the numerical scheme, which enables to capture wake distortion and shed of trailing-edge vortices. The model is valid for arbitrary variations in free stream velocity (external perturbations like gusts), kinematics (rapid plunge and pitch manoeuvres) and geometry (chordwise deformations).

A set of harmonic trailing-edge deflection cases has been used to assess the performance of the new morphing discrete-vortex model. Various combinations of shape-control parameters have been tested, which include the flexion ratio, the amplitude and rate of deflection. Regardless of the flexion ratio, results for small-amplitude deflections evince noticeable differences with CFD results in terms of drag force. The dominant component of drag in these scenarios is viscous in origin, which is not modelled in MDVM. As the amplitude of deflection increases the viscous drag loses importance in favour of the form drag, and results improve. However, this is only the case if the time-varying chord line approach introduced in this chapter is considered. Because this way the chord line is allowed to rotate with flap deflections, the effective angle of attack seen by the aerofoil varies in time. This variation tilts the pressure force vector against the incoming free stream, which results in lift and drag generation. If on the contrary the fixed chord line approach is followed, the pressure force vector remains perpendicular to the direction of motion, producing lift only (the contribution to horizontal force is due to the suction force, with positive sign).

In terms of lift and moment, MDVM predictions reproduce with great success the temporal evolution computed with CFD, including the distortion from the typical sine waveform observed for large amplitudes, which the classical theory does not.

Lastly, flow visualisation through vorticity contours showcases the capacity of MDVM in modelling wake roll-up into coherent structures, capturing remarkably well the location and size of vortices shed from the trailing edge at every cycle.

In short, the low-computational cost physics-based model developed in this chapter performs simulations of unsteady flows past deforming bodies, including non-linear aerodynamic phenomena such as vortex shedding, in the order of seconds in a personal laptop. It lays the groundwork for vortex-dynamics characterisation in response to shape variations, studied in Chapter 6.

Frustra fit per plura quod potest fieri per pauciora.

[It is futile to do with more things that which can be done with fewer]

— William of Ockham

4

MORPHING: ANALYTIC APPROACH

4.1 Introduction

Theoretical predictions of aerodynamic loads have been published in literature for the most fundamental unsteady problems: impulsively started aerofoils (Wagner, 1925), oscillating aerofoils (Theodorsen, 1935), aerofoil response to sharp-edge gusts (Küssner, 1936), and harmonic gusts (Sears, 1941). Although the strength of the vortex sheet is used to compute the aerodynamic loads, its analytical prediction was not explicitly derived in these works.

Insight into the fundamental nature of the flow field can be gained by observing the balance between circulatory and non-circulatory contributions, which is possible having an analytic expression of the vortex sheet strength. It also is practically useful, owing to a broad interest on rapidly obtaining accurate unsteady pressure distributions over wings undergoing time-varying kinematics. In addition, it enables to obtain closed-form expressions for the contribution to Fourier coefficients of the different motion-defining parameters.

Progress along these lines has recently been possible due to available computational resources in modern times, out of reach to aerodynamicists who developed their theories a century ago limited to the means of the time. A numerical method to compute certain complex coefficients was presented by Epps and Roesler (2018), which allowed them to obtain analytic predictions of the vortex sheet strength in the four seminal unsteady aerodynamics problems before cited.

Owing to the interest of the dissertation on morphing, the attention is focused on Theodorsen's problem, an aerofoil with three independent degrees of freedom: pitch, plunge and flap motions. This chapter aims to obtain simple forms of the Fourier coefficients for this basic problem. The derivation for the vortex sheet strength of Epps and Roesler (2018) is here adapted to the frame of reference used in unsteady thin-aerofoil theory. This allows to obtain the sought coefficients through comparison with the bound vorticity distribution defined in Chapter 3.

This chapter is structured as follows: in §4.2 the basis is set for the ultimate derivation of Fourier coefficients, starting in §4.2.1 with a definition of the problem and the transformation variables needed to change the frame of reference; to which follows a decomposition of vortex sheet strength into individual contributions of motion parameters, for the non-circulatory term in §4.2.2, the circulatory term due to motion in §4.2.3, and the wake-induced term in §4.2.4; simple forms of the Fourier coefficients are then provided in §4.3, where for the first two coefficients the dependency on the reduced frequency is exhaustively analysed in §4.3.1, and the expression for the rest of coefficients is subsequently given in §4.3.2; finally, the chapter is summarised in §4.4.

4.2 Vortex sheet strength

Different strategies can be followed to solve the potential flow problem. The flow can be partitioned into a non-circulatory part, which fulfils the zero-normal flow boundary condition but not the Kutta condition, plus a circulatory part due to the surface of discontinuity behind the wing, which satisfies the last condition. This strategy was adopted by Theodorsen (1935). An alternative flow partition makes a distinction between the solution obtained ignoring the effect of the wake, the so-called quasi-steady part, which depends only on the instantaneous relative velocity of the aerofoil and the air (contrary to the non-circulatory term in the previous approach, this part does enforce the Kutta condition), and the solution

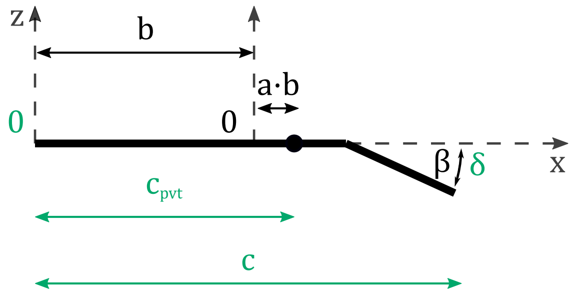

Figure 4.1: Schematic of variables used to define the aerofoil-flap problem according to: Theodorsen (1935) in black, and unsteady thin-aerofoil theory in green.

that accounts for the wake-induced velocity. This partitioning strategy was followed by Von Karman and Sears (1938). Despite the different formulation, the total flow field is the same in both approaches. For convenience, the first flow partitioning is adopted in this section, where the intention is to derive the vortex sheet strength for Theodorsen's problem in the desired frame of reference. In a later step, the quasi-steady term mentioned in the second strategy is formed to enable comparison of terms with unsteady thin-aerofoil theory.

4.2.1 Problem kinematics and frame of reference

There is some diversity within the literature of unsteady foils in the notation adopted for kinematics parameters. The point taken as the origin of the body-fixed frame of reference used to define the geometry also differs between studies. As opposed to the convention adopted by Birnbaum (1924) for its theory of thin wing sections, where the aerodynamic centre is taken as the origin of the coordinate system; or that by Theodorsen (1935), in which the origin lies midway between the leading and the trailing edge; for unsteady thin-aerofoil theory the origin is fixed at the aerofoil leading edge. Values of the non-dimensional chordwise coordinate of the leading edge and trailing edge are, respectively, $-\frac{1}{2}$ and $\frac{3}{2}$ in the first case; -1 and 1 in the second case; and 0 and 1 in the last case. The schematic in Fig. 4.1 illustrates these differences for the cases of Theodorsen and UTAT.

Mathematical representation of the angle deflected by a lifting surface (either ailerons or trailing-edge flaps) is often time assigned the Greek letter β or δ. Intending to ease the follow-up of the mathematical development in this chapter, given that Theodorsen's outcomes are taken as starting point the framework of his work is adhered to, and β instead of δ is used to represent flap deflections (see Fig. 4.1). The use of δ will be adopted again in Chapter 5.

Harmonic motions of plunge, pitch and flap deflections are defined in complex variable as:

$$h(t) = h_0 \, e^{i\omega t} \quad , \tag{4.1a}$$

$$\alpha(t) = \alpha_0 \, e^{i\omega t + \phi} \quad , \tag{4.1b}$$

$$\beta(t) = \beta_0 \, e^{i\omega t + \psi} \quad , \tag{4.1c}$$

where h_0, α_0 and β_0 denote the complex amplitude of each degree of freedom; $\omega = \frac{2Uk}{c}$ is the angular frequency of the sinusoidal wave, with k the reduced frequency; ϕ indicates the phase between plunge (taken as reference) and pitch motions; and ψ the phase between plunge motion and flap deflection.

Association of terms between the vortex sheet strength derived in this chapter and the bound vortex sheet strength from unsteady thin-aerofoil theory, given in Eq. (3.2), will offer straight away the Fourier coefficients in simple forms. To do so, both expressions of the vorticity distribution on the aerofoil need to be written in terms of the chordwise transformation variable, θ, in the same frame of reference. Some relations between variables used in both frameworks have to be defined.

If $\tilde{x} = -\cos\theta$ is used in the available expressions for the vortex sheet strength (Epps & Roesler, 2018), where $\tilde{x}$ indicates dimensionless chordwise coordinate, values of θ going from 0 to π trace the camber line from the leading edge ($\tilde{x} = -1$) to the trailing edge ($\tilde{x} = 1$). The reference length used to make variables non-dimensional in Theodorsen's work is the half chord, b, and in UTAT the total chord, c. Hence the equivalence $b = \frac{c}{2}$ is clear. The pitch axis in Theodorsen's framework is placed at a distance from the leading edge of $b(1 + a)$, whilst this length is c_{pvt} in UTAT. Therefore, $a = 2\frac{c_{pvt}}{c} - 1$ can be used in the expressions borrowed for the vortex sheet strength. The relation between variables is illustrated in Fig. 4.1 and summarised in Table 4.1.

Table 4.1: Equivalence between variables used in Theodorsen and UTAT frameworks.

	Theodorsen	UTAT	equivalence
flap angle	β	δ	$\beta = \delta$
chord length	$2b$	c	$b = \frac{c}{2}$
chordwise coordinate	$x = x_{UTAT} - b$	$x_{UTAT} = \frac{c}{2}(1 - \cos\theta)$	$\tilde{x} = \frac{x}{b} = -\cos\theta$
distance LE to pivot axis	$b(1+a)$	c_{pvt}	$a = 2\frac{c_{pvt}}{c} - 1$

4.2.2 Non-circulatory vortex sheet strength

The non-circulatory flow is an instantaneous response of the fluid to the motion and deformation of the aerofoil, therefore exclusive to unsteady problems. Built on the velocity potential derived by Theodorsen (1935) for an aerofoil oscillating in three degrees of freedom, Epps and Roesler (2018) came up with the following expressions to compute the effect of each individual motion/deformation parameter on the non-circulatory vortex sheet strength:

1. Vertical motion and pitch angle — $\dot{h}$, α

$$\gamma_{n_{h,\alpha}}(\tilde{x}, t) = (\dot{h}(t) + U\alpha(t))\frac{-2\tilde{x}}{\sqrt{1-\tilde{x}^2}} \quad . \tag{4.2}$$

2. Rate of rotation of the aerofoil — $\dot{\alpha}$

$$\gamma_{n_{\dot{\alpha}}}(\tilde{x}, t) = 2b\dot{\alpha}(t)\left\{\frac{1}{2}\sqrt{1-\tilde{x}^2} + \left(\frac{1}{2}\tilde{x} - a\right)\frac{-\tilde{x}}{\sqrt{1-\tilde{x}^2}}\right\} \quad . \tag{4.3}$$

3. Angle bent down by the flap — β

$$\gamma_{n_{\beta}}(\tilde{x}, t) = -\frac{2U}{\pi}\beta(t)\left\{\theta_f\frac{\tilde{x}}{\sqrt{1-\tilde{x}^2}} + \log|N| + (\tilde{x} - f)\frac{1}{N}\frac{dN}{d\tilde{x}}\right\} \quad . \tag{4.4}$$

4. Rate of flap displacement — $\dot{\beta}$

$$\begin{aligned} \gamma_{n_{\dot{\beta}}}(\tilde{x}, t) = \; & \tfrac{b}{\pi}\dot{\beta}(t)\Big\{\theta_f\sqrt{1-\tilde{x}^2} + ((\tilde{x} - 2f)\theta_f + \sin\theta_f)\tfrac{-\tilde{x}}{\sqrt{1-\tilde{x}^2}} \\ & -2(\tilde{x} - f)\log|N| - (\tilde{x} - f)^2\tfrac{1}{N}\tfrac{dN}{d\tilde{x}}\Big\} \quad . \end{aligned} \tag{4.5}$$

Here $f = \cos\theta_f$ and $N = \big(1 - \tilde{x}f - \sqrt{1-\tilde{x}^2}\sin\theta_f\big)/(\tilde{x} - f)$. The location of the hinge is indicated by θ_f. To adapt these expressions to the framework of UTAT the forms defined in Table 4.1 for $\tilde{x}$, a and b have to be used.

Logarithm approximation

The presence of logarithmic terms in Eqs. (4.4) and (4.5) might seem a cause for concern, since they become singular at the hinge, $\tilde{x} = \cos\theta_f$. Approximations in terms of only trigonometric functions are desired, so that the global expression for the vortex sheet strength will enable a direct comparison with thin-aerofoil theory to extract the Fourier coefficients sought. After applying the corresponding relations between variables, to have all functions expressed in the frame of reference of interest, these logarithmic terms take the general form:

$$L_1 = \log|N| = \log\frac{1+\cos(\theta+\theta_f)}{|\cos\theta+\cos\theta_f|} \quad , \tag{4.6a}$$

$$L_2 = \cos\theta\log|N| \quad . \tag{4.6b}$$

For the particular case where $\theta_f = \frac{\pi}{2}$, this is, a flap whose length is half the total chord of the aerofoil, the fortunate situation is given that Eq. (4.6) can be written in terms of inverse hyperbolic functions. Upon evaluation of Eq. (4.6a) under such condition we have:

$$L_1\Big|_{\theta_f=\frac{\pi}{2}} = \log\frac{1-\sin\theta}{|\cos\theta|} \quad , \tag{4.7}$$

and recurring to the following known relation:

$$\operatorname{arcsinh}\big(\tan(-\theta)\big) = \operatorname{arctanh}\big(\sin(-\theta)\big) = \log\left(\frac{1-\sin\theta}{\cos\theta}\right) \quad , \tag{4.8}$$

the logarithmic term can be equated to an inverse hyperbolic function:

$$L_1\Big|_{\theta_f=\frac{\pi}{2}} = \operatorname{arctanh}\big(\sin(-\theta)\big) \quad . \tag{4.9}$$

The same procedure applies to Eq. (4.6*b*).

Taylor series of a function $f(x)$ is an expansion into an infinite sum of terms with increasing exponent, the sum of which equals the function. When 0 is the point about which the function is expanded it is called a Maclaurin series, which for the inverse hyperbolic function of interest here is given as:

$$\operatorname{arctanh}(x) = x + \frac{x^3}{3} + \frac{x^5}{5} + \ldots = \sum_{m=0}^{\infty} \frac{x^{2m+1}}{2m+1} \quad \text{for} \quad |x| < 1 \quad . \tag{4.10}$$

Replacing Eq. (4.10) with $x = \sin(-\theta)$ in Eq. (4.9), which satisfies the range of validity since $\sin\theta \in [-1, 1]$, the logarithmic terms in the non-circulatory vortex sheet strength can be approximated, for an aerofoil-flap configuration with the hinge located at the mid chord, by summations of powers of $\sin\theta$:

$$L_1\Big|_{\theta_f=\frac{\pi}{2}} = -\sum_{m=0}^{\infty} \frac{\sin^{2m+1}\theta}{2m+1} \quad , \tag{4.11a}$$

$$L_2\Big|_{\theta_f=\frac{\pi}{2}} = -\sum_{m=0}^{\infty} \frac{\sin^{2m+1}\theta}{2m+1}\cos\theta \quad . \tag{4.11b}$$

In order to have an only-sines expression, the $\cos\theta$ in the second logarithmic term needs to be converted. The following known relation has been used:

$$\sin\big((2n-1)\theta\big)\cos\theta = \frac{1}{2}\Big[\sin\big((2n-2)\theta\big) + \sin\big((2n)\theta\big)\Big] \quad . \tag{4.12}$$

Note that this way odd terms of the Fourier sine series are replaced by even terms.

Basic algebraic operations allow to convert Eq. (4.11) into summations of terms in $\sin(n\theta)$ to the power of 1, consistent with Eq. (3.2). A binomial has been included in this final derivation to determine the coefficient of each term:

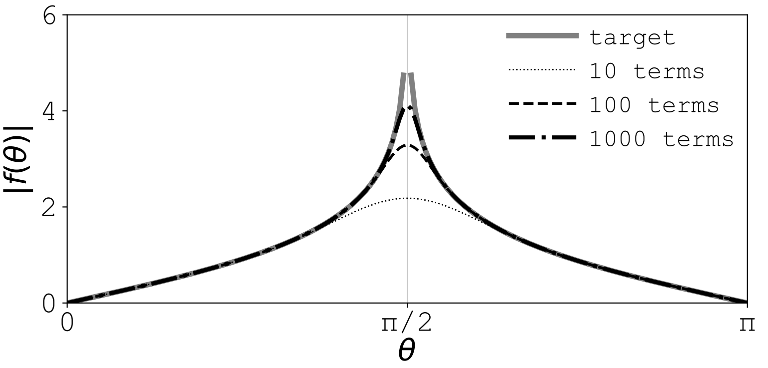

Figure 4.2: Comparison between the first logarithmic term, L_1, in its exact form (——) and its truncated series approximation keeping 10 terms (·····), 100 terms (----) and 1000 terms (-·-·).

$$L_1\Big|_{\theta_f=\frac{\pi}{2}} = -\sum_{m=0}^{N_o}\sum_{r=0}^{m}\Big[\tfrac{(-1/4)^m}{2m+1}(-1)^r\binom{2m+1}{r} \cdot \sin\big((2m-2r+1)\theta\big)\Big] \quad , \tag{4.13a}$$

$$L_2\Big|_{\theta_f=\frac{\pi}{2}} = -\sum_{m=0}^{N_e}\sum_{r=0}^{m}\Big[\tfrac{(-1/4)^m}{2m+1}\tfrac{(-1)^r}{2}\binom{2m+1}{r} \cdot\Big(\sin\big((2m-2r)\theta\big)+\sin\big((2m-2r+2)\theta\big)\Big)\Big] \quad , \tag{4.13b}$$

where N_o and N_e indicate, respectively, the number of odd and even terms of the sine series kept in the expansion. The more terms the better the approximation to the function. It is interesting to observe that the approximation of the first logarithmic term, L_1, associated with the angle bent by the flap, comprises odd terms of the sine series only, whereas the approximation of the second logarithmic term, L_2, related to the bending angular velocity, contains solely even terms.

An illustrative example of the accuracy achieved if the logarithmic functions from Eq. (4.6) are approximated by sums of sines to the power of one, as defined in Eq. (4.13), is given in Fig. 4.2. The presence of a logarithmic component in the vortex sheet strength gives rise to a pronounced spike around the hinge, going from zero at the leading edge to infinity at the hinge location, and back to zero at the trailing edge. The effect is thus centred around the hinge, and it is directly proportional to the flap amplitude and rate of deflection. An approximation of the function by a sine series, no matter how many terms are kept, accurately tracks the target curve everywhere over the aerofoil except in the vicinity of the hinge, where it removes the singularity to produce a bump. The fewer terms the smoother the bump, although the higher the deviation from the original value.

Uncoupled effects

Upon substitution of the relations from Table 4.1 and the approximations to the logarithmic terms from Eq. (4.13) in the expressions of the non-circulatory vortex sheet strength (Eqs. (4.2) to (4.5)), to have them all written in terms of the chordwise transformation variable θ in consistency with UTAT, and recalling that logarithmic terms have been approximated for a flap whose chord length is half that of the aerofoil, $\theta_f = \frac{\pi}{2}$, the effects of plunge, pitch and flap motions can be isolated for this specific geometry. Individual contributions to the non-circulatory vortex sheet strength are therefore broken down as:

1. Plunge rate — $\dot{h}$

$$\gamma_{n_h} = \dot{h}(t)\left[2c\cot\theta\right] \quad . \tag{4.14}$$

2. Pitch angle — α

$$\gamma_{n_\alpha} = \alpha(t)\left[2U\cot\theta\right] \quad . \tag{4.15}$$

3. Pitch rate — $\dot{\alpha}$

$$\gamma_{n_{\dot{\alpha}}} = \dot{\alpha}(t)\left[2c\left(\frac{1}{2} - \frac{c_{pvt}}{c}\right)\cot\theta - \frac{c}{2}\csc\theta + c\sin\theta\right] \quad . \tag{4.16}$$

4. Flap angle — β

$$\begin{aligned}\gamma_{n_\beta} = \;& \beta(t)\Big[\,U\cot\theta - \tfrac{2U}{\pi}\csc\theta \\ & +\tfrac{2U}{\pi}\sum_{m=0}^{N}\sum_{r=0}^{m}\tfrac{(-1)^{m+r}}{2^{2m}(2m+1)}\tbinom{2m+1}{r}\sin\left(2(m-r+\tfrac{1}{2})\theta\right)\,\Big] \quad .\end{aligned} \tag{4.17}$$

5. Flap rate — $\dot{\beta}$

$$\begin{aligned}\gamma_{n_{\dot{\beta}}} = \; & \dot{\beta}(t)\Big[\, \tfrac{c}{\pi}\cot\theta - \tfrac{c}{4}\csc\theta + \tfrac{c}{2}\sin\theta \\ & -\tfrac{c}{\pi}\sum_{m=0}^{N}\sum_{r=0}^{m}\tfrac{(-1)^{m+r}}{2^{2m+1}(2m+1)}\tbinom{2m+1}{r}\Big(\sin\big(2(m-r)\theta\big)+\sin\big(2(m-r+1)\theta\big)\Big)\Big] \quad . \end{aligned} \tag{4.18}$$

Beyond the interest in having uncoupled the effect of kinematics parameters, upon grouping terms with the same trigonometric function in both circulatory and non-circulatory vortex sheet strengths, and comparing them with the bound vortex sheet strength from unsteady thin-aerofoil theory, individual contributions to all Fourier coefficients are obtained in §4.3.

4.2.3 Circulatory vortex sheet strength – motion

The circulatory component of the vortex sheet strength is attributed to flow field vorticity which the moving or deforming body sheds itself. According to the flow partitioning previously described, in order to form the quasi-steady vortex sheet strength a pure circulatory flow (it must induce zero flow through the surface) needs to be produced, its net circulation being determined so as the steady Kutta condition is enforced. Such circulatory flow is defined in Epps and Roesler (2018) by the following vorticity distribution:

$$\gamma_{c0}(\tilde{x},t) = \frac{\Gamma_0(t)}{\pi b}\frac{1}{\sqrt{1-\tilde{x}^2}} \quad , \tag{4.19}$$

where the required circulation is $\Gamma_0(t) = 2\pi b W_0\, e^{i\omega t}$, with W_0 being the complex amplitude of the motion, expressed as:

$$W_0 = i\omega h_0 + U\alpha_0 + i\omega b\left(\frac{1}{2}-a\right)\alpha_0 + \frac{1}{\pi}T_{10}U\beta_0 + i\omega\frac{1}{2\pi}bT_{11}\beta_0 \quad . \tag{4.20}$$

Coefficients T_{10} and T_{11} in the above expression are provided by Theodorsen (1935) as $T_{10} = \sqrt{1-f^2} + \arccos(f)$ and $T_{11} = (2-f)\sqrt{1-f^2} + (1-2f)\arccos(f)$.

Uncoupled effects

By substituting in Eqs. (4.19) and (4.20) the variables given in Table 4.1, individual contributions to the circulatory vortex sheet strength due to motion are derived:

1. Plunge rate — $\dot{h}$

$$\gamma_{c0_h} = \dot{h}(t)\left[2c\csc\theta\right] \quad . \tag{4.21}$$

2. Pitch angle — α

$$\gamma_{c0_\alpha} = \alpha(t)\left[2U\csc\theta\right] \quad . \tag{4.22}$$

3. Pitch rate — $\dot{\alpha}$

$$\gamma_{c0_{\dot{\alpha}}} = \dot{\alpha}(t)\left[2c\left(\frac{3}{4} - \frac{c_{pvt}}{c}\right)\csc\theta\right] \quad . \tag{4.23}$$

4. Flap angle — β

$$\gamma_{c0_\beta} = \beta(t)\Big[2U\left(\frac{1}{2} + \frac{1}{\pi}\right)\csc\theta\Big] \quad . \tag{4.24}$$

5. Flap rate — $\dot{\beta}$

$$\gamma_{c0_{\dot{\beta}}} = \dot{\beta}(t)\Big[c\left(\frac{1}{4} + \frac{1}{\pi}\right)\csc\theta\Big] \quad . \tag{4.25}$$

4.2.4 Circulatory vortex sheet strength – wake

The wake-induced vortex sheet strength is written in Epps and Roesler (2018) as:

$$\gamma_w(\theta,t) = -ik\frac{\Gamma_0}{\pi b}S(k)\left[Q_0(k)\frac{1-\cos\theta}{\sin\theta} + 2\sum_{n=1}^{\infty}Q_n(k)\sin(n\theta)\right]e^{i\omega t} \quad , \tag{4.26}$$

where $S(k)$ is the Sears function and $Q_n(k)$ are the wake coefficients. The first two can be analytically evaluated as $Q_0(k) = K_0(ik)$ and $Q_1(k) = K_1(ik) - \frac{1}{ik}\,e^{-ik}$, being $K_n(ik)$ modified Bessel functions. The remainder of wake coefficients have to be calculated numerically, and up to 3000 terms might be necessary to reach convergence to a smooth distribution of vorticity. The method to calculate these coefficients is detailed in Epps and Roesler (2018).

Uncoupled effects

Proceeding in a similar manner as for the previous case, expressions for the individual effects on the circulatory vortex sheet strength induced by the wake are here derived:

1. Plunge rate — $\dot{h}$

$$\begin{aligned} \gamma_{w_h} = \; & -\dot{h}(t)\Big[\, 2\,c\,i\,k\,S(k)\,Q_0(k)(\csc\theta + \cot\theta) \\ & +4\,c\,i\,k\,S(k)\,Q_n(k)\sin(n\theta)\,\Big] \quad . \end{aligned} \tag{4.27}$$

2. Pitch angle — α

$$\begin{aligned} \gamma_{w_\alpha} = \; & -\alpha(t)\Big[\, 2\,U\,i\,k\,S(k)\,Q_0(k)(\csc\theta + \cot\theta) \\ & +4\,U\,i\,k\,S(k)\,Q_n(k)\sin(n\theta)\,\Big] \quad . \end{aligned} \tag{4.28}$$

3. Pitch rate — $\dot{\alpha}$

$$\begin{aligned} \gamma_{w_{\dot\alpha}} = \; & -\dot{\alpha}(t)\Big[\, 2\,c\left(\tfrac{3}{4} - \tfrac{c_{pvt}}{c}\right) i\,k\,S(k)\,Q_0(k)(\csc\theta + \cot\theta) \\ & +4\,c\left(\tfrac{3}{4} - \tfrac{c_{pvt}}{c}\right) i\,k\,S(k)\,Q_n(k)\sin(n\theta)\,\Big] \quad . \end{aligned} \tag{4.29}$$

4. Flap angle — β

$$\begin{aligned} \gamma_{w_\beta} = \; & -\beta(t)\Big[\, 2\,U\left(\tfrac{1}{2} + \tfrac{1}{\pi}\right) i\,k\,S(k)\,Q_0(k)(\csc\theta + \cot\theta) \\ & +4\,U\left(\tfrac{1}{2} + \tfrac{1}{\pi}\right) i\,k\,S(k)\,Q_n(k)\sin(n\theta)\,\Big] \quad . \end{aligned} \tag{4.30}$$

5. Flap rate — $\dot{\beta}$

$$\begin{aligned} \gamma_{w_{\dot\beta}} = \; & -\dot{\beta}(t)\Big[\, c\left(\tfrac{1}{4} + \tfrac{1}{\pi}\right) i\,k\,S(k)\,Q_0(k)(\csc\theta + \cot\theta) \\ & +2\,c\left(\tfrac{1}{4} + \tfrac{1}{\pi}\right) i\,k\,S(k)\,Q_n(k)\sin(n\theta)\,\Big] \quad . \end{aligned} \tag{4.31}$$

Table 4.2: Components of quasi-steady vortex sheet strength, $\gamma_0(\theta,t)$.

	$\cot(\frac{\theta}{2})$	$\sin\theta$	$\sin(n\theta)$ for $n \geq 2$
$\dot{h}(t)$	$2c$	-	-
$\alpha(t)$	$2U$	-	-
$\dot{\alpha}(t)$	$2c\,(\frac{1}{2} - \frac{c_{pvt}}{c})$	c	-
$\beta(t)$	U	$\frac{2U}{\pi}\sum\limits_{m}^{N}\frac{1}{2^{2m}(2m+1)}\binom{2m+1}{m}$	Eq. (4.36a)
$\dot{\beta}(t)$	$\frac{c}{\pi}$	$\frac{c}{2}$	Eq. (4.36b)

Table 4.3: Components of wake-induced vortex sheet strength, $\gamma_w(\theta,t)$.

	$\cot(\frac{\theta}{2})$	$\sin(n\theta)$ for $n \geq 1$
$\dot{h}(t)$	$-2\,c\,i\,k\,S(k)\,Q_0(k)$	$-4\,c\,i\,k\,S(k)\,Q_n(k)$
$\alpha(t)$	$-2\,U\,i\,k\,S(k)\,Q_0(k)$	$-4\,U\,i\,k\,S(k)\,Q_n(k)$
$\dot{\alpha}(t)$	$-2\,c\,(\frac{3}{4} - \frac{c_{pvt}}{c})\,i\,k\,S(k)\,Q_0(k)$	$-4\,c\,(\frac{3}{4} - \frac{c_{pvt}}{c})\,i\,k\,S(k)\,Q_n(k)$
$\beta(t)$	$-2\,U\,(\frac{1}{2} + \frac{1}{\pi})\,i\,k\,S(k)\,Q_0(k)$	$-4\,U\,(\frac{1}{2} + \frac{1}{\pi})\,i\,k\,S(k)\,Q_n(k)$
$\dot{\beta}(t)$	$-c\,(\frac{1}{4} + \frac{1}{\pi})\,i\,k\,S(k)\,Q_0(k)$	$-2\,c\,(\frac{1}{4} + \frac{1}{\pi})\,i\,k\,S(k)\,Q_n(k)$

At this point, all components of the vorticity distribution over an aerofoil are expressed in terms of the transformation variable from UTAT, θ. Combining the non-circulatory and the circulatory contributions due to motion, listed in Eqs. (4.14) to (4.18) and Eqs. (4.21) to (4.25), the quasi-steady vortex sheet strength is defined: $\gamma_0 = \gamma_n + \gamma_{c0}$. All terms here are functions of either $\cot(\frac{\theta}{2})$ or $\sin(n\theta)$, and the same goes for the wake-induced vortex sheet strength, γ_w (note that $\cot(\frac{\theta}{2}) = \csc\theta + \cot\theta$). Direct comparison with the bound vortex sheet strength from unsteady thin-aerofoil theory is now possible. A summary in a matrix-like form is given in Tables 4.2 and 4.3, where each element is associated to a certain time-dependant kinematics parameter and trigonometric function of the transformation variable.

4.3 Fourier coefficients

Having obtained expressions for the bound vortex sheet strength it is possible to derive simple forms of the Fourier coefficients, needed to compute the unsteady pressure distribution over the aerofoil-flap configuration, and to determine the dynamics of the stagnation point. It is the aim of the present section to derived these expressions, for all Fourier coefficients, in terms of only the amplitude and reduced frequency of motion, which are the inputs of the low-order model.

Recalling from Eq. (4.1) that complex harmonic functions are defined as the amplitude of the variable in question multiplied by $e^{i\omega t}$, time derivatives are obtained multiplying by $\frac{i2Uk}{c}$. Applying this factor to the corresponding terms in Tables 4.2 and 4.3, dividing by $2U$ for direct comparison with the bound vorticity in UTAT, and taking the real part of the resulting expressions, the contribution of each kinematics parameter to each Fourier coefficient is obtained in the form of a sinusoid. The temporal evolution of any Fourier coefficient is therefore defined by a sinusoidal wave whose amplitude comprises the effects of plunge rate, pitch angle, pitch rate, flap deflection angle and flap deflection rate:

$$A_n(t) = \left(A_{n,h} + A_{n,\alpha} + A_{n,\dot{\alpha}} + A_{n,\beta} + A_{n,\dot{\beta}}\right) e^{i\omega t} \quad . \tag{4.32}$$

4.3.1 A_0 and A_1 coefficients

The first two Fourier coefficients, A_0 and A_1, play a fundamental role in potential flow theory since they are necessary to compute both the bound circulation in Eq. (3.26) and the non-circulatory component of unsteady loads in Eq. (3.37). The importance of the *zero*-th coefficient is further manifested in Chapter 5 through its use in predicting and modelling leading-edge flow separation. These reasons justify the special consideration of A_0 and A_1 in this section.

The amplitude of individual effects in Eq. (4.32) is given in Table 4.4 for the A_0 coefficient, and in Table 4.5 for the A_1 coefficient. Note that all kinematics

Table 4.4: Amplitude of individual effects in A_0 Fourier coefficient.

$A_{0,h}$	$h_0\,\Re\,(2\,i\,k + 2\,k^2\,S(k)\,Q_0(k))$
$A_{0,\alpha}$	$\alpha_0\,\Re\,(1 - i\,k\,S(k)\,Q_0(k))$
$A_{0,\dot{\alpha}}$	$\alpha_0\,\Re\big(2\,i\,k\,(\frac{1}{2} - \frac{c_{pvt}}{c}) + 2\,(\frac{3}{4} - \frac{c_{pvt}}{c})\,k^2\,S(k)\,Q_0(k)\big)$
$A_{0,\beta}$	$\beta_0\,\Re\big(\frac{1}{2} - (\frac{1}{2} + \frac{1}{\pi})\,i\,k\,S(k)\,Q_0(k)\big)$
$A_{0,\dot{\beta}}$	$\beta_0\,\Re\big(\frac{1}{\pi}\,i\,k + (\frac{1}{4} + \frac{1}{\pi})\,k^2\,S(k)\,Q_0(k)\big)$

Table 4.5: Amplitude of individual effects in A_1 Fourier coefficient.

$A_{1,h}$	$h_0\,\Re\,(4\,k^2\,S(k)\,Q_1(k))$
$A_{1,\alpha}$	$\alpha_0\,\Re\,(-2\,i\,k\,S(k)\,Q_1(k))$
$A_{1,\dot{\alpha}}$	$\alpha_0\,\Re\big(i\,k + 4\,(\frac{3}{4} - \frac{c_{pvt}}{c})\,k^2\,S(k)\,Q_1(k)\big)$
$A_{1,\beta}$	$\beta_0\,\Re\Bigg(\frac{1}{\pi}\sum_{m}^{N}\frac{1}{2^{2m}(2m+1)}\binom{2m+1}{m} - 2\,(\frac{1}{2} + \frac{1}{\pi})\,i\,k\,S(k)\,Q_1(k)\Bigg)$
$A_{1,\dot{\beta}}$	$\beta_0\,\Re\big(\frac{1}{2}\,i\,k + 2\,(\frac{1}{4} + \frac{1}{\pi})\,k^2\,S(k)\,Q_1(k)\big)$

parameters contribute a quasi-steady and a wake-induced term to the total amplitude of A_0 (expressed the last one as a complex function of the reduced frequency, k). Whereas for the amplitude of A_1 only the pitch rate, flap angle and flap rate effects have a quasi-steady component.

Complex functions of the reduced frequency

Following the main thesis theme of morphing through temporal camber variations, a pure flap motion has been considered in this chapter for the analysis of Fourier coefficients. Their expressions, Eq. (4.32), evolve in time as sinusoidal waves of an amplitude determined by solely flap-related terms, which for A_0 and A_1 become:

$$A_0(t) = (A_{0,\beta} + A_{0,\dot{\beta}})\,e^{i\omega t} \quad , \tag{4.33a}$$

$$A_1(t) = (A_{1,\beta} + A_{1,\dot{\beta}})\,e^{i\omega t} \quad , \tag{4.33b}$$

with $A_{0,\beta}$, $A_{0,\dot{\beta}}$, $A_{1,\beta}$ and $A_{1,\dot{\beta}}$ provided in Tables 4.4 and 4.5.

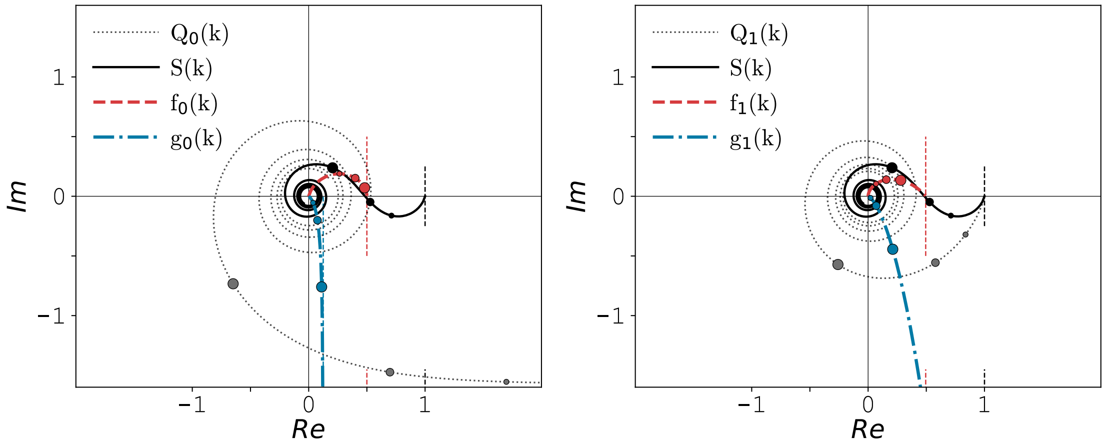

(a) (b)

Figure 4.3: Representation in the complex plane of functions used to calculate Fourier coefficients A_0 (a) and A_1 (b): wake coefficients $Q(k)$ (⋯⋯), Sears function $S(k)$ (——), $f(k)$ (- - - -) and $g(k)$ (- - - -). Direction of increasing reduced frequency is indicated for each curve by filled circles of growing size ($k_\beta = 0.2$, $k_\beta = 0.5$, $k_\beta = \pi/2$).

To get a better understanding of the effect the reduced frequency, k, has on the total amplitude of A_0 and A_1, a complex function is defined for each of these four coefficients by grouping their terms that depend on said parameter:

$$\left.\begin{array}{llcll} f_0(k) = i\,k\,S(k)\,Q_0(k) & \text{for } A_{0,\beta} & , & g_0(k) = k^2\,S(k)\,Q_0(k) & \text{for } A_{0,\dot{\beta}} \\ f_1(k) = i\,k\,S(k)\,Q_1(k) & \text{for } A_{1,\beta} & , & g_1(k) = k^2\,S(k)\,Q_1(k) & \text{for } A_{1,\dot{\beta}} \end{array}\right\} \quad , \tag{4.34}$$

where the wake coefficients $Q_0(k)$ and $Q_1(k)$ have been introduced in §4.2.4.

These two pair of functions are plotted in the complex plane, along with the Sears function and the wake coefficient used in their formulation, to examine their tendency as the reduced frequency increases. Functions related to A_0 are represented in Fig. 4.3(a), and those pertaining to A_1 in Fig. 4.3(b). With increasing reduced frequency, in the direction of the curve in which filled circles grow in size, the real part of all but one of the newly defined complex functions goes from zero when $k = 0$ to an asymptotic value when $k \to \infty$. These limiting values are $\frac{1}{2}$ for $f_0(k)$ and $f_1(k)$, and $\frac{1}{8}$ for $g_0(k)$. They will impose a constraint on the growth of the term they contribute to the amplitude of the respective Fourier coefficient. Since all terms in A_0

are bounded, the amplitude of this coefficient reaches a constant value after some k. The only function with an unbounded real part, $g_1(k)$, contributes to the amplitude of A_1. Because this term will grow indefinitely with the reduced frequency, so will the total amplitude of A_1, even when the remaining terms present a limit. It will be easier to visualise all this in the next subsection, where a scale factor is introduced that indicates the behaviour of Fourier coefficient with the reduced frequency.

Scale factors

Observing how terms are defined in Tables 4.4 to 4.7, the amount contributed by each kinematics parameter to the total amplitude of a Fourier coefficient is expressed as a constant multiplied by the real part of a complex function. This constant indicates the amplitude of the corresponding motion (plunge, pitch, flap deflection). The real part of the function can be thought of as a factor which scales that magnitude depending on the reduced frequency of the motion. It serves to indicate how much will it contribute to the amplitude of the Fourier coefficient when the reduced frequency is modified. Different subfactors can be introduced for each vorticity component within a specific motion effect contributing to a certain Fourier coefficient, this is, every term of every row of every table (e.g., non-circulatory component of pitch rate on A_0, wake-induced effect due to flap deflection on A_2, and so on). Since pure flap kinematics have been considered for analysis in this section, the scale factor for the flap motion, $\mathcal{S}_\beta$, multiplied by the complex amplitude of flap deflection, β_0, provides the total amount contributed by the flap motion to the desired Fourier coefficient: $A_{n,\beta} = \mathcal{S}_\beta \beta_0$.

As mentioned, each factor can be broken down into several subfactors. For example, to compute A_0 for this case of an aerofoil undergoing exclusively flap deflections, according to Table 4.4 there will be 4 contributing terms (those inside the big parenthesis in the last two rows): the quasi-steady part of the vorticity, and the part associated with the wake, for both individual effects, the flap angle and the flap rate. But the function defining the quasi-steady component on the flap rate effect has no real part. Thus, the scale factor for the flap motion is decomposed as:

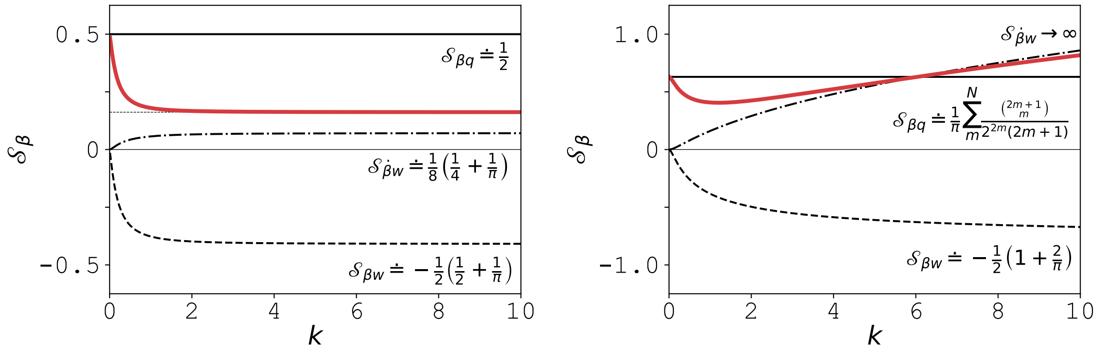

(a) (b)

Figure 4.4: Scale factors for flap motion as a function of the reduced frequency, for A_0 (a) and A_1 (b) Fourier coefficients: quasi-steady part of vorticity due to flap deflection amplitude $\mathcal{S}_{\beta q}$ (—), wake-induced part owing to flap deflection amplitude $\mathcal{S}_{\beta w}$ (----), wake-induced part from flap deflection rate $\mathcal{S}_{\dot\beta w}$ (-·-·), and combined effect (—). Asymptotic values are shown to the right of each curve.

$$\mathcal{S}_\beta = \mathcal{S}_{\beta q} + \mathcal{S}_{\beta w} + \mathcal{S}_{\dot\beta w} \quad , \tag{4.35}$$

where $\mathcal{S}_{\beta q}$ is the subfactor defined for the quasi-steady part of the vorticity due to the flap deflection amplitude; $\mathcal{S}_{\beta w}$ similar for the part of the vorticity associated with the wake; and $\mathcal{S}_{\dot\beta w}$ a subfactor to compute the wake-induced part of the vorticity owing to the rate of flap deflection.

Insight into the behaviour of Fourier coefficients with the reduced frequency can be gained by understanding the effect this parameter has on each subfactor. The evolution with k of all terms in Eq. (4.35) is exhibited in Fig. 4.4. The first subfactor, $\mathcal{S}_{\beta q}$, does not depend on the reduced frequency, so its contribution will be a constant value. Subfactors $\mathcal{S}_{\beta w}$ and $\mathcal{S}_{\dot\beta w}$ are proportional to the complex functions $f(k)$ and $g(k)$ introduced in Eq. (4.34), so they will behave alike with the reduced frequency. Accordingly, for $k = 0$ they will be null, and for $k \to \infty$ they will converge to the asymptotic values before mentioned multiplied by certain constants, as shown to the right of each curve (see Tables 4.4 and 4.5). Finally, the total scale factor for the flap motion, $\mathcal{S}_\beta$, sum of the previous three (red line in the graphs), will have at $k = 0$ the same value as the quasi-steady subfactor of the corresponding Fourier

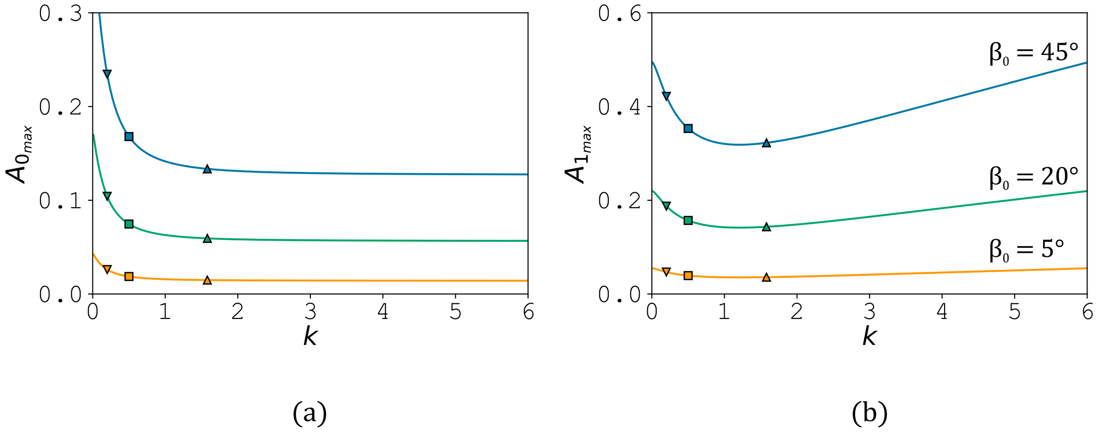

Figure 4.5: Maximum amplitude of A_0 (a) and A_1 (b) Fourier coefficients as a function of the reduced frequency, for flap deflection amplitudes $\beta_0 = 5°$ (yellow), $\beta_0 = 20°$ (green) and $\beta_0 = 45°$ (blue). Markers indicate reduced frequencies selected for validation.

coefficient. For $k \to \infty$ the trend will differ between coefficients: for A_0, where all subfactors are bounded, it will evolve towards a constant value which is the sum of the three asymptotic values, whereas for A_1 it will scale as $\mathcal{O}(k^2)$.

Parameter space

The two main parameters that quantitatively characterise aerofoil kinematics are the amplitude and the rate of motion. Their effect on A_0 Fourier coefficient is discussed in Fig. 4.5(a), and on A_1 coefficient in Fig. 4.5(b). This can be easily deduced by looking at Tables 4.4 and 4.5. The effect of the reduced frequency has been analysed in the previous subsection. The tendency of Fourier coefficients with variations of this parameter is clear by observing the behaviour of scale subfactors associated with the kinematics in question (harmonic flap deflections here). As explained, the maximum value or amplitude of the Fourier coefficient is the result of multiplying the scale factor by the kinematics amplitude. Thus, the curve representing maximum values of A_0 and A_1 will have the shape of the corresponding red curve in Fig. 4.4 scaled by the amplitude of the motion (hence the name of the factors). The trend is shown for three different amplitudes of flap deflection: $\beta_0 = 5°$, $\beta_0 = 20°$, $\beta_0 = 45°$. As for the amplitude effect, Fourier coefficients are directly proportional to this magnitude. It is observed in Fig. 4.5 how larger values of flap deflection shift the curve of each coefficient upwards while the general trend is preserved.

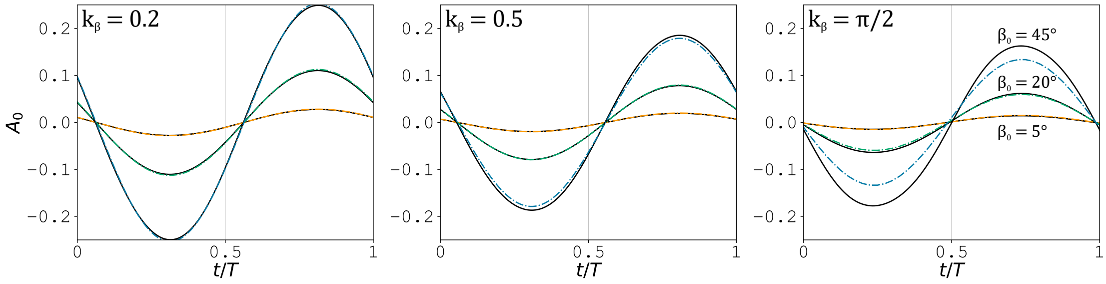

(a) (b) (c)

Figure 4.6: Temporal evolution of A_0 Fourier coefficient for one cycle of harmonic flap deflection with small, medium and large amplitude (yellow, green and blue respectively), with: (a) low, (b) medium and (c) high reduced frequency. Results are from the analytical solution (-·-·) and the discrete-vortex model (——).

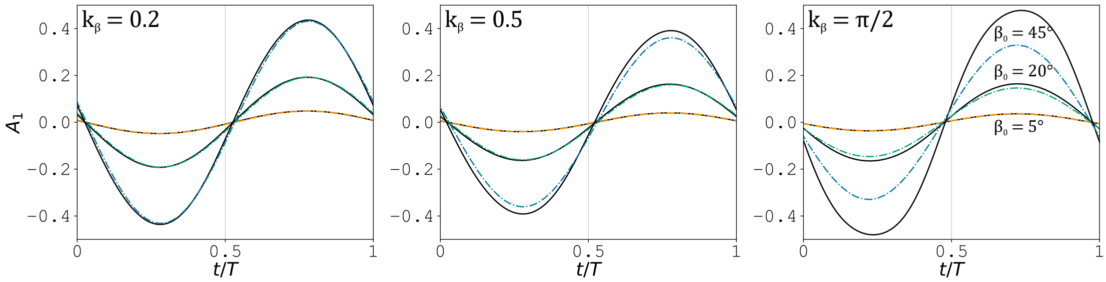

(a) (b) (c)

Figure 4.7: Temporal evolution of A_1 Fourier coefficient for one cycle of harmonic flap deflection with small, medium and large amplitude (yellow, green and blue respectively), with: (a) low, (b) medium and (c) high reduced frequency. Results are from the analytical solution (-·-·) and the discrete-vortex model (——).

Comparison with numerical results

Theoretical expressions of the Fourier coefficients derived in this chapter serve as a benchmark for validation of numerical codes. Comparison between these analytic expressions and simulations performed with the discrete-vortex model developed in Chapter 3 is made in Fig. 4.6 for A_0 Fourier coefficient, and in Fig. 4.7 for A_1 Fourier coefficient. The parameter space chosen for comparison encompasses a range of values, for the deflection amplitude and the reduced frequency, wide enough to cover various cases of engineering interest, such as those studied in §3.4. Nine different cases of harmonic trailing-edge flap deflections are therefore selected, which comprise all possible combinations of deflection amplitudes $\beta_0 = 5°$, $\beta_0 = 20°$ and $\beta_0 = 45°$,

Table 4.6: Amplitude of individual effects in A_n Fourier coefficients (n = 3,5,7...).

$A_{n,h}$	$h_0\, \Re\,(4\,k^2\, S(k)\, Q_n(k))$
$A_{n,\alpha}$	$\alpha_0\, \Re\,(-2\,i\,k\, S(k)\, Q_n(k))$
$A_{n,\dot{\alpha}}$	$\alpha_0\, \Re\big(4\,(\frac{3}{4} - \frac{c_{pvt}}{c})\, k^2\, S(k)\, Q_n(k)\big)$
$A_{n,\beta}$	$\beta_0\, \Re\big(\frac{T_1}{2U} - 2\,(\frac{1}{2} + \frac{1}{\pi})\, i\,k\, S(k)\, Q_n(k)\big)$
$A_{n,\dot{\beta}}$	$\beta_0\, \Re\big(2\,(\frac{1}{4} + \frac{1}{\pi})\, k^2\, S(k)\, Q_n(k)\big)$

Table 4.7: Amplitude of individual effects in A_n Fourier coefficients (n = 2,4,6...).

$A_{n,h}$	$h_0\, \Re\,(4\,k^2\, S(k)\, Q_n(k))$
$A_{n,\alpha}$	$\alpha_0\, \Re\,(-2\,i\,k\, S(k)\, Q_n(k))$
$A_{n,\dot{\alpha}}$	$\alpha_0\, \Re\big(4\,(\frac{3}{4} - \frac{c_{pvt}}{c})\, k^2\, S(k)\, Q_n(k)\big)$
$A_{n,\beta}$	$\beta_0\, \Re\big(-2\,(\frac{1}{2} + \frac{1}{\pi})\, i\,k\, S(k)\, Q_n(k)\big)$
$A_{n,\dot{\beta}}$	$\beta_0\, \Re\big(\frac{T_2}{c}\, i\,k + 2\,(\frac{1}{4} + \frac{1}{\pi})\, k^2\, S(k)\, Q_n(k)\big)$

with reduced frequencies $k_\beta = 0.2$, $k_\beta = 0.5$ and $k_\beta = \frac{\pi}{2}$. Numerical parameters used for the LOM are those stated in §3.2.2, and results presented are for one cycle of motion. At one edge of the spectrum, with the smallest values of both amplitude and reduced frequency, theoretical and numerical predictions perfectly match. Upon increasing the value of any of the parameters, the agreement is preserved in all cases except at the opposite edge of the spectrum. For this case, with the highest amplitude and reduced frequency, the maximum value predicted theoretically is lower than the one provided by the low-order model. It is not surprising, since the derivation of Fourier coefficients presented in this chapter is built upon the classical theory of Theodorsen, which is only valid for small amplitudes. Finally, note that the maximum value of each curve corresponds with a marker from Fig. 4.5.

4.3.2 A_n coefficients ($n \geq 2$)

The logarithmic terms that appear in the expression for the vortex sheet strength were approximated by sine series in Eq. (4.13). Independent contributions to A_n Fourier coefficients with $n \geq 2$ can be extracted upon using the following transformation variables to get rid off the second summation: $r = m - \frac{n-1}{2}$ for

Eq. (4.13*a*), and $r = m - \frac{n}{2}$ and $r = m - \frac{n-2}{2}$ for Eq. (4.13*b*). The missing terms in Table 4.2, which will be defined as T_1 and T_2, are then:

$$T_1 = \frac{2U}{\pi} \sum_{m=\frac{n-1}{2}}^{N_o} \frac{(-1)^{\frac{n-1}{2}}}{2^{2m}(2m+1)} \binom{2m+1}{m - \frac{n-1}{2}} \quad \text{with} \quad n = 3, 5, 7, \ldots \quad , \tag{4.36a}$$

$$T_2 = -\frac{c}{\pi} \sum_{m=\frac{n-2}{2}}^{N_e} \frac{(-1)^{\frac{n}{2}}}{2^{2m+1}(2m+1)} \left[\binom{2m+1}{m - \frac{n}{2}} - \binom{2m+1}{m - \frac{n-2}{2}} \right] \quad \text{with} \quad n = 2, 4, 6, \ldots \quad , \tag{4.36b}$$

where the last term of the summation is the binomial coefficient.

Following the method used for A_0 and A_1 Fourier coefficients, the amplitude of individual effects in Eq. (4.32) can now be obtained elegantly, and is given in Table 4.6 for odd-index A_n coefficients, and in Table 4.7 for even-index A_n coefficients. Note that the quasi-steady vorticity component contributing to the amplitude of A_n coefficients with $n \geq 2$ depends only on the shape of the camber line (last column in Table 4.2). Thus, only flap kinematics (flap angle and flap rate) can have both, the quasi-steady and the wake-induced contributions.

Comparison with numerical results

An equivalent full analysis to the one performed in §4.3.1 is theoretically possible for A_n Fourier coefficients with $n \geq 2$. However, no analytical closed-forms can be derived for wake coefficients $Q_n(k)$, and a numerical approach has to be considered (see §4.2.4). This means that a large number of computations would be required to properly study the dependency on the reduced frequency, which makes the effort worthless. Instead, only for a few cases, the same nine cases as before, the temporal evolution of A_2 and A_3 Fourier coefficients are compared against numerical predictions from the discrete-vortex model. Results for one cycle of motion are presented for A_2 in Fig. 4.8, and for A_3 in Fig. 4.9. Because the derivation of the analytic expressions is based on Theodorsen's theory, where small amplitude and planar wake assumptions are made, results are expected to be less accurate for large-amplitude deflections. For these cases, the numerical curve distorts and

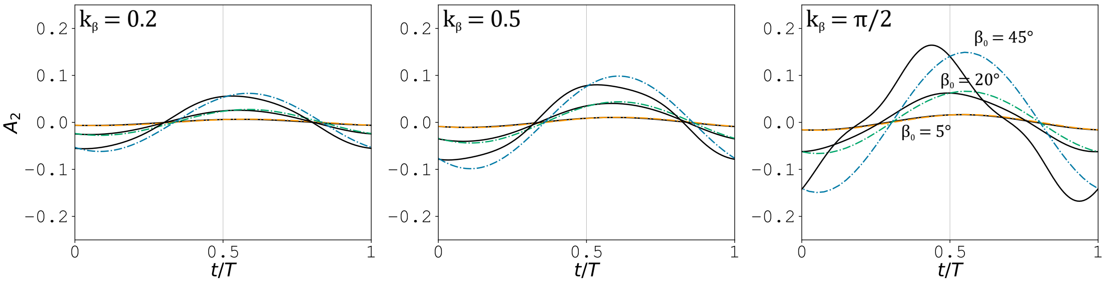

(a) (b) (c)

Figure 4.8: Temporal evolution of A_2 Fourier coefficient for one cycle of harmonic flap deflection with small, medium and large amplitude (yellow, green and blue respectively), with: (a) low, (b) medium and (c) high reduced frequency. Results are from the analytical solution (- - - -) and the discrete-vortex model (——).

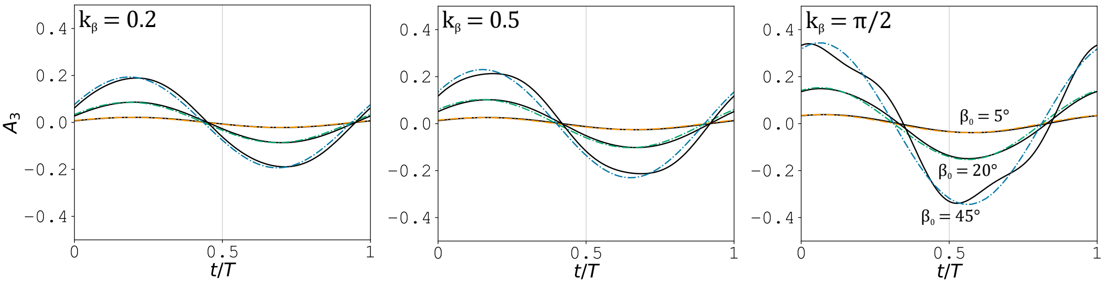

(a) (b) (c)

Figure 4.9: Temporal evolution of A_3 Fourier coefficient for one cycle of harmonic flap deflection with small, medium and large amplitude (yellow, green and blue respectively), with: (a) low, (b) medium and (c) high reduced frequency. Results are from the analytical solution (- - - -) and the discrete-vortex model (——).

shows non-linearity (as it happened for the lift coefficient in Fig. 3.17), whereas the theoretical prediction does not. Furthermore, it was shown in §3.4.5 that flow separation occurs at the leading edge of the aerofoil in that case. With the exception of said case, analytical and numerical predictions compare very similar for all other combinations of amplitude and reduced frequency studied.

4.4 Summary

The main motivation of this chapter has been to contribute simple analytical forms of all bound vorticity Fourier coefficients, with the effect of motion-defining parameters uncoupled, for the fundamental aerodynamic problem of an oscillating plate-flap configuration. Uncoupling the different contributions facilitates a better understanding of their relation to the Fourier coefficients, and by extension to the unsteady pressure distribution and stagnation point location.

To achieve this goal, available expressions of the vortex sheet strength for this problem have been adapted to the frame of reference used in unsteady thin-aerofoil theory. This allowed the coefficients sought to be obtained by comparing expressions for the bound vortex sheet strength. Logarithmic terms in the non-circulatory vortex sheet strength have been approximated using a Fourier expansion for better comparison to the expansion used in unsteady thin-aerofoil theory. This has only been done for the special case of a flap hinged at the mid chord.

All Fourier coefficient expressions have been derived in terms of only the amplitude and reduced frequency of motion. The idea of scale factors has been introduced, with subfactors representing all different components of the vorticity. Insight into the behaviour of Fourier coefficients with the reduced frequency can be gained by analysing the evolution of all subfactors with variations of this parameter.

Contrary to classical analysis that yields closed-form expressions, such as Theodorsen's theory, the present derivation includes series that must be truncated for practical evaluation, in the non-circulatory and wake vorticity terms. The approach for Fourier coefficients with $n \geq 2$ can thus be seen as semi-numerical. Regardless of this, the derived expressions for Fourier coefficients (and accordingly unsteady pressure distribution and stagnation point location) can be used to validate numerical codes.

Comparison has been made between the expressions derived in this chapter and numerical simulations performed with the discrete-vortex model developed in the previous chapter. A pure flap motion with different combinations of amplitude and reduced frequency has been considered for analysis. Theoretical and numerical predictions perfectly match for most cases, with the exception of the case with both largest amplitude and highest frequency. This is as expected, since the small-amplitude assumption of Theodorsen's theory, upon which the derivation is built, imposes a limitation in the accuracy of results for large-amplitude motions.

odd b𝕃urs in sight, disguised keys
(on swimming gaits or Light wingbeats)

aloft they flaunt dextErity,
all gaze enthralled et𝔼rnally.

dear nai𝕍e minds, dare you to dream?
don't waste your Vim, just stop and esteem!

who maSters flight? we'll never twig:
wise flyer𝕊 ride wee flapping wings...

— Àrdachadh Mothachadh

5

LEADING-EDGE VORTEX: MODELLING

5.1 Introduction

VORTEX formation features heavily in this research, and the second half of the dissertation is devoted to its study. Flow separation at the leading edge of a wing or a fin results in an aerodynamic non-linearity. As a consequence of the vorticity produced at this edge a shear layer is formed, that rolls up on itself giving rise to a coherent structure, the well known leading-edge vortex. Fed by the vorticity in this shear layer, the LEV grows in size and strength to the extent that it is able to significantly alter the aerodynamics under study. In a two-dimensional problem the growth rate of the LEV is correlated to the influx of mass through the feeding shear layer, which necessarily depends on the shear layer's thickness. The mass flow rate is itself influenced by the geometry of the leading edge. In particular, it is influenced by the leading-edge radius. Flow separation at the leading edge is a phenomenon attributable entirely to viscosity. Vortex models, although based on inviscid theories, are able to capture the non-linearity associated with the LEV, but require explicit closure conditions. The present chapter explores the performance of some of these models in LEV-dominated flows using different strategies to estimate the vorticity shedding rate from the separation point.

The outline of this chapter is as follows: different approaches for modelling LEV formation are discussed in §5.2, which opens in §5.2.1 bringing back a criterion previously used in discrete-vortex models, and presents in §5.2.2 a novel strategy to determine the vorticity feeding rate. It follows with a thorough comparison in §5.3 of the vortex sheet dynamics resulting from both approaches. After introducing the problem kinematics in §5.3.1, and the CFD model used for validation in 5.3.2, the onset of flow separation is studied in §5.3.3, the vortex growth stage in §5.3.4, and the process of flow reattachment in §5.3.5, to close with the analysis of aerodynamic coefficients in §5.3.6. A particular case from a previous chapter involving flow separation due to flap motion is revised in §5.4 using the new model. Finally, the summary of the chapter is provided in §5.5.

5.2 Leading-edge vortex sheet

Inviscid and incompressible flow assumptions as the basis of the theoretical model may seem inappropriate for studies of low Reynolds number aerodynamics. These regimes are dominated by the effect of viscosity. Viscous fluid phenomena, such as leading-edge separation, can yet be incorporated into low-order models built upon classical aerodynamic theories. This can be accomplished by empirically augmenting potential-flow theory.

Reported evidence that flow separation at the leading edge is closely related to critical events of the flow in this region (Beddoes, 1978; Ekaterinaris & Platzer, 1998; Evans & Mort, 1959; Shih et al., 1995), inspired Ramesh et al. (2014) to seek an inviscid parameter, numerically calculable at every time step of a simulation, that would serve to introduce viscous behaviours in potential flow models, such as the formation of LEVs. For this aim, they hypothesised that a non-dimensional measure of the suction at the leading edge would be correlated to the *zero*-th term in the Fourier expansion of the bound vorticity distribution, A_0 (see Eq. (3.25a)). This way, they introduced the Leading-Edge Suction Parameter (LESP), $\mathcal{L}$:

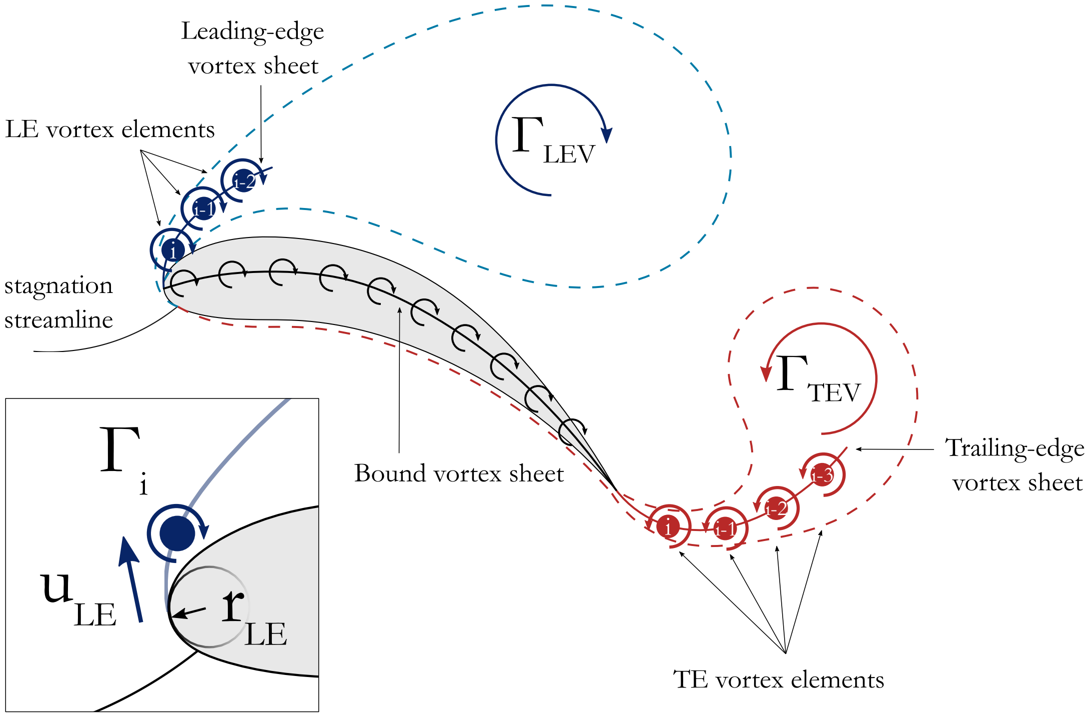

Figure 5.1: Representation of separated shear layers at the leading and trailing edges of an unsteady foil by vortex elements. Inset: parameters involved in the calculation of the strength of leading-edge vortex elements with Eq. (5.6).

$$\mathcal{L}(t) = A_0(t) \quad . \tag{5.1}$$

Success in modelling vortex dynamics has a direct bearing on the vorticity flux through feeding shear layers, here represented by arrays of vortex elements as illustrated in Fig. 5.1. The A_0 term plays a crucial role in this regard. Two different approaches to calculate the strength of vortex elements emerging at the leading edge at every time step of the low-order simulation are discussed next.

5.2.1 Constant-$\mathcal{L}$ model: LDVM

In prior work Ramesh et al. (2014) postulated that leading-edge vortex formation and shedding occurs at a constant value of leading-edge suction, which is indeed the maximum amount that the aerofoil can sustain at that specific Reynolds number of operation. When, due to the motion of the aerofoil or vortex-induced velocities, the instantaneous A_0 from potential theory exceeds that critical value, vorticity is released from the leading edge as discrete vortices. When it falls below the limit, the shedding process terminates. By requiring the theoretical value to equal the empirically determined critical value, an iterative process to fulfil Kelvin's circulation theorem provides the strength of these discrete vortices. Ramesh et al. (2014) developed a discrete-vortex method to simulate leading-edge vortex shedding with this criterion, termed LESP-modulated Discrete-Vortex Method (LDVM). Models based on this idea are gathered in this chapter under the label *constant-$\mathcal{L}$* models, and two different implementations of LDVM are presented herein. Ramesh et al. (2018) further suggested that for a given aerofoil and Reynolds number, the critical value is kinematics-independent as long as no significant trailing-edge flow separation results from the aerofoil's motion.

Several quantitative criteria have been proposed in recent years to trigger leading-edge separation based on local flow signatures. Ramesh et al. (2014) identified the critical value of $\mathcal{L}$ from CFD skin-friction distributions over the aerofoil's upper surface. Initiation of vortex formation is there signalled by the first appearance of a spike in the negative-c_f region reaching a positive value. This time instant is used to obtain the critical $\mathcal{L}$ value from inviscid-LDVM analysis. For this purpose, the attached-flow condition at the leading edge is fulfilled in the low-order simulations by disabling the release of vortex particles from this point. A version of LDVM implemented with this criterion is used in this chapter, and referred to as *criterion P* henceforth.

In a follow-up investigation, Narsipur et al. (2020) expanded the spectrum of parameters used in the study of vortex formation, to notice that the earlier criterion by Ramesh et al. (2014) is limited in applicability to low Reynolds numbers. For the high Reynolds numbers cases analysed in their work, vorticity contours already evinced a clear vortex structure at the time instant corresponding to LEV onset if that criterion is adopted. Alternatively, they proposed the first appearance of an inflexion point within the negative-c_f region as a more reliable signature of LEV onset detection. This criterion proved to work well for all Reynolds numbers studied, and it gives rise to the second version of LDVM contemplated in this chapter, denoted *criterion I* in what follows.

5.2.2 Variable-$\mathcal{L}$ model: SVDVM

The primary intent in §5.2.1 has been to discuss various approaches to estimate the initiation of LEVs. The accuracy of low-order models built on these grounds is however expected to be limited. While the principal physical phenomenon is captured, i.e. the presence of vortex structures in the flow, their temporal evolution is firmly marked by the post-stall behaviour of the leading-edge suction, which governs the rate of circulation fed into the nascent vortex. It must be stressed here that leading-edge suction does not remain fixed at a critical value during vortex formation as suggested by Ramesh et al. (2014), since recent experiments and computation showed that the critical value is reached after the onset of instabilities near the leading edge, preceding flow separation, has already occurred (Deparday & Mulleners, 2019; Narsipur et al., 2020). It will be demonstrated in §5.3 how failing to reproduce this trend affects leading-edge vortex dynamics.

It is the aim of this section to contribute to the resolution of this modelling shortcoming, by presenting an alternative strategy to compute the rate of vorticity shed from the separation point in vortex methods (Martínez et al., 2022). To this end, an expression proposed in the literature to estimate the rate of vorticity transport through a separated shear layer in terms of the velocity at its outside edges (Clements, 1973; Fage & Johansen, 1927; Katz, 1981; Leonard, 1980; Sarpkaya, 1975) is recovered in this work:

$$\frac{d\Gamma_s}{dt} = \frac{1}{2}(V_1^2 - V_2^2) \quad , \tag{5.2}$$

where V_1 and V_2 are the velocities at the outer and inner edges of the shear layer (closer and further to the leading edge respectively), with the outer velocity much greater than the inner velocity, $V_1^2 \gg V_2^2$ (Fage & Johansen, 1927). This way of estimating the rate at which vorticity is released from a separation point was termed the shear velocity method in the literature (Katz, 1981).

Assuming the separation point to be located at the leading edge, a valid supposition for unsteady flow problems with an LEV as the dominant feature, Eq. (5.2) simplifies to the following expression for the leading-edge vorticity feeding rate, $\dot{\Gamma}_{LE}$:

$$\dot{\Gamma}_{LE} = \frac{1}{2} u_{LE}^2 \quad , \tag{5.3}$$

where u_{LE} is the velocity at the leading edge of the aerofoil.

A salient point to make here is that in thin-aerofoil-theory primitive variables become singular at the leading edge: the suction peak, represented by the A_0 term of the bound vorticity distribution, and the velocity are infinite at this location. This poses a hurdle in implementing Eq. (5.3) on reduced order models which are based on UTAT. Ramesh (2020) provided a solution to this issue by applying the principle of matched asymptotic expansions (Van Dyke, 1964). The solution from UTAT (outer solution) is matched with that from unsteady potential flow past a parabola (inner solution) to resolve the singularity. An expression for the velocity at the leading edge is derived that depends on only A_0:

$$u_{LE} = \sqrt{\frac{2}{r_{LE}}} U A_0 \quad , \tag{5.4}$$

with r_{LE} the radius of the aerofoil's leading-edge. For a symmetric NACA aerofoil it is defined as $r_{LE} = 1.1019 t^2$, where t is the maximum thickness of the aerofoil as a fraction of the chord.

A final expression for the growth rate of circulation at the leading edge results after substituting Eq. (5.4) in Eq. (5.3):

$$\dot{\Gamma}_{LE} = \frac{U^2 A_0^2}{r_{LE}} \quad , \tag{5.5}$$

which shows that vorticity feeding rate is proportional to the square of the leading-edge suction parameter and inversely proportional to the leading-edge radius.

The discrete formulation of Eq. (5.5) provides the strength of the i-th vortex particle entering the flow field from the leading edge at the current time step, Γ_i:

$$\boxed{\Gamma_i(t) = \frac{U^2 A_0^2(t)}{r_{LE}}\Delta t} \quad . \tag{5.6}$$

To compute the aerodynamic loads, before the pressure jump is integrated, the contribution of the new vortex particle shed from the leading edge has to be included in the unsteady pressure term, Eq. (3.33), by adding $\frac{\Gamma_i}{\Delta t}$ for every shed particle. The normal force and moment coefficients will then be corrected by adding $\frac{2\Gamma_i c_{eff}}{\Delta t U^2 c}$ and $\frac{\Gamma_i c_{eff}^2}{\Delta t U^2 c^2}$, respectively, at every time step that a vortex particle is shed from the leading edge.

The vortex model constructed following this scheme will be labelled Shear-layer Velocity Discrete-Vortex Model (SVDVM). One of its strengths comes through the unrestricted evolution of $\mathcal{L}$ during the vortex-shedding process. For this reason, it will also be referred to as *variable-*$\mathcal{L}$ model throughout the thesis.

5.3 Leading-edge vortex formation and dynamics

The role of A_0 in the context of vortex sheet dynamics is studied in depth through the primary unsteady flow features: flow separation and vortex formation (covered in §5.3.3), vortex growth (in §5.3.4) and flow reattachment (in §5.3.5).

5.3.1 Kinematics: ramp pitching motion

The canonical ramp manoeuvre suggested by Eldredge et al. (2009) assures the appearance of the previous sequence of events, one in each of the three different segments comprising this movement (up-hold-down). The smoothed pitch motion is given by:

Table 5.1: Parameters defining pitching kinematics.

$\alpha_0[^\circ]$	$\alpha_{max}[^\circ]$	K_α	σ	t_1^*	t_{hold}^*
0	45	0.2	0.9	2	2

$$\alpha(t^*) = \alpha_0 + \frac{K_\alpha}{a} \ln \left[\frac{\cosh\left(a(t^* - t_1^*)\right) \cosh\left(a(t^* - t_4^*)\right)}{\cosh\left(a(t^* - t_2^*)\right) \cosh\left(a(t^* - t_3^*)\right)} \right] \quad , \tag{5.7}$$

where α_0 is the mean pitch angle; $K_\alpha = \frac{\dot{\alpha}c}{2U}$ the reduced pitch rate (this value is determined with the angular velocity, $\dot{\alpha}$, at the midpoint of the ramp-up segment); $a = \pi^2 K_\alpha / (2\alpha_{max}(1-\sigma))$ a parameter to determine the smoothing at the transition points, with larger values of σ (from 0 to 1) producing sharper transitions (Granlund et al., 2013); and α_{max} the pitch amplitude. Time is made non-dimensional by dividing by the convective time, $t^* = \frac{t}{t_c} = \frac{tU}{c}$. The timing of the four transition points is indicated by: t_1^*, start of the pitch-up; $t_2^* = t_1^* + \frac{\alpha_{max}}{2K_\alpha}$ end of the pitch-up; $t_3^* = t_2^* + t_{hold}^*$ start of the pitch-down; $t_4^* = t_3^* + \frac{\alpha_{max}}{2K_\alpha}$ end of the pitch-down. Parameters defining the motion are listed in Table 5.1.

The reasoning for the values imputed is as follows: t_1^* allows enough time for boundary layers to fully develop on the aerofoil before the motions starts; K_α and σ describe a rapid transient manoeuvre, typical for biological and bio-inspired flapping flight; α_{max} and t_{hold}^* guarantee the development of the vortex into a coherent structure, essential for the analysis of the total circulation; α_0 allows the flow to reattach at the leading edge and to track the progress of the reattached region. Additionally, two geometries, NACA 0004 and a NACA 0012 aerofoils, are considered to account for thickness effects, since the shape of an aerofoil (radius at the leading edge) has an impact on the amount of leading-edge suction that it can support (Narsipur, 2022), on the strength of the dynamic-stall vortex, and on the aerodynamic loads (McCroskey, 1982). Finally, the pivot location at the trailing edge offers the possibility of studying vortex events occurring on both sides of the aerofoil during a single manoeuvre. The delayed formation of the typical

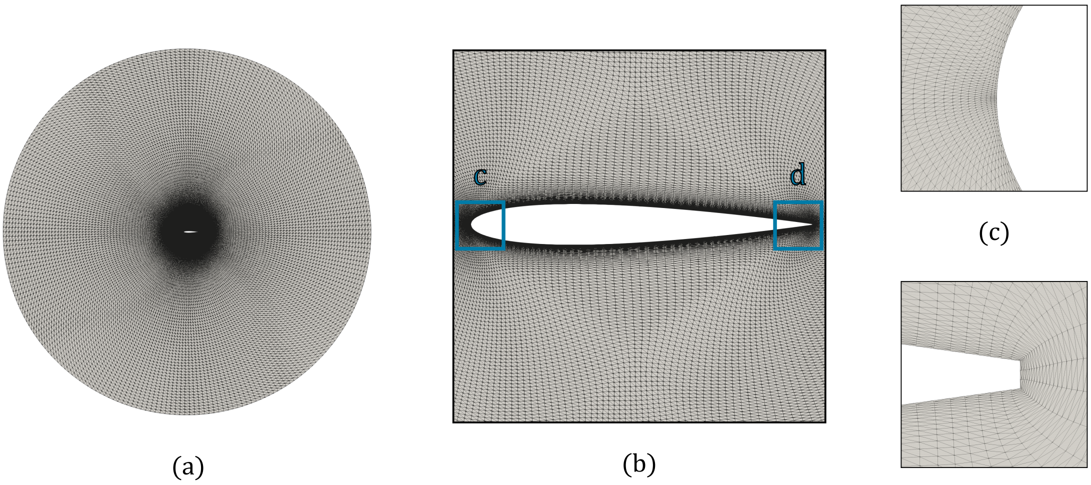

(a)

(b)

(c)

(d)

Figure 5.2: Details of the CFD mesh: (*a*) complete fluid domain, (*b*) close-up of the aerofoil, (*c*) leading edge and (*d*) trailing edge zoomed-in.

suction LEV, due to the appearance of an LEV on the pressure side, has been documented before for similar pitching profiles with a trailing edge pivot axis, for high reduced pitch rates of $K_\alpha = 0.2$ (Granlund et al., 2013), $K_\alpha = 0.39$ (Yu & Bernal, 2017), and $K_\alpha = 0.7$ (Ol et al., 2009).

5.3.2 CFD model for unsteady rigid aerofoils

Camber morphing is not considered in this chapter, so the geometries studied are not equipped with a trailing-edge flap. These are a NACA 0004 and a NACA 0012 aerofoils in clean configuration. Flow conditions also differ slightly from those in Chapter 3. Therefore, a better suited CFD model was developed for validation of the low-order models used in this chapter, whose details are provided as follows. The aerofoil chord length was 3 inches, and the free stream velocity 0.1312 m/s, resulting in a Reynolds number based on the chord $Re = 10^4$ for these unsteady flow simulations. O-meshes (instead of an overset-mesh) were constructed for these clean geometries. The far field extended to 12 chord lengths in all directions, as depicted in Fig. 5.2(*a*). The number of cells around the aerofoil was 246, with a fine resolution near the leading edge and the trailing edge, as observed in Figs. 5.2(*c*) and 5.2(*d*), and the number of cells in the wall-normal direction was 257. The no-slip boundary condition was enforced on the surface of the aerofoil, and free stream (inlet/outlet) boundary conditions were used for the far field. This behaves as a zero-gradient condition when fluid is flowing out of the boundary face, and as a fixed value condition (equal to the free stream) otherwise. Solver setting for CFD simulations was the same as described in §3.3 for the multi-body problem.

5.3.3 Flow separation: Leading-edge suction

The new model introduced in this chapter brings an important advantage in that no empirical parameter is needed to incorporate the influence of viscosity. On the other hand, without this critical parameter the information about the start of flow separation is lost. Hence an alternative procedure is necessary to retain knowledge about this viscous phenomenon.

Identification of flow separation

Qualitatively, flow separation can be inferred by monitoring a sequence of flow field images. By studying the trend of some theoretical variables at desired time instants, a more quantitative form can be produced. A careful evaluation of the sign of a function's derivatives at a given point provides meaningful information on its local behaviour. The first derivative can be seen as the slope of the tangent line to the function. It tells us if the function increases or decreases locally. Whereas the second derivative explains the behaviour of the first derivative: if the second derivative is positive the slope of the graph increases with x and vice versa.

In a bid to ascertain the time instant at which flow separates using the new formulation, the leading-edge suction parameter is examined, and by extension the edge velocity of the shear layer (scaled with $\mathcal{L}$) and the vortex-element strength (scaled with $\mathcal{L}$ squared). Observing the state of these magnitudes at the time step when flow starts to separate at the leading edge from CFD vorticity images, a slope lessening is noticeable in their curves about this time, meaning a change in rate of vorticity creation. Mathematically, this translates into the first derivative having the same sign as the function, and the second derivative having the opposite sign. Returning to Eqs. (5.4) and (5.6), the expressions of the functions' derivatives are:

$$\frac{\mathrm{d}u_{LE}(t)}{\mathrm{d}t} = \sqrt{\frac{2}{r_{LE}}} U \dot{A}_0(t) \quad , \tag{5.8a}$$

$$\frac{\mathrm{d}^2u_{LE}(t)}{\mathrm{d}t^2} = \sqrt{\frac{2}{r_{LE}}} U \ddot{A}_0(t) \quad , \tag{5.8b}$$

for the leading-edge velocity, and:

$$\frac{\mathrm{d}\Gamma_i(t)}{\mathrm{d}t} = 2\frac{U^2\Delta t}{r_{LE}} A_0(t)\dot{A}_0(t) \quad , \tag{5.9a}$$

$$\frac{\mathrm{d}^2\Gamma_i(t)}{\mathrm{d}t^2} = 2\frac{U^2\Delta t}{r_{LE}} \left[\dot{A}_0^2(t) + A_0(t)\ddot{A}_0(t) \right] \quad , \tag{5.9b}$$

for the vortex particle strength.

The sign of the functions depends upon the side of the aerofoil over which flow separates: positive when the LEV is forming on the suction side, negative if it forms on the pressure side. For the first case the curves exhibit a concave-down shape, which corresponds to a positive first derivative and a negative second derivative. Applying these guidelines to Eqs. (5.8) and (5.9) the following inequalities are obtained:

$$\dot{A}_0(t) > 0 \quad , \quad \ddot{A}_0(t) < 0 \quad , \tag{5.10}$$

for the velocity at the leading edge, and:

$$A_0(t)\dot{A}_0(t) > 0 \quad , \quad \ddot{A}_0(t) < -\frac{\dot{A}_0^2(t)}{A_0(t)} \quad , \tag{5.11}$$

for the strength of vortex particles.

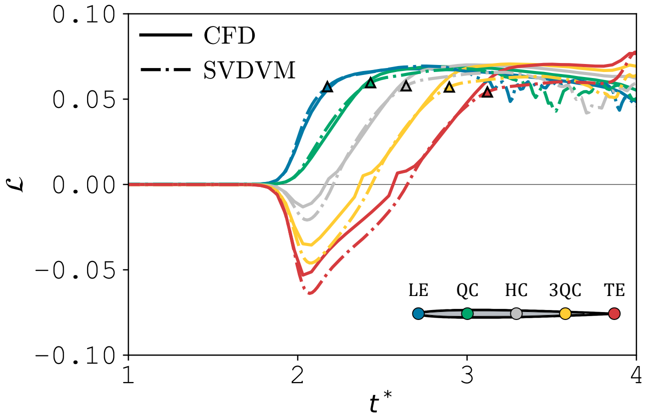

Figure 5.3: Evolution of $\mathcal{L}$ during leading-edge flow separation for a NACA 0004 aerofoil pitching about five pivot axes (LE, QC, HC, 3QC, TE). Predictions from SVDVM (-·-·) are compared against calculations from CFD (——). Coloured triangles mark the onset of flow separation according to Eq. (5.12).

In summary, the system of inequalities to enforce to the *zero*-th Fourier coefficient and its derivatives is:

$$\left.\begin{array}{ll} A_0(t) > 0\ , \quad \dot{A}_0(t) > 0\ , \quad \ddot{A}_0(t) < -\dfrac{\dot{A}_0^2(t)}{A_0(t)} & \text{for suction side LEV} \\ A_0(t) < 0\ , \quad \dot{A}_0(t) < 0\ , \quad 0 < \ddot{A}_0(t) < -\dfrac{\dot{A}_0^2(t)}{A_0(t)} & \text{for pressure side LEV} \end{array}\right\} . \tag{5.12}$$

The onset of leading-edge separation in this work is suggested to correspond with the instant at which the absolute value of $\ddot{A}_0(t)$ is maximum (local minimum for the suction side, and local maximum for the pressure side) within the range where the system of inequalities (5.12) is satisfied. The timing of such a maximum lies slightly before the global maximum of $\mathcal{L}$ is reached. Figure 5.3 compares the evolution of $\mathcal{L}$ between SVDVM and CFD (extracted as described in Appendix B.1) for a NACA 0004 pitching about five different pivot locations. The onset of separation is indicated with markers, and its timing is consistent with findings by He et al. (2020), who inferred that dynamic stall development is not governed by the maximum $\mathcal{L}$, as Ramesh et al. (2014) thought.

Table 5.2: Values of $\mathcal{L}$ at the onset of LEV formation: critical value for LDVM-based models, and value at flow separation for SVDVM.

	NACA 0004	NACA 0012
criterion P	0.16	0.32
criterion I	0.12	0.27
criterion $\ddot{A}_0$	0.05	0.17

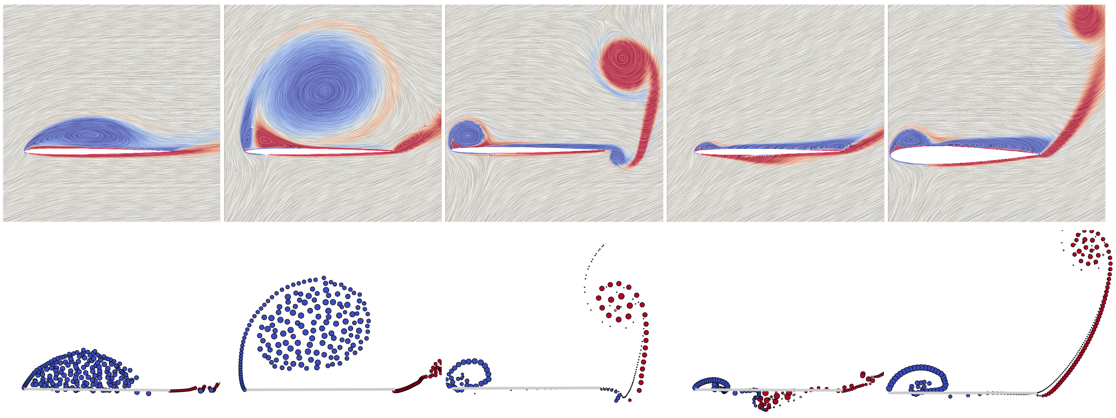

(a) (b) (c) (d) (e)

Figure 5.4: Characteristic LEV shapes for different kinematics/geometries as modelled with CFD (top images) and SVDVM (bottom images): (*a*) slow pitch rate, (*b*) medium pitch rate, (*c*) high pitch rate, (*d*) pivot axis at the rear half and (*e*) thick aerofoil. All plots are shown in the reference frame of the aerofoil at an arbitrary time instant.

Critical $\mathcal{L}$ values obtained with *criterion P* and *criterion I* are collected in Table 5.2 for the two cases studied in this chapter. The value of $\mathcal{L}$ at the onset of flow separation according to the methodology just introduced, termed *criterion* $\ddot{A}_0$ hereinafter, is also included. As it will be discussed in subsequent sections, the *variable-*$\mathcal{L}$ model will enable improved predictions of leading-edge vortex dynamics compared to the *constant-*$\mathcal{L}$ models.

To assess its performance, the new criterion proposed from Eq. (5.12) to determine the onset of flow separation was tested over a broad range of kinematics and geometries characterised by very diverse LEV shapes. Results were compared against CFD simulations, and vorticity contours at representative instants of the vortex evolution are exhibited in Fig. 5.4. The selection of cases was motivated by the knowledge that increasing the reduced pitch rate strengthens the LEV, delaying many of the vortex milestones to larger incidences, and that the same effect is attained by moving the pitch axis aftwards (Eldredge & Jones, 2019). A distinctive shape is the elongated backwards LEV covering the whole surface of slow pitching aerofoils, as shown in Fig. 5.4(*a*). Typical of medium pitch rates is a well-formed round LEV away from the surface, like the one displayed in Fig. 5.4(*b*). Representative of higher pitch rates is the formation of a strong TEV preceding the LEV, which can be clearly seen in Fig. 5.4(*c*). For aerofoils that pitch about a pivot axis over the rear half of the chord, a pressure-side LEV delaying the suction-side LEV is expected, as represented in Fig. 5.4(*d*). Finally, a late formed LEV is characteristic of thick aerofoils, like that in Fig. 5.4(*e*).

Whether or not the removal of the dependency on a critical value has too great an implication on the correct modelling of the complex vortex dynamics, may be assessed only on the basis of its comparison with reference data. The remainder of this chapter aims to analyse different features in the evolution of a vortex and its feeding sheet for both approaches to model the rate of vorticity transport.

Post-stall behaviour of $\mathcal{L}$

Post-separation behaviour of the leading-edge suction parameter is an ongoing matter of research. Numerous low-order models have been built on the hypothesis that it is held fixed at a critical value during the whole vortex formation phase (see examples in §2.2). Notwithstanding the general good estimations of load coefficients in studies using this assumption, recent computational (Narsipur, 2022; Narsipur et al., 2020) and experimental lines of investigation (Deparday et al., 2022; Deparday & Mulleners, 2019) revealed that the leading-edge suction drops shortly after the vortex starts forming at the leading edge. The closure condition set at this point for *constant-*$\mathcal{L}$ models renders them inappropriate to capture the leading-edge suction post-stall behaviour, and therefore to reproduce the correct dynamics of vortex sheets (vorticity transport rate, inclination angle, reattachment process). In contrast, the *variable-*$\mathcal{L}$ model does recreate the observed declining tendency of $\mathcal{L}$. The positive-slope of the suction parameter decreases following a patch of reversed

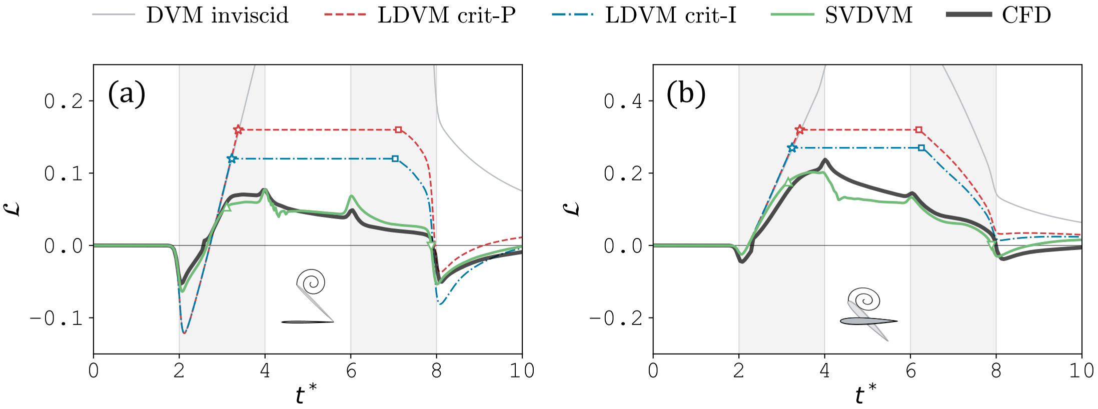

Figure 5.5: Temporal evolution of $\mathcal{L}$: (a) NACA 0004 pitching around its trailing edge and (b) NACA 0012 pitching around its mid-chord. Symbols for LDVM models indicate: onset of LEV formation (⋆) and termination of LEV (□). Symbols for SVDVM indicate: leading-edge flow separation (△) and reattachment (▽).

flow close to the leading edge (visualised through streamlines in CFD simulations), and turns negative slightly after the separated shear layer rolls up into a vortex.

In LDVM-based low-order models, the suction parameter is defined as the *zero*-th Fourier term from unsteady thin-aerofoil theory, given by Eq. (5.1). The post-separation behaviour of this parameter is illustrated in Fig. 5.5 for the three discrete-vortex schemes considered in this chapter (two *constant*-$\mathcal{L}$ models and the *variable*-$\mathcal{L}$ model), and it is contrasted with the value extracted from CFD simulations as discussed in Appendix B.1. For the case of a NACA 0012 aerofoil pitching at its mid-chord, Fig. 5.5(b), prior to the onset of flow separation, which is marked with stars for the *constant*-$\mathcal{L}$ models and a triangle for the *variable*-$\mathcal{L}$ model, the leading-edge suction evolves similarly for both schemes. At this point onwards the predicted values of $\mathcal{L}$ progressively differ between models. Whilst the suction parameter is bounded by the critical value in the original LDVM scheme, it peaks in SVDVM not long after the shear layer separates at the leading edge and starts rolling-up into the nascent LEV. The value of $\mathcal{L}$ then drops as the vortex increases in size and strength. This post-stall behaviour of the leading-edge suction parameter has been observed in recent investigations, and is here only well tracked with the new discrete-vortex model. Once the flow begins to reattach at the leading edge when the aerofoil pitches back down, time instant signalled

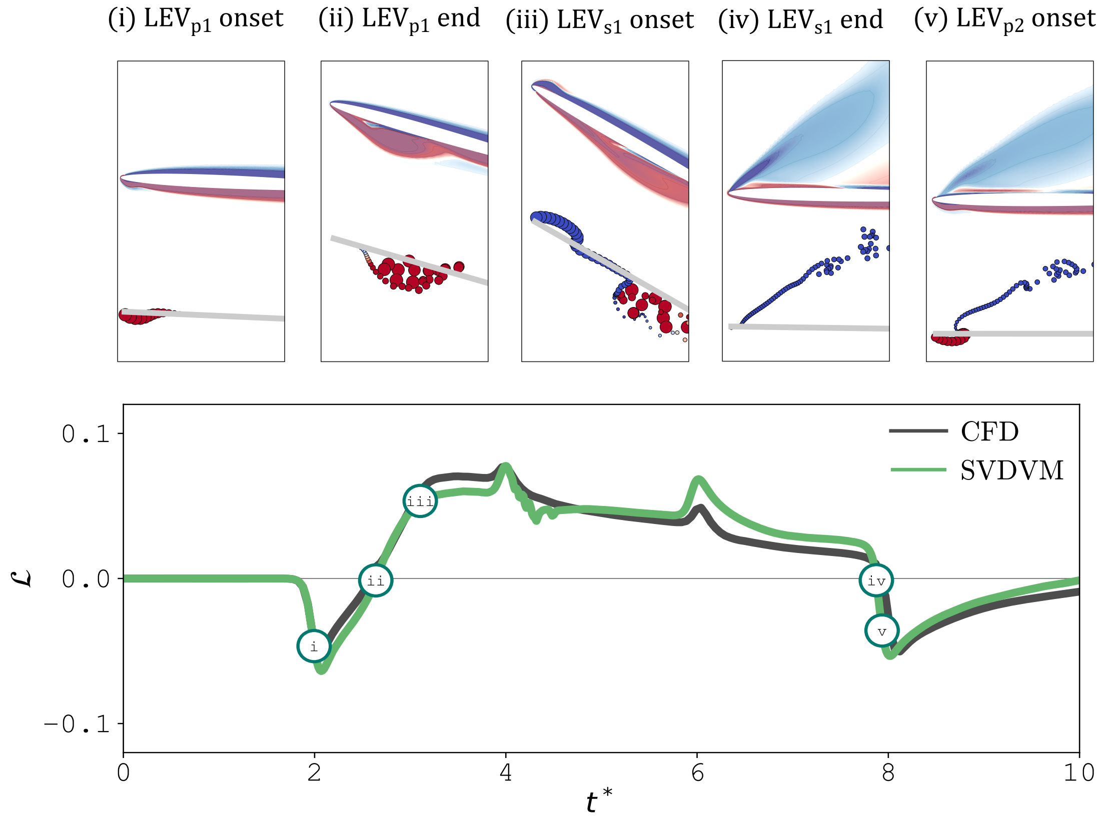

Figure 5.6: Unsteady flow events over a NACA 0004 undergoing a ramp-hold-return pitch motion with the pivot axis at the trailing edge. On the upper sequence of images, vorticity contours from CFD (top) and vortex particles from SVDVM (bottom) are compared. On the lower graph, the corresponding $\mathcal{L}$ value for each flow event is shown. Sub-index p stands for pressure side, and s for suction side of the aerofoil.

with an inverted triangle in the *variable*-$\mathcal{L}$ model, the deviation between both schemes becomes smaller, to finally collapse all three curves by the end of the motion, when the initial steady state is recovered.

It is worth noting that the temporal evolution of $\mathcal{L}$ changes with the pivot location. In Fig. 5.5(a) a NACA 0004 pitches around its trailing edge. The location of the pivot point in the rear half of the aerofoil triggers flow separation over the pressure side before it happens on the suction side. As stated above, the formation process of an LEV influences the suction experienced by the aerofoil. Because the *constant*-$\mathcal{L}$ models do not capture the associated decay in $\mathcal{L}$, the slope of these curves differ from the *variable*-$\mathcal{L}$ model and CFD results after the pressure-side LEV is formed. This is clearly visible in the first grey-shaded region, between $t^* \sim 2$ and $t^* \sim 3$.

The rate of circulation fed into the LEV has been estimated in the new discrete-vortex model through the velocity at the edge of the shear layer. With no empirical parameters needed to determine the temporal evolution of $\mathcal{L}$, SVDVM offers a faster way to model unsteady flow separation, and a more accurate recreation of vortex sheet dynamics. Flow features that characterise unsteady aerofoils, such as vortex formation and flow reattachment, are naturally captured with this new approach, and the sequence of vortex events that occur around the NACA 0004 aerofoil, summarised in Fig. 5.6, is a good case in point: at the beginning of the pitching motion the stagnation point moves towards the upper surface, resulting in $\mathcal{L}$ dropping to negative values. A negative value of the suction parameter means that flow separation, and the consequent formation of an LEV, will occur over the pressure side of the aerofoil (see Eq. (5.12)). This is indicated as event (i) in the graph, and the corresponding flow field from CFD simulations and SVDVM predictions shows the incipient vortex, with red colour representing counter-clockwise vorticity. Immediately after, $\mathcal{L}$ reaches a local minimum, equivalent to what was explained earlier for the case of positive $\mathcal{L}$. As the pitching motion progresses, the stagnation point returns to the leading edge and the suction parameter changes sign, the time instant at which the flow reattaches at the leading edge, event (ii) in the plot. Since the rate at which leading-edge vorticity builds in the SVDVM model is proportional to the instantaneous suction parameter (see Eq. (5.5)), zero-strength particles enter the flow field at this time. The attached flow state is identified as a small region close to the leading edge where no discrete vortices are visible in the bottom image of event (ii). Although the algorithm generates those computational elements carrying very little vorticity, or none at all, they are not perceptible since their radii are proportional to their strength, and they run along the aerofoil's chord line. Next, the stagnation point moves towards the lower surface, and the same sequence is repeated over the suction side of the aerofoil, events (iii) – (iv). The blue colour here indicates clockwise vorticity. By the end of the motion, an LEV with negative vorticity is formed on the pressure side, whilst the shear layer feeding the suction-side LEV continues to attach as the flow convects downwards, event (v).

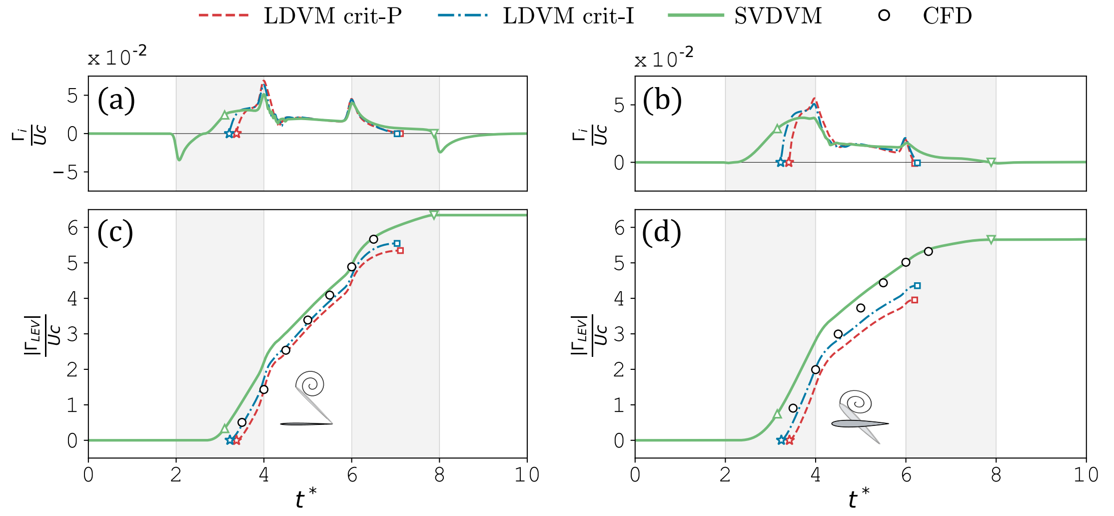

Figure 5.7: Temporal evolution of normalised discrete-vortex strength and leading-edge vortex total circulation: (a, c) NACA 0004 pitching around its trailing edge and (b, d) NACA 0012 pitching around its mid-chord. Symbols for LDVM models indicate: onset of LEV formation (⋆) and termination of LEV (□). Symbols for SVDVM indicate: leading-edge flow separation (△) and reattachment (▽). White circles are from CFD.

5.3.4 Vortex growth: Circulation

Separated shear layers are the initial stage in the formation of vortices, and their feeding mechanism. Vortex dynamics can be successfully predicted by means of vortex methods if the rate of circulation transferred into the vortex through the feeding shear layer is accurately modelled. Vortex elements representing these sheets have individual strengths assigned, Γ_i, which together define the total circulation accumulated within the vortex, Γ_{LEV}. This parameter is a characteristic indicator of the vortex growth stage.

The correlation between these quantities is assessed in Fig. 5.7. Estimated non-dimensional strengths of the i-th discrete vortex released from the leading edge at each time step of the low-order simulation, Γ_i, are displayed in Figs. 5.7(a) and 5.7(b). The novel approach to model leading-edge flow separation presented in this chapter, SVDVM, is compared against the two variants of LDVM introduced in §5.2.1, where the critical value of the leading-edge suction parameter has been determined from CFD according to different signals in the wall shear stress. The strength of shed particles in these methods is governed by the difference between the instantaneous and critical values of $\mathcal{L}$, whilst for the new formulation it is proportional to the instantaneous $\mathcal{L}$ squared, Eq. (5.6). The NACA 0004 case is analysed in Fig. 5.7(a). Regardless of the DVM chosen to model unsteady thin aerofoils, the strength of vortex particles is similar throughout most of the vortex lifespan: soon after the onset of leading-edge flow separation, a local maximum is observed during the ramp-up part of the motion. As the angular acceleration drops during the transition before reaching the final pitch angle, the strength of released particles climbs, to peak at the instant of the largest negative value (maximum deceleration), $t^* = 4$. It follows a short sharp decline due to the deceleration returning to zero. The slope decreases more gently thereafter, when the aerofoil stays stationary at 45° and the only velocity contributing to A_0 is that induced by the growing LEV, $t^* \sim 4$ to $t^* \sim 6$. Analogous later peaks are the product of angular acceleration/deceleration during the transitions in the last segment of the motion, when the aerofoil is pitching back to zero, $t^* \sim 6$ to $t^* \sim 8$. In spite of the overall trend captured by all formulations in a similar manner, there are some meaningful differences: the critical value of $\mathcal{L}$ determined by *criterion P* and *criterion I* is too high for the LEVs formed on the pressure side to be captured, identifiable by negative values of vortex strength in SVDVM, $t^* \sim 2$ and $t^* \sim 8$. This large critical value is also the reason for a later onset of LEV formation on the suction side, denoted by stars in the graph, which ultimately translates into a smaller vortex total circulation. Conversely, SVDVM does manage to model the aforesaid vortices, achieving a smooth transition in the strength assigned to vortex particles where A_0 changes sign, this is where a suction-side LEV succeeds a pressure-side LEV.

One of the improvements attained with the new model is that, through the leading-edge radius, the thickness effect can be included in the calculation of the rate at which leading-edge vorticity builds, Eq. (5.5). This is examined through the NACA 0012 case in Fig. 5.7(b). Whilst the results obtained are largely similar for the NACA 0004, some distinctions can be identified: 1) the specific characteristics of the present motion, where the pivot axis is located at the mid-chord, do not trigger the occurrence of vortices on the pressure side, as was observed for the thinner foil; 2) acceleration spikes at the transition points are less pronounced here due to the pitching axis being closer to the leading edge; 3) flow curvature at the leading edge is lower for thicker aerofoils, allowing them to sustain a higher amount of suction, which translates into larger values of $\mathcal{L}$ at flow separation than for thinner aerofoils. These higher $\mathcal{L}$ values (see Table 5.2) delay the occurrence of the vortex even further, accentuating the difference between models on the individual strength of discrete vortices during the ramp-up phase, between $t^* \sim 3$ and $t^* \sim 4$. Also the final decline, past $t^* \sim 6$, is more abrupt in *constant-*$\mathcal{L}$ models for the same reason.

Non-dimensional LEV circulation, Γ_{LEV}, is depicted in Figs. 5.7(c) and 5.7(d). To enable direct comparison between CFD results, where clockwise vorticity is taken as negative, and low-order model predictions, where the opposite is considered, the absolute value of the total circulation has been plotted. Vorticity is continuously shed and accumulated into the vortex, leading to a progressive growth in circulation magnitude. The same general trend is observed for both aerofoils: two linear sections with different positive slopes, influenced by the kinematics. During the up-stroke (first grey-shaded region) the i-th particle strength rises up to its peak value at the end of the motion (see Fig. 5.7a), leading to a significant circulation growth. Once the motion has ceased contributing to the strength of vortex particles (through A_0) the positive slope gently reduces, yet the circulation still increases as discrete vortices keep adding to the growing LEV. Owing to their higher $\mathcal{L}$ value at flow separation, *constant-*$\mathcal{L}$ models start releasing particles later than the *variable-*$\mathcal{L}$ model, which translates into a lower total circulation. However, dissimilarities between models are barely noticeable for the thin aerofoil case, Fig. 5.7(c), and all curves are in good agreement with CFD data (extracted as explained in Appendix B.2) up to the time of vortex shedding. From this point forwards dissipation effects on the free vortex are expected, but LOM predictions do not account for them, and so the circulation remains at its maximum value indefinitely. Discrepancies between models are more evident for the thicker aerofoil, Fig. 5.7(d). During the down-stroke *constant-*$\mathcal{L}$ models cease releasing particles and their curves stop growing, drifting

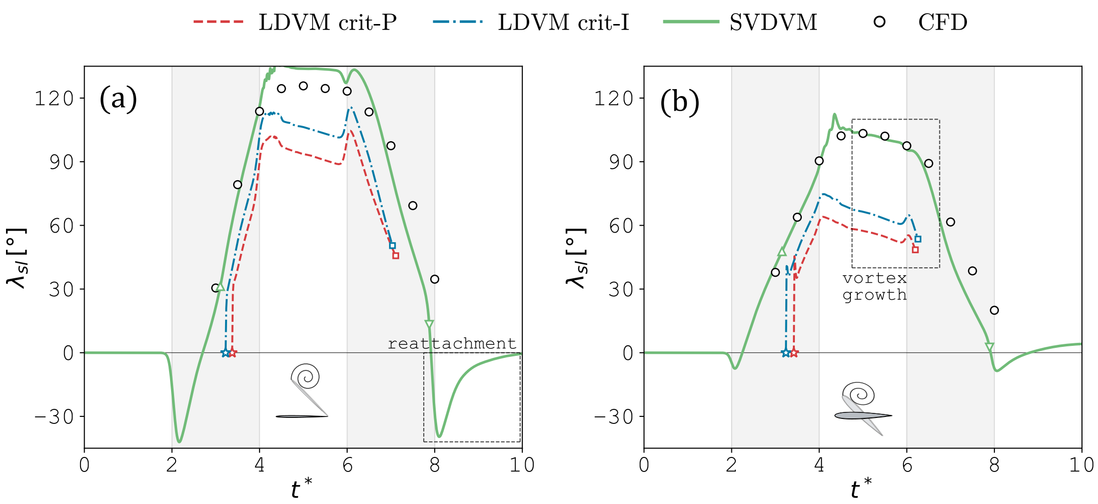

Figure 5.8: Temporal evolution of shear layer slope: (*a*) NACA 0004 pitching around its trailing edge and (*b*) NACA 0012 pitching around its mid-chord. Symbols for LDVM models indicate: onset of LEV formation (☆) and termination of LEV (□). Symbols for SVDVM indicate: leading-edge flow separation (△) and reattachment (▽). White circles are from CFD.

the maximum predicted value of vortex circulation away from that of CFD. The *variable*-$\mathcal{L}$ model on the contrary provides an accurate estimation of that peak value.

5.3.5 Flow reattachment: Shear layer angle

The interplay between vortex particles distributed in the flow field is the essence of vortex methods. The amount of vorticity each of these discrete elements carries has a critical role in modelling vortex dynamics, since the strength and inclination of the sheet they represent will solely depend on their mutual interactions. With the interest focused on the leading edge, the performance of vortex methods can be assessed by observing the angle that the separated vortex sheet forms with the chord line, λ_{sl}. In DVM models it can be computed with the last two discrete vortices shed. The methodology followed to obtain this angle from CFD simulations is detailed in Appendix B.3. The temporal evolution of the shear layer slope is exhibited in Fig. 5.8 for both, the thin and the thick aerofoils. For the *variable*-$\mathcal{L}$ model the entire history has been traced, whereas only the formation and growth stages of the suction-side LEV are represented for the *constant*-$\mathcal{L}$ models, which are unable to reproduce the reattachment process. Results from CFD, represented

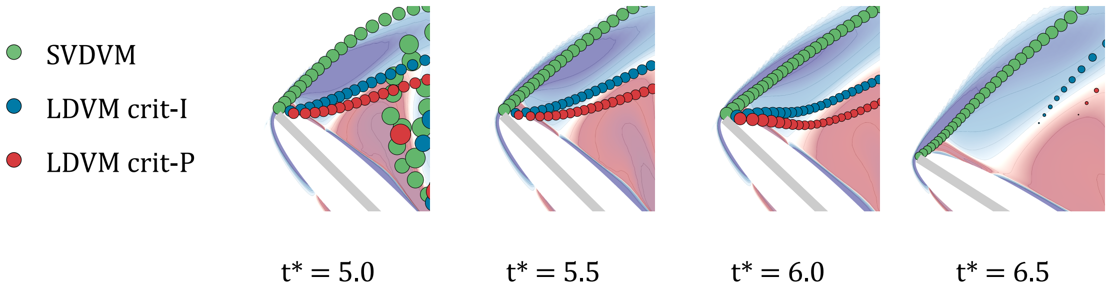

Figure 5.9: Dynamics of the leading-edge vortex sheet during LEV growth stage for the NACA 0012 aerofoil. Vorticity contours from CFD are overlaid with vortex particles from the three DVMs.

by white circles in the graphs, span from the onset of flow separation to the point at which it reattaches at the leading edge as determined by SVDVM, marked with a triangle and an inverted triangle respectively. The separated shear layer moves away from the surface as the aerofoil pitch angle increases, reaching its maximum inclination when the angular deceleration ceases entirely, shortly after $t^* = 4$. With the aerofoil motionless, the flux of vorticity through the feeding shear layer lessens during the vortex growth stage, pulling it back closer to the surface as the coherent vortex structure convects downstream. Graphically, this is observed as a gentle decrease in λ_{sl} between $t^* \sim 4$ and $t^* \sim 6$. Because the growth rate of circulation at the leading edge is nearly the same for all models at this stage (see Figs. 5.7*a* and 5.7*b*), all curves fall with a similar decline. The magnitude of λ_{sl} is however smaller the higher the critical $\mathcal{L}$. A higher critical value means that it will take longer for the first leading-edge vortex particle to enter the flow field. Consequently, such starting discrete vortices will be weaker than the one placed at that time instant if a smaller critical value was calculated, since in that case the vortex sheet would have already started developing, and the growth rate of circulation would be increased (see Figs. 5.7(*a*) and 5.7(*b*) between $t^* \sim 3$ and $t^* \sim 4$). Weaker particles in the flow field are convected faster with the incoming flow, thus resulting in a smaller angle of separation.

To visually reinforce the tendency of the separated vortex sheet observed for the three DVMs and CFD simulations, a sequence of images zoomed-in on the leading edge of the NACA 0012 aerofoil is exhibited in Fig. 5.9. The time interval shown, from $t^* = 5.0$ to $t^* = 6.5$, is indicated with a dashed square in Fig. 5.8(*b*), and comprises most of the vortex growth stage, when the LEV displays its distinctive fully-developed shape. It is interesting to recall here the inherent limitation of *constant-$\mathcal{L}$* models in properly capturing vortex sheet dynamics: when the instantaneous value of the theoretical A_0 drops below the critical value release of leading-edge vorticity terminates, and no more leading-edge vortex particles enter the flow field. Previously shed discrete vortices continue to move downstream with the incoming flow, which results in the vortex sheet being no longer connected to the aerofoil (last image of the sequence, $t^* = 6.5$). CFD contours evince however that at this time instant the fully-developed LEV still remains attached to the aerofoil through the shear layer. This is only reproduced with the novel approach introduced in this chapter to model vorticity feeding rate, where a new computational element is placed at every time step of the numerical simulation, and its strength estimated with the velocity at the edge of the shear layer, Eq. (5.6).

As remarked above, numerical computations of shear layers with *constant-$\mathcal{L}$* models entails a certain degree of inaccuracy, since the vortex sheet detaches from the leading edge when suction falls below a certain value. Accordingly, results presented for the remainder of this section include only the estimations made by the *variable-$\mathcal{L}$* model and CFD calculations. During the return part of the ramp motion, the second grey-shaded area in Fig. 5.8, the aerofoil goes back to its initial position, and the slope of the separated shear layer progressively reduces until the flow reattaches at the leading edge. Numerically, this has been defined as the instant when leading-edge suction becomes null (see Fig. 5.6), and it is indicated in the graph with an inverted green triangle. Low-order predictions of the shear layer angle underestimate results given by high-fidelity computations. A plausible explanation might have its origin in the geometry below the reattaching layer. Low-order models simplified the aerofoil to a line, allowing a zero value for λ_{sl} at reattachment, whereas the rounded leading edge in CFD simulations imposes a geometric constraint, precluding that zero angle from being reached.

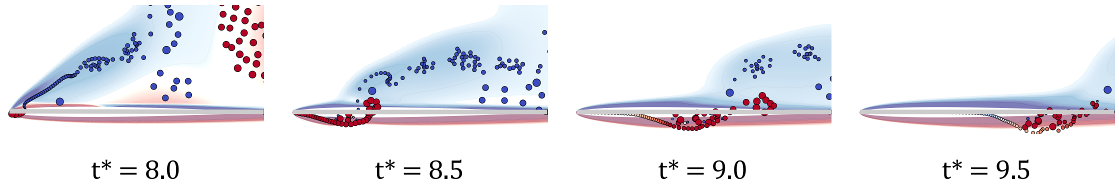

Figure 5.10: Dynamics of the leading-edge vortex sheet during the reattachment process for the NACA 0004 aerofoil. Vorticity contours from CFD are overlaid with vortex particles from SVDVM.

Finally, with the aerofoil at rest back at a zero angle of attack, the reattached region is extended from the leading edge rearwards, until it encompasses the whole surface of the aerofoil and the initial undisturbed flow state is recovered. By including the velocity at the leading-edge shear layer in the calculation of vortex particle strength, SVDVM accurately updates in time the position of the shear layer. The reattaching process is illustrated for the NACA 0004 aerofoil in Fig. 5.10. The time interval shown, $t^* = 8.0$ to $t^* = 9.5$, corresponds to the dashed square highlighted in Fig. 5.8(a).

5.3.6 Aerodynamic coefficients. Reynolds number effect

Contrary to other canonical motions (like translation or rotation), for pure pitching manoeuvres the Reynolds number is believed not to have a significant role in the initial development of the LEV, at least in the range $\mathcal{O}(10^2)$ to $\mathcal{O}(10^4)$ (Eldredge & Jones, 2019). In early experimental investigations into dynamic stall, it was observed that Reynolds number had little effect on aerodynamic load coefficients, but the leading-edge profile did have a larger impact (McCroskey, 1982). These findings have been more recently supported with computational evidence (Narsipur, 2022; Narsipur et al., 2020). The influence of these two variables, thickness and Reynolds number, on the performance of discrete-vortex models in LEV-dominated scenarios is explored in this section.

Regarding the aerofoil shape, the time history of the aerodynamic coefficients is examined for the two cases studied in Fig. 5.11, where predictions made by the low-order models are compared against results obtained from CFD simulations. Overall, the different approaches to determine the rate of circulation fed into an

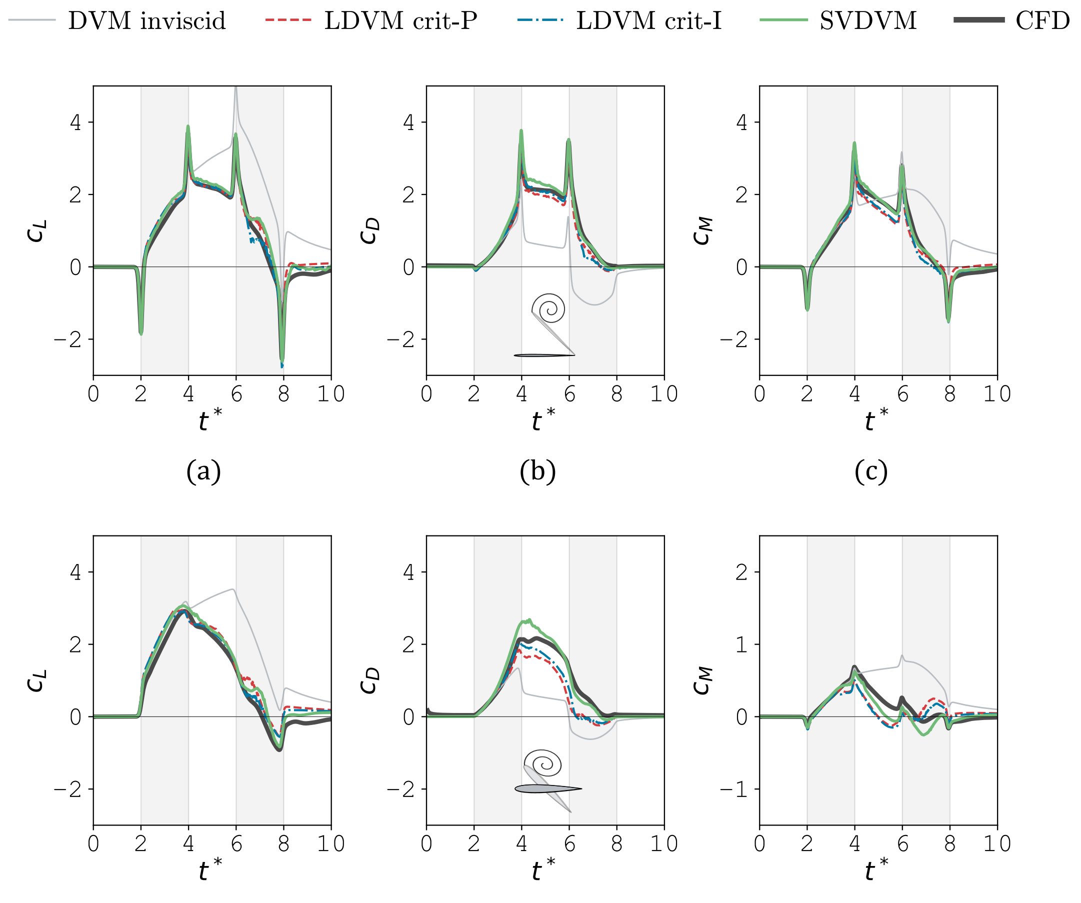

(a) (b) (c)

(d) (e) (f)

Figure 5.11: Aerodynamic coefficients time history for a NACA 0004 pitching around its trailing edge: (a) lift, (b) drag and (c) pitching moment; and for a NACA 0012 pitching around its mid-chord: (d) lift, (e) drag and (f) pitching moment

LEV reveal minor variations when compared to the high-fidelity simulations for the thin aerofoil case, Figs. 5.11(a) to 5.11(c). Added-mass effects, indicated by spikes when angular accelerations are large, are particularly pronounced for this kinematic condition and correctly captured by both discrete-vortex schemes. Curves from CFD data are closely tracked during the entire time series, aside from minor dissimilarities over the down stroke phase of the motion (second grey-shaded region in the graphs), from $t^* = 6.0$ to $t^* = 8.0$. Differences become more noticeable for the thick aerofoil case, Figs. 5.11(d) to 5.11(f), especially over the time interval mentioned. Some of the most significant distinctions between models occur here, and *constant-$\mathcal{L}$* models fail to keep a good agreement with CFD results. If the strategy adopted to define the shedding rate of vorticity is based on a critical value of the leading-edge suction parameter, it is during this part of the motion when the theoretically predicted A_0 falls below the limiting value (see squares in Fig. 5.5). Furthermore, the strength of the last released vortex particles rapidly decays (see Figs. 5.7(a) and 5.7(b), and last snapshot in Fig. 5.9, where the size of particles is proportional to their strength). With no more discrete vortices entering the flow field vorticity is no longer built at the leading edge, and the vortex sheet breaks off (see Fig. 5.8), affecting the contribution of the LEV to the aerodynamic loads. On the contrary, the *variable-$\mathcal{L}$* model estimates aerodynamic loads with higher accuracy, which is particularly marked on the drag and moment coefficients, Figs. 5.11(e) and 5.11(f). Although SVDVM estimation of the moment coefficient is slightly more negative than the CFD results the trend is properly followed, whereas LDVM-based models fail to capture the characteristic shape in this phase of the motion. The function of LEVs is to prevent leading-edge vorticity from advecting downstream, and in SVDVM the leading-edge vortex sheet remains adhered to the bound vortex sheet during that time interval. The improvement with this approach can then be justified by the build up of vorticity not being inaccurately halted during the down stroke (see Figs. 5.7 and 5.8). The component of the aerodynamic loads due to the vortex is therefore not negatively impacted.

Having removed the need of an empirical value for the development of SVDVM, it is logical to inquire how important the effect of the Reynolds number might be on the performance of this novel discrete-vortex model. In order to examine this, an additional test case is included following the work by Narsipur et al. (2020): a NACA 0012 aerofoil pitching harmonically about its quarter chord at a reduced frequency of $k_\alpha = 0.4$. Two different Reynolds numbers, $Re = 3 \cdot 10^4$ and $Re = 3 \cdot 10^6$, are considered in that work. Reference CFD data was taken from the supplementary material accompanying the paper.

The aerodynamic load coefficients estimated with the *variable-$\mathcal{L}$* model are compared with the reference CFD data in Fig. 5.12. In view of the results, the effect of the Reynolds number on aerodynamic loads seems to be minimal, despite

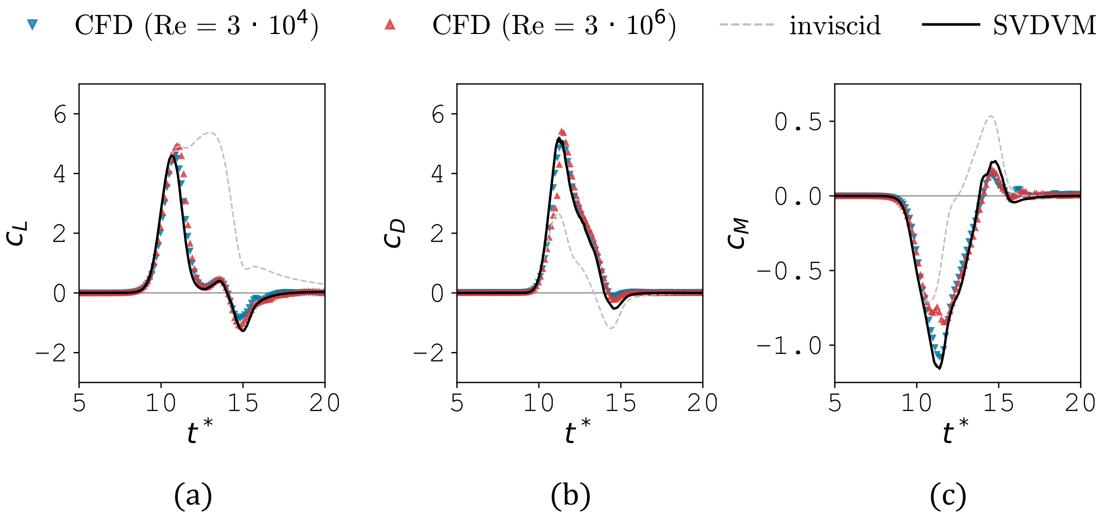

Figure 5.12: Reynolds number effect on the aerodynamic loads for a NACA 0012 aerofoil pitching harmonically about its quarter chord: (a) lift, (b) drag and (c) pitching moment. Results are from SVDVM (——) and CFD data (▽ , △).

being a difference of two orders of magnitude between cases. This is consistent with the statement made at the beginning of this section. The good agreement between the aerodynamic coefficients predicted by SVDVM and CFD data might mislead about the range of Reynolds numbers for which the low-order model provides reliable estimations of unsteady flows.

From the aerodynamic loads coefficients alone it is difficult to assess the performance of the model in full, and it would not be wise to extrapolate the outcome to other aspects such as flow field modelling. In a bid to better understand the real scope of accurate predictions, the temporal evolution of the leading-edge suction parameter (a reliable indicator of the state of the flow at the leading edge) is compared in Fig. 5.13 for the same Reynolds numbers. The maximum value of $\mathcal{L}$ and its timing are observed to increase with the Reynolds number, being closest to the SVDVM estimation in the lower range. Although during pre-separation and reattachment stages trends are very well captured, the decline in $\mathcal{L}$ associated with vortex formation starts earlier for SVDVM. This could mean that the actual flow regime for which the model accurately predicts unsteady flow features, such as leading-edge flow separation, is below $Re = 3 \cdot 10^4$. However, further research is required before a definitive statement could be made. It would be interesting

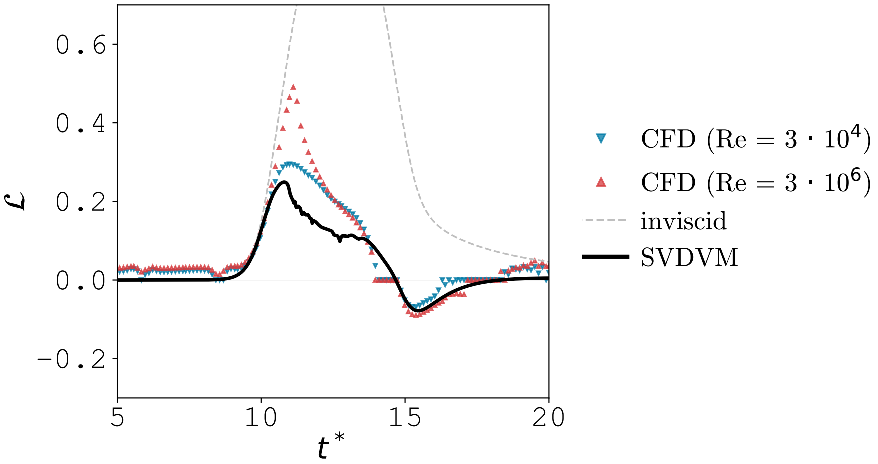

Figure 5.13: Reynolds number effect on $\mathcal{L}$ for a NACA 0012 aerofoil pitching harmonically about its quarter chord. Results are from SVDVM (——) and CFD data (▽ , △).

to examine the behaviour for even lower Reynolds numbers, between $\mathcal{O}(10^2)$ and $\mathcal{O}(10^3)$, to cover the spectrum seen in biological and bio-inspired flight research, where the use of discrete-vortex methods is gaining popularity.

5.4 Flow separation due to flap motion

The acronym MDVM introduced in Chapter 3 refers to a morphing discrete-vortex model. Although vorticity was shed only from the trailing edge in that chapter, modelling of leading-edge vorticity shedding as discussed in the present chapter is also valid for deforming camber lines. The acronym will then be kept for the final version of the low-order model to simulate vortex flows around morphing foils developed in this dissertation.

Originally studied in §3.4.5, the large-flexion ratio large-amplitude oscillating trailing-edge flap, $\frac{c_f}{c} = 0.5$ and $\delta_{max} = 45°$, triggered the occurrence of leading-edge flow separation, which was visualised through CFD vorticity contours (see Fig. 3.18). Because in that chapter no shedding of leading-edge vorticity was assumed in the construction of the low-order model, no particles were released from that point. The case is revised in this section using the updated version of MDVM, where leading-edge vorticity shedding has been accounted for (see §5.2.2). The spatial distribution of vortex particles in the flow field now showcases how flow separates at

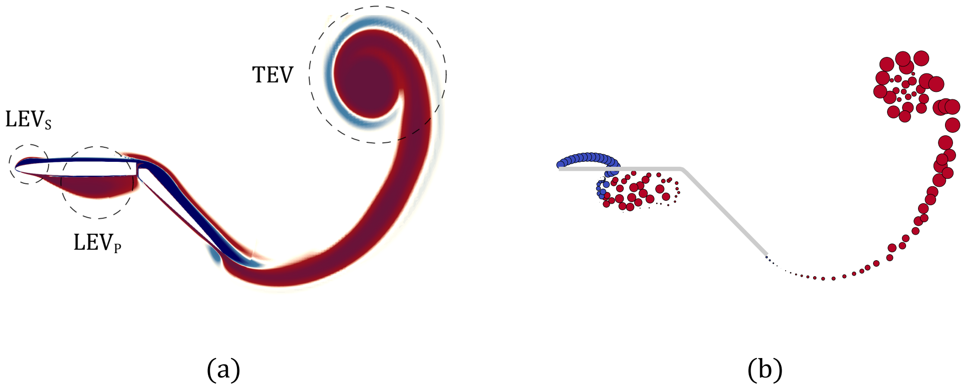

Figure 5.14: Leading-edge flow separation with harmonic flap oscillations (see §3.4.5): (*a*) vorticity contours from CFD and (*b*) vortex particles from the modified version of MDVM. Unsteady flow hallmarks: pressure-side leading-edge vortex (LEV$_P$), suction-side leading-edge vortex (LEV$_S$) and trailing-edge vortex (TEV).

the leading edge, alternating between the suction and pressure side of the aerofoil (flow separates twice every cycle of flap motion). As a result, small vortex structures form with opposite sense of rotation, visible in Fig. 5.14 and highlighted as LEV$_S$ (suction-side LEV) and LEV$_P$ (pressure-side LEV).

5.5 Summary

The motivation of this chapter comes from the critical role that estimations of vorticity shedding rate play on the modelling of vortex-dominated flows. Numerous discrete-vortex models assume a constant post-stall evolution of the leading-edge suction, inaccurately halting the production of vorticity. After leading-edge suction falls below a critical value the vortex sheet breaks off from the leading edge, making these models incapable of reproducing later vortex dynamics traits like the reattachment process.

This chapter has aimed to address the weaknesses highlighted by proposing an alternative strategy for vortex methods to estimate the rate at which leading-edge vorticity is produced, in terms of the velocity at the outside edges of the shear layer. The resultant expression for the rate of circulation fed through the shear layer is proportional to the square of the leading-edge suction parameter, and inversely proportional to the leading-edge radius. This allows, on the one hand to include the effect of thickness in the computation, and on the other hand to naturally capture the evolution of leading-edge suction during the vortex formation process.

A new discrete-vortex model with this implementation has been derived, and named SVDVM. Its performance has been tested for two different profiles, a NACA 0004 and a NACA 0012, undergoing a canonical pitch ramp manoeuvre. By including the velocity at the edge of the shear layer in the calculation of vortex particle strength, this model improves predictions of vortex sheet dynamics compared to the other class of discrete-vortex models. The position/inclination of the separated shear layer is accurately updated in time, capturing unsteady flow features such as its reattachment. As an illustrative example of the capacity SVDVM has in modelling LEV-dominated scenarios, comparison of normalised vorticity with CFD simulations is exhibited: for the ramp-up segment in Fig. 5.15, for the ramp-hold stage in Fig. 5.16, and for the ramp-return phase in Fig. 5.17.

Additionally, a criterion to determine the onset of flow separation has been proposed through a system of inequalities to be enforced to the *zero*-th Fourier coefficient and its derivatives. Its validity has been tested over a broad range of kinematics, yielding reliable estimations of the time instant at which flow separates at the leading edge for the cases studied.

The effect of Reynolds number on the accuracy of low-order predictions has been analysed with data from the literature, and preliminary results suggest a better performance at lower Reynolds numbers. However, this observation is based only on the available data used for comparison, and further study should verify the exact scope for which unsteady flow simulations are suitable. This could serve to remove the empirical dependency of discrete-vortex models for these flow regimes.

Lastly, the applicability of the low-order model for variable-camber foils has been demonstrated. This has been achieved by successfully recreating an oscillating flap case from Chapter 3 where flow separation at the leading edge was provoked by the flap motion. The validated extension of this model to deforming foils sets the groundwork to characterise the alteration of LEV development through trailing-edge flexion, the subject of the following chapter.

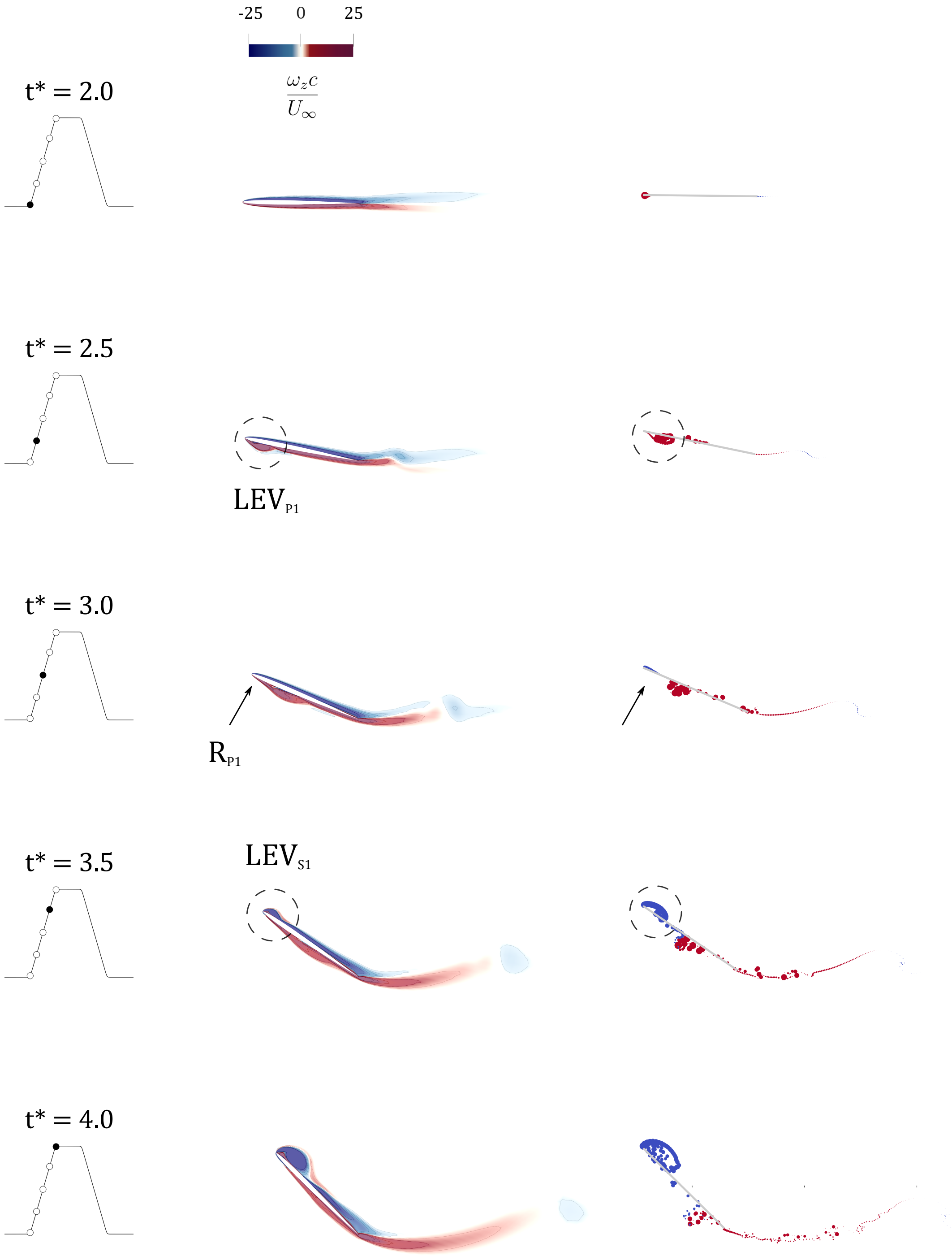

Figure 5.15: Out-of-plane vorticity comparison between CFD (left) and SVDVM (right) simulations for the NACA 0004 aerofoil during the ramp-up segment. Critical unsteady flow features are highlighted: pressure-side leading-edge vortices (LEV_P), suction-side leading-edge vortices (LEV_S) and flow reattachment on the pressure side (R_P).

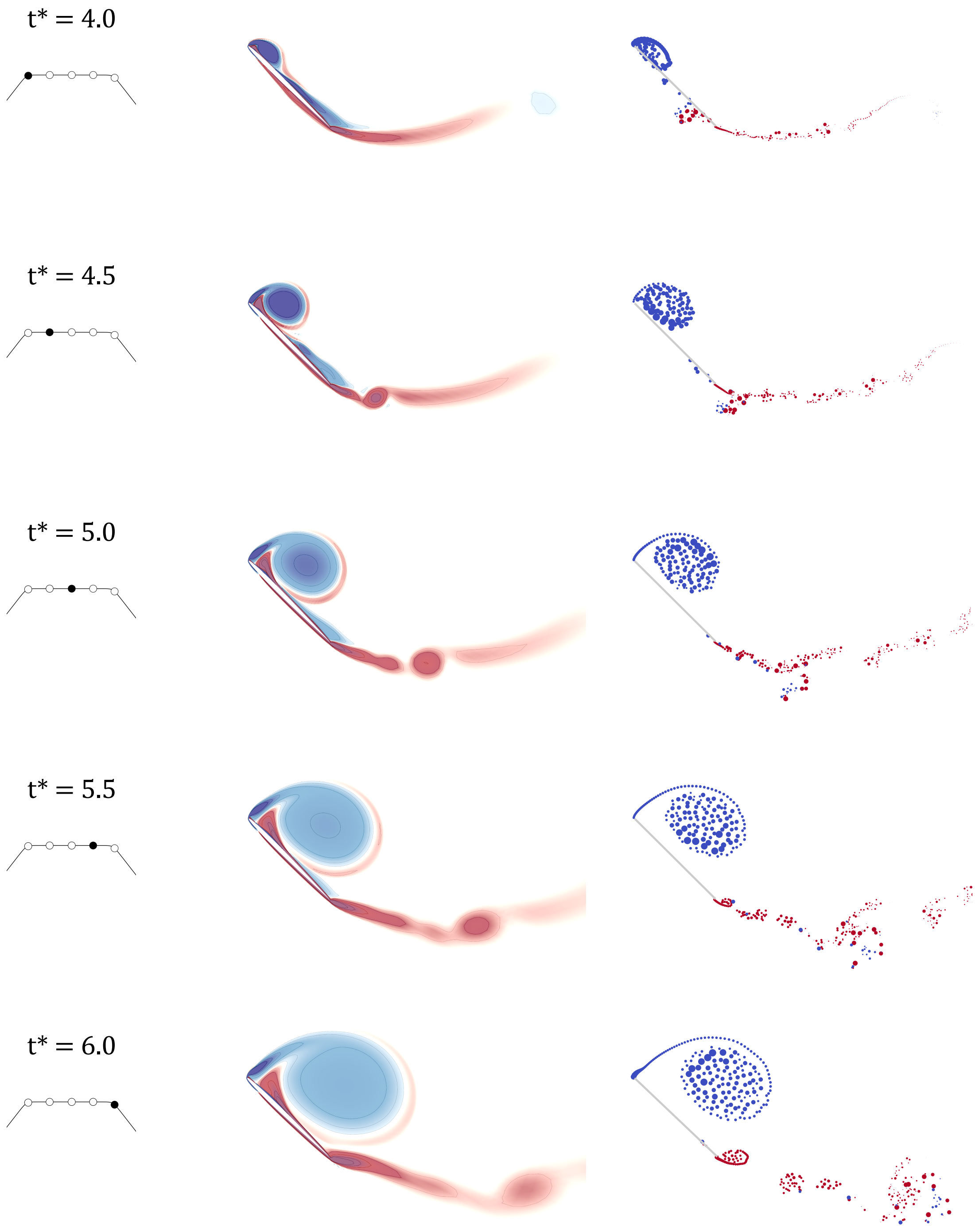

Figure 5.16: Out-of-plane vorticity comparison between CFD (left) and SVDVM (right) simulations for the NACA 0004 aerofoil during the ramp-hold segment.

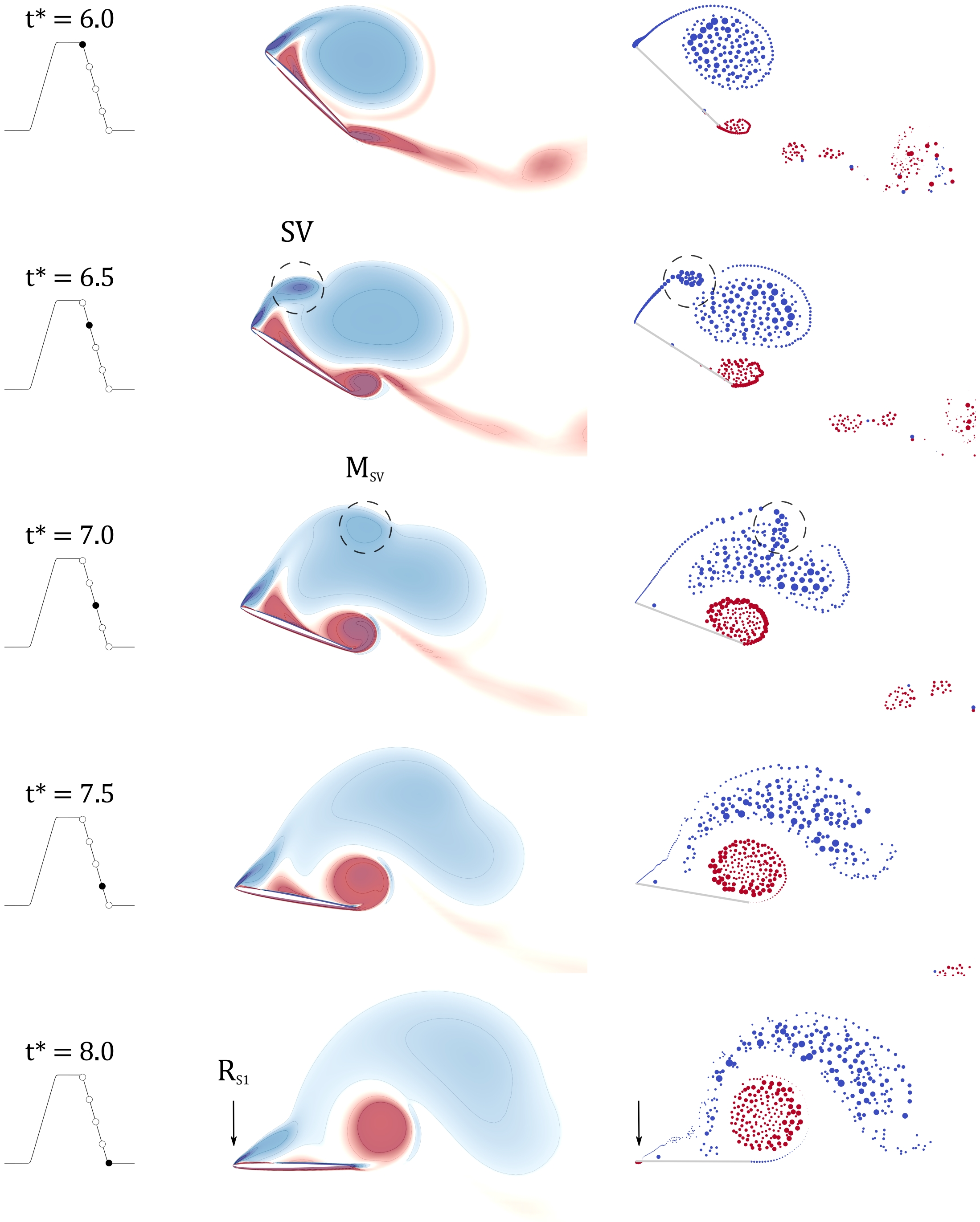

Figure 5.17: Out-of-plane vorticity comparison between CFD (left) and SVDVM (right) simulations for the NACA 0004 aerofoil during the ramp-down segment. Critical unsteady flow features are highlighted: formation and merger of secondary vortices (M_{SV}) and flow reattachment on the suction side (R_S).

Who controls the past controls the future.
Who controls the present controls the past.

— George Orwell

6

LEADING-EDGE VORTEX: MODULATION

6.1 Introduction

CONTROL of unsteady flows is instinctively achieved by natural flapping flyers. They resort to very diverse techniques which confer them with great manoeuvrability. Combining rapid motions with complex deformations they switch between flight regimes of attached and separated flow while maintaining excellent control authority. Pressure gradient modulation via wing shaping stands out as one of the best suited techniques for flow separation control at Low-Reynolds numbers (Gad-el-Hak, 2000). The idea of dynamic camber has stimulated multiple studies, and whilst the general interest has been on the influence this strategy has on the instantaneous aerodynamic loads produced, few have looked at the direct impact on the flow field and the evolution of resultant vortex structures (Harbig et al., 2013; C. Li et al., 2015; Y. Liu et al., 2015). Leading-edge vortex has widely been accepted as the foremost determinant of high forces generated by flapping wings, and it has been hypothesised that camber achieved through trailing-edge flexion causes correlated alteration of the vorticity at the leading edge, and subsequently the magnitude of aerodynamic coefficients (Zhao et al., 2011).

Taking this fundamental relation forwards, the discrete-vortex model developed in Chapter 3 to simulate shape-varying foils in unsteady flow scenarios, and the criterion introduced in §5.3.3 to determined the onset of flow separation at the leading edge, are combined in this chapter to explore the capacity of camber morphing in altering vortex structures characteristics. A quantitative picture of the effect of trailing-edge flap deflections on leading-edge vortex formation time and strength is derived through modulation of the leading-edge suction parameter history.

This chapter serves multiple purposes. It assesses the performance of the low-order morphing model under more complex kinematics than thus studied so far, in the presence of leading-edge vorticity shedding, by combining pitch motion and temporal deformations along the chord in §6.2. It illustrates the potential of trailing-edge flexion in altering vortex features, like formation time and strength, through modulation of the leading-edge suction parameter in §6.3, and it provides fundamental insight into this correlation. The chapter closes drawing conclusions in §6.4.

6.2 Combined pitching and trailing-edge flexion

In Chapter 3 emphasis was placed on the shape of the camber line during deformations of an aerofoil, rather than its impact on the flow field. The kinematic analysis assessed the validity of the model to perform large amplitude trailing-edge deflections, without exploring the topic of flow separation. On the contrary, Chapter 5 has been solely concerned with the temporal evolution of the fluid around unsteady aerofoils, without undergoing shape variations. This included flow separation at the leading edge. For an in-depth study of that unsteady phenomenon, a rapid pitching manoeuvre was chosen that ensured flow separation at the leading edge, followed by the formation and growth of a strong vortex structure.

A dynamic manoeuvre involving unsteady separated flow during which a wing rapidly pitches to very high angles of attack ($\alpha \approx 50°$) and deforms simultaneously is observed at the end of a typical gliding-perching sequence on birds flight (Carruthers et al., 2010). Combining the outcomes from both chapters - morphing and vortex modelling - more complex kinematics, like that one, can be defined to alter vortex behaviour. With this aim, a pitching motion at the quarter chord of a NACA 0006 aerofoil is considered, as defined in Eq. (5.7), to which different combinations of ramp-type flap deflection are superimposed. A slight modification has been made to the values in Table 5.1 to have a smoother transition between phases of both motions, using $\sigma = 0.6$ instead. Furthermore, because the main interest is to affect the initial stages in the vortex development (formation and growth), neither shedding nor reattachment are of concern here. Accordingly, the return part of the motion has been omitted, and the duration of the hold part, t^*_{hold}, is large enough for the vortex to grow but not to shed, giving a total duration of the motion $t^* = 5$. Flap kinematics are prescribed with the same values as the pitch motion except for the reduced rate, that is varied to generate seven different cases (including a baseline case with no flap motion) by modifying the effective angle of attack history, Eq. (3.9): three of them experience positive flap deflections (downwards) with $K_\delta = 0.2$, $K_\delta = 0.4$ and $K_\delta = 0.6$, and the other three equivalent negative deflections (upwards).

6.2.1 Aerodynamic loads and flow field

The first step is to validate the low-order model under these combined kinematics against CFD simulations. Low-order predictions of unsteady loads are compared to high-fidelity computations in Fig. 6.1 for a NACA 0006 aerofoil equipped with a trailing-edge flap hinged at its mid chord. The baseline case (grey curve) exhibits a good agreement for the whole time series. Although some deviations are evinced when flap deflections are added to the gross motion, the reason seems to have little connection with the accuracy of the model, and they are rather credited to geometrical differences. The aerofoil-flap geometry for CFD simulations was designed based on an experimental model from the literature (see §3.3). That model presents a gap at the hinge location, visible in Fig. 3.4(d), which could not be covered in CFD as it was done on the experimental setup. Flow in this region is therefore prone to separation at the leading edge of the flap if the angle of incidence is large for this element. Having clarified this, for cases undergoing

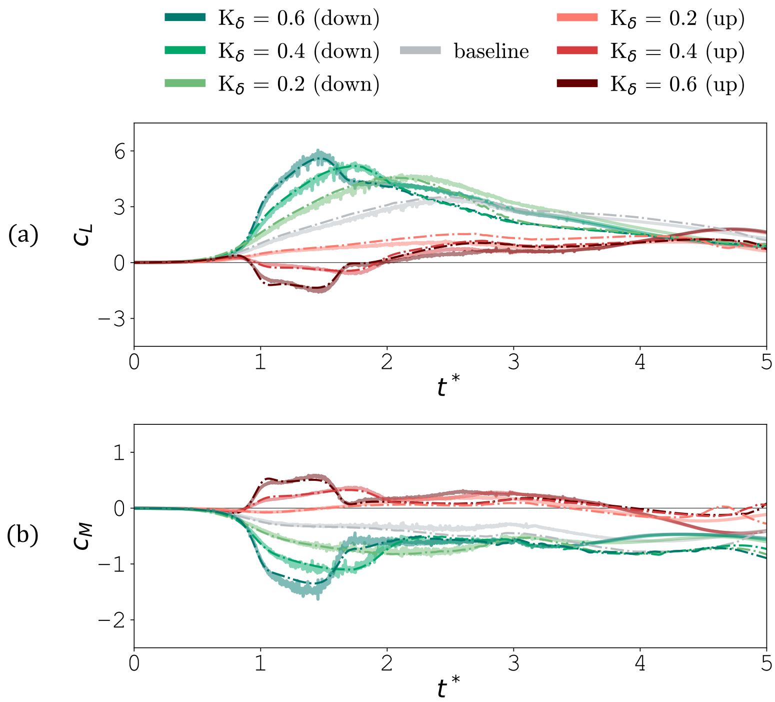

Figure 6.1: Aerodynamic coefficients time history for pitch-flap combined kinematics: (a) lift and (b) quarter-chord pitching moment from CFD (——) and MDVM (-·-·).

positive deflections (green curves) the flap experiences a high angle of attack at around $t^* = 2$, which is now owe to a combination of pitch and flap deflection. As a result, a Hinge Vortex (HV) forms at the leading edge of the flap and stays attached until approximately $t^* = 4$. Flow visualisation via spatial distribution of vorticity is shown in the top row of Fig. 6.2 for the case with $K_\delta = 0.4$, where the hinge vortex on the suction side, HV_S, is highlighted. Extra lift is expected during this period, and it is attributed to said vortex being adhered to the aerofoil. In consistency with the fact that MDVM does not model the hinge gap, and therefore not the hinge vortex either, low-order estimations of the lift coefficient, presented in Fig. 6.1(a), under-predict values obtained with CFD between $t^* = 2$ and $t^* = 4$. On the other hand, for the cases subjected to negative flap deflections (red curves), the right corner at the end of the fore element induces flow separation, that evolves over the pressure side of the flap, generating this section a negative lift (downwards force). The total lift coefficient for these cases is thus reduced between $t^* = 2$ and $t^* = 4$. Vorticity fields are shown in the top row of Fig. 6.3 for the case with $K_\delta = 0.4$,

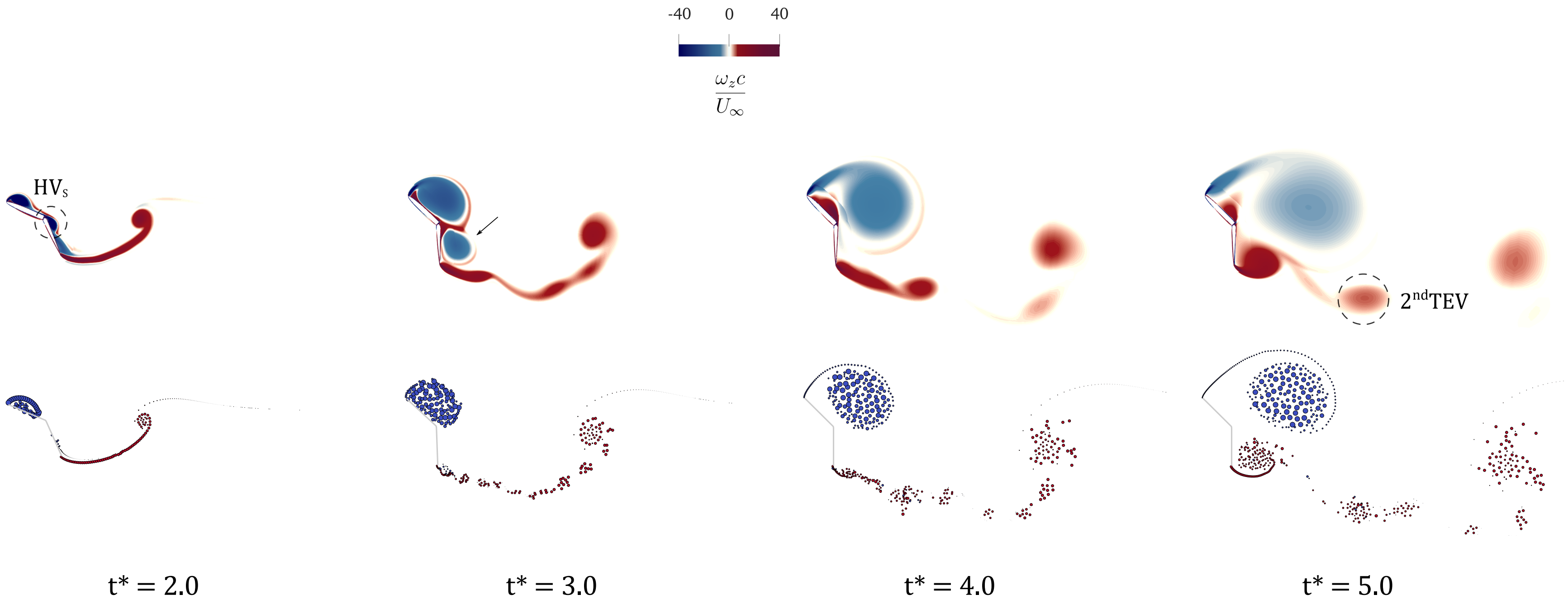

Figure 6.2: Spatial distribution of vorticity for positive flap deflection case with $K_\delta = 0.4$. Top is CFD, bottom is MDVM.

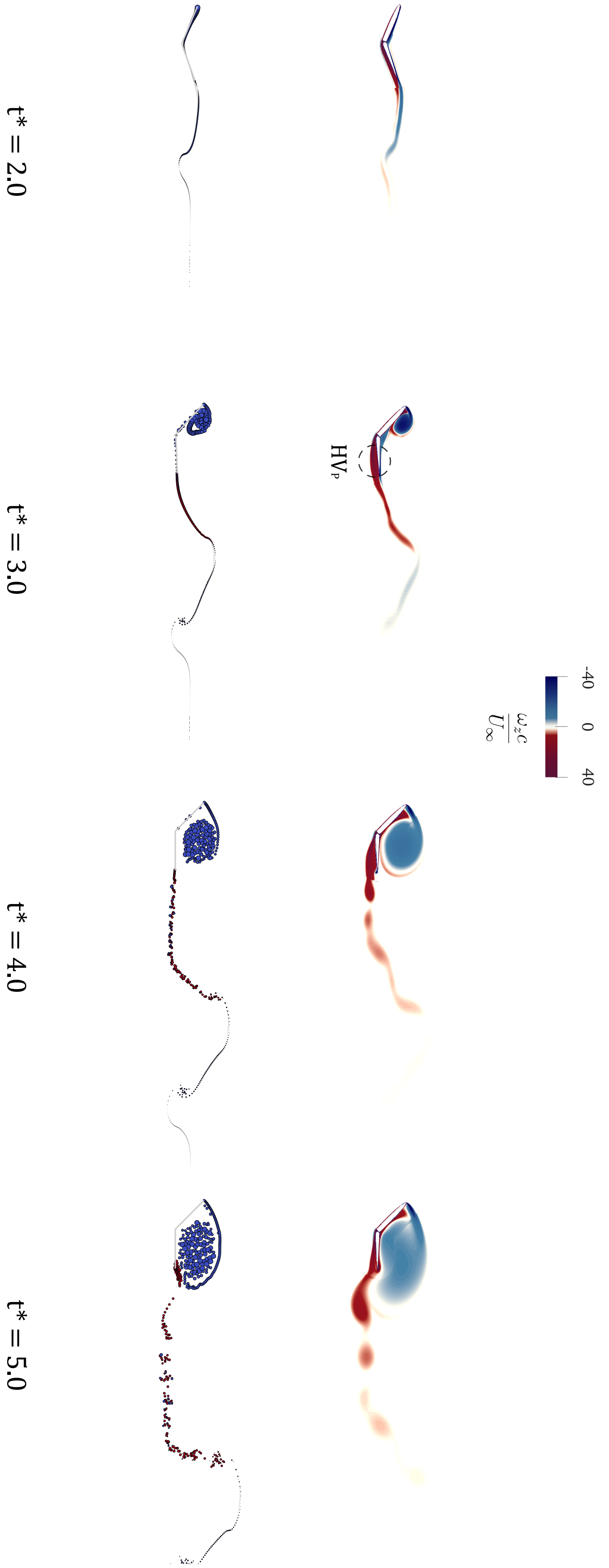

Figure 6.3: Spatial distribution of vorticity for negative flap deflection case with $K_\delta = 0.4$. Top is CFD, bottom is MDVM.

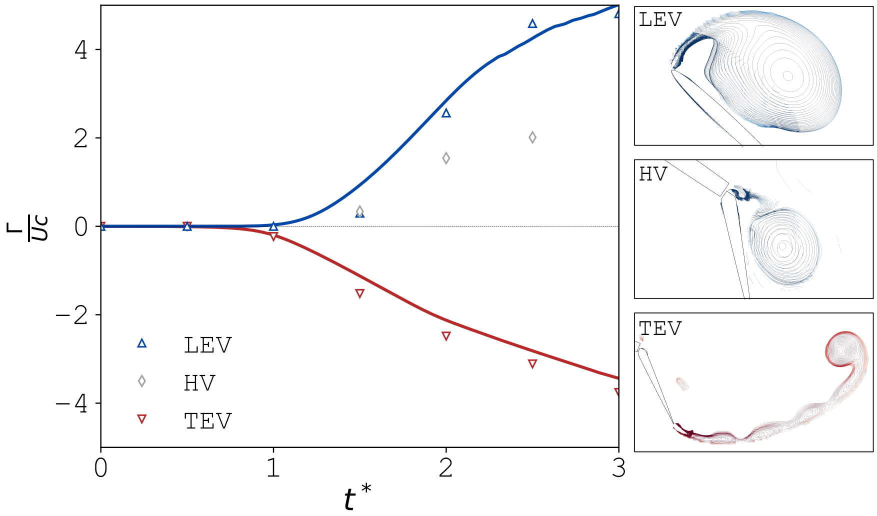

Figure 6.4: Normalised circulation of LEV, HV and TEV for positive flap deflection with $K_\delta = 0.4$. Curves represent MDVM predictions and markers CFD computations. Vorticity iso-contours defining each vortex shape are included to the right of the graph.

highlighting the separated flow region on the pressure side, HV_P. A negative vertical force applied behind the point at which moments are computed (the quarter chord here) produces a clockwise pitching moment, increasing the positive value of the coefficient for the period of time where separated flow is present, as observed in Fig. 6.1(*b*).

Hinge vortex

To give the observation of this vortex a more quantitative form, its strength is represented in Fig. 6.4 by means of the normalised total circulation extracted from CFD simulations. The strength of LEV and TEV has also been quantified and serves as a reference to ascertain the magnitude of the effect that a hinge vortex can have on aerodynamic loading. Past $t^* = 2$ the strength of the hinge vortex is around half that of the LEV, which could explain the substantial contribution to lift noticed in Fig. 6.1(*a*) for that case. Beyond this, the graph is useful to asses the precision with which the low-order model estimates the strength of vortices.

Aside from the strength, MDVM fully captures important traits of vortex dynamics such as: timing, size and position of vortices (excluding those formed at the hinge gap); slope of feeding shear layers; or wake patterns, like the shedding

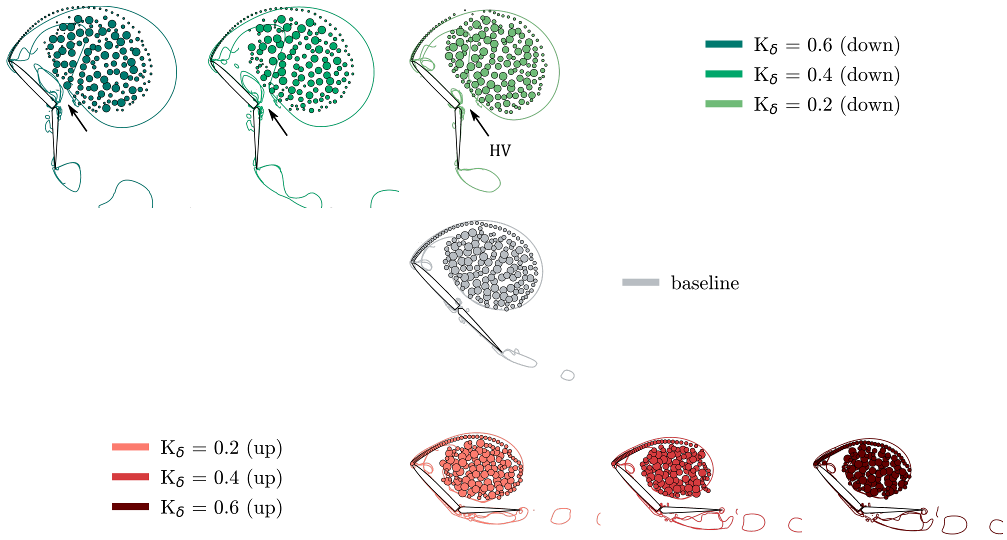

Figure 6.5: Shape comparison of LEV structure at $t^* = 4$ for all flap deflection rates. Vortex particles from MDVM are overlaid to vortex boundaries from CFD.

of two consecutive trailing-edge vortices. This is visible on the last snapshot in Fig. 6.2, and was previously reported in bats flight (Johansson et al., 2008) and computational studies with similar motions and deformations (Y. Liu et al., 2015). Visualisation of vorticity contours provided in Figs. 6.2 and 6.3 showcases the good agreement with CFD in modelling all these flow features.

The limitations imposed by the hinge gap to fully test the performance of MDVM are further examined in Fig. 6.5. For a late time of the vortex growth stage, $t^* = 4$, the shape of the fully-developed LEV is compared between MDVM and CFD simulations. The boundary of the vortex is defined in CFD as explained in Appendix B.2. Leading-edge vortex particles (trailing-edge particles are omitted here to present a clearer image) are overlaid to assess the correct size and position of the LEV are captured, as well as the slope of the feeding shear layer at the leading edge. The agreement in all these flow features is remarkable for the baseline case (grey) and the negative flap deflection cases (red). For the positive flap deflection cases (green) some dissimilarities arise. An emerging vortex structure is observed at the hinge gap, this time growing upstream. By the selected time instant, $t^* = 4$, the HV studied before has already been shed into the wake (see Fig. 6.2), but a

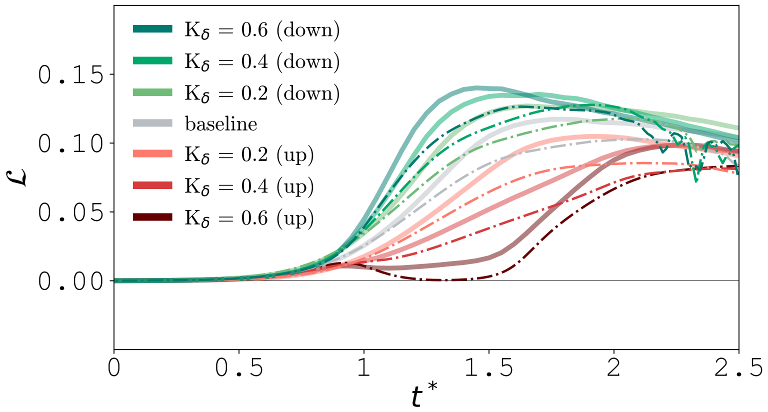

Figure 6.6: Leading-edge suction parameter time history for pitch-flap combined kinematics. Results are from CFD (——) and MDVM (-·-·).

new one has formed, apparently induced by the growing LEV itself. Because the LEV rotates clockwise, the momentum imparted on the fluid moving through the gap pulls it upstream (notice also the sharp corners at the trailing edge of the main aerofoil). The stronger the LEV the larger the imparted momentum, and subsequently the size of the newly growing HV, which in turn interacts with the LEV pushing it further downstream. This can explain the difference observed with MDVM, which is more accentuated for the fastest flap deflection case, corresponding to the strongest LEV as it will be discussed in §6.3.2.

Comments made regarding the appearance of hinge vortices do not infer the performance of MDVM deteriorates for positive flap deflections, they only aim to remark that direct comparison with CFD is meaningless at late stages of the LEV development. Overall, the low-order model presents a very good agreement in all aspects analysed, and for all cases, up to at least the onset of vortex formation, which it will be shown in §6.3.1 to happen between $t^* = 1$ and $t^* = 2$ for all cases. Since the attention is primarily focused on the formation process, it is believed HVs do not pose a hindrance in the following study.

6.2.2 Leading-edge suction

In §5.3.6, and in particular Fig. 5.13, the effect of Reynolds number on the leading-edge suction parameter was discussed. Estimations made by MDVM seemed to agree better with lower Reynolds numbers. The CFD simulations for the present chapter have been performed at $Re = 4 \cdot 10^4$. Thence, somewhat lower values of $\mathcal{L}$ are expected with the low-order model, and this is exhibited in Fig. 6.6. Despite the maximum values being slightly lower, the general trend is captured in all cases, which will suffice to achieve the goal of next section: to demonstrate the potential of camber morphing on altering vortex characteristics, including its formation time and strength. This will be accomplished by modulating the leading-edge suction parameter history through prescribed trailing-edge flexion.

6.3 Alteration of LEV development

Motion kinematics can be tailored to modify the timing of LEV occurrence through modulation of the leading-edge suction parameter. By superimposing heave motions on a pitching aerofoil Ramesh et al. (2018) and Suresh-Babu et al. (2022) demonstrated, through CFD and LOM simulations respectively, the viability of using the LESP concept to alter vortex formation. By the same token, morphing can be applied to affect the behaviour of vortices. The very nature of the variable-camber discrete-vortex model developed in Chapter 3 allows to input a broad spectrum of shape-defining parameters, which includes the length of the bending surface, the rate of deformation and the flexion amplitude. The study presented in following sections is centred around the effect of the second parameter on vortex formation time and strength.

6.3.1 Vortex formation time

Since the objective pursuit in this chapter is to alter vortex characteristics, the formation of an LEV has to be ensured before any action is taken to affect its behaviour. To design a baseline case which evinced a strong LEV, a rapid transient manoeuvre was prescribed on the aerofoil, and six different camber profiles were derived by actuating the trailing-edge flap as described in §6.2. In total, seven cases are generated to analyse the production of leading-edge vorticity. All of them share flow conditions, Re, radius of the profile at the leading edge, r_{LE}, instantaneous

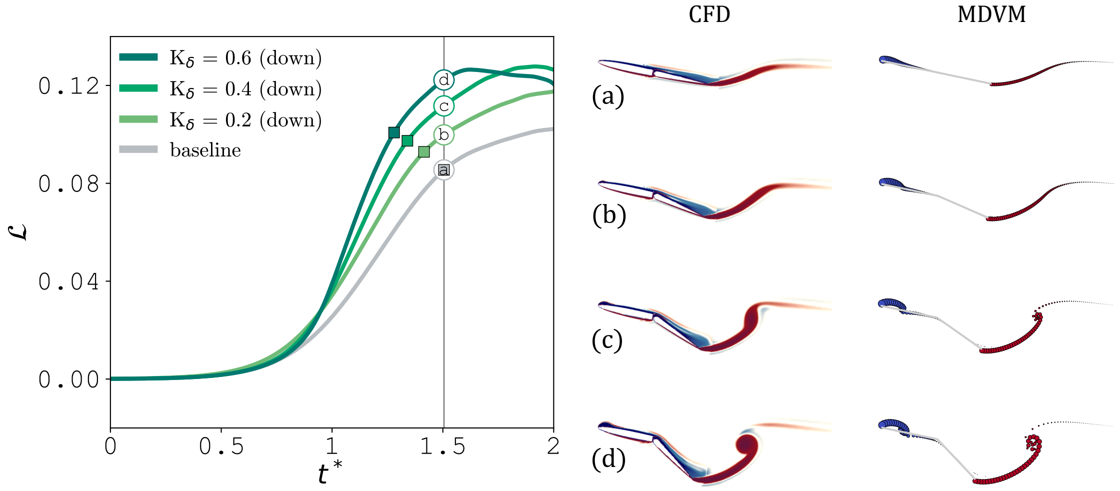

Figure 6.7: LEV formation triggered with positive trailing-edge flexion. Flow separation at the leading edge is marked with squares. A vertical line indicates the time instant at which CFD vorticity contours and MDVM vortex particles are shown for each case.

angle of attack, $\alpha(t)$, flexion ratio, $\frac{c_f}{c}$, flexion amplitude, δ_{max}, and start of actuation. In other words, the only difference between cases is therefore owed to the rate of flap deflection, K_δ. However, this parameter modifies the instantaneous value of flap deflection angle, $\delta(t)$, and by extension those of the effective angle of attack, $\alpha_{eff}(t)$, the camber ratio, $\frac{\eta_{max}(t)}{c}$, and the effective chord length, $c_{eff}(t)$.

Qualitative predictions of flow patterns induced by dynamic cambering, as noted by Zhao et al. (2010), suggest that positive camber in a wing is expected to produce higher values of leading-edge vorticity, and hence larger net forces than the uncambered counterpart, contrasting to the lower values expected for negatively cambered wings compared to the zero-camber case. Inspired by these observations, the effect of the different cambering profiles on the amount of vorticity produced at the leading edge is quantified here through the leading-edge suction parameter history, which for cases undergoing downwards flap deflections (positive camber) is presented in Fig. 6.7. The time instant of leading-edge flow separation has been calculated for each case based on the criterion introduced in Eq. (5.12), and marked with a coloured square over the corresponding curve. For the time period shown, the addition of positive camber is observed to increase the suction at the leading edge, the more the faster the flap motion. This is reasonable bearing in mind

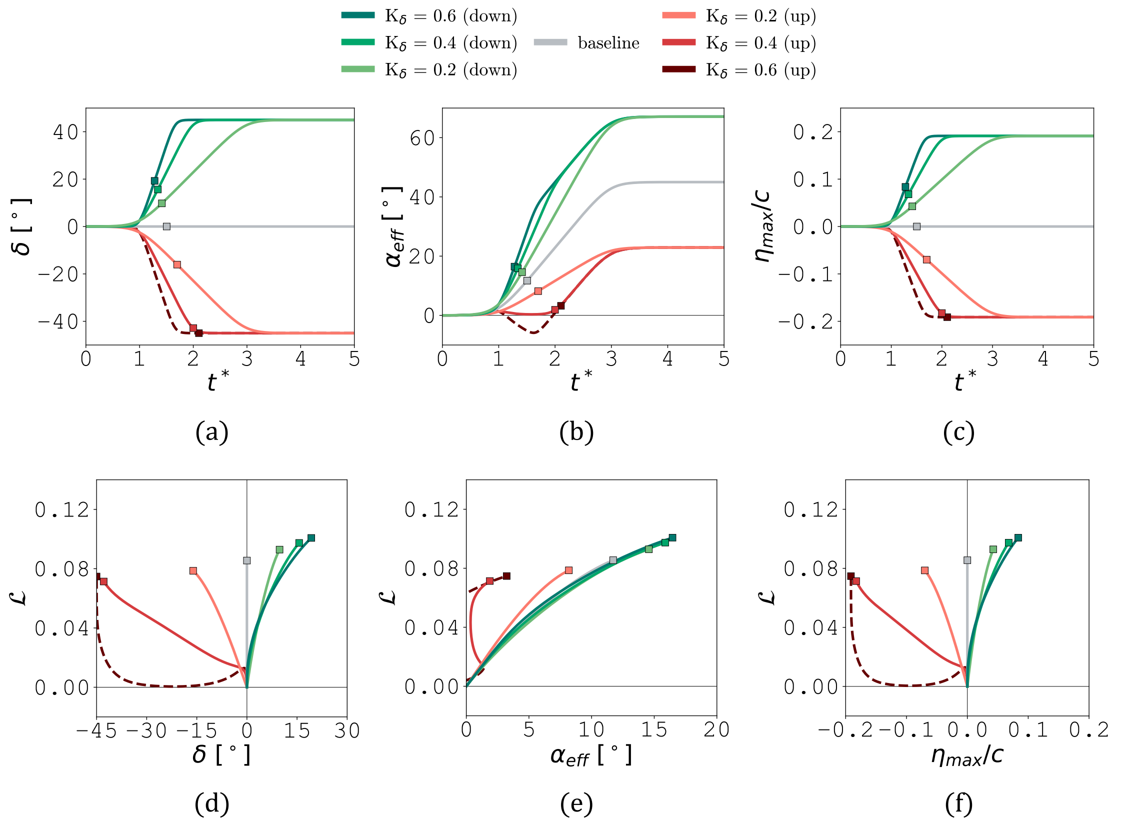

Figure 6.8: Morphing parameters (vs. time and vs. $\mathcal{L}$ respectively): (a, d) flap deflection angle, (b, e) effective angle of attack and (c, f) camber ratio. Squares mark the instant of flow separation.

that the instantaneous camber ratio, $\frac{\eta_{max}(t)}{c}$, will be higher for a larger value of K_δ until the flap ceases its motion (see Fig. 6.8c). It is also noticeable that for faster cases the flow separates earlier and after the aerofoil has accumulated a larger amount of suction (squares shifted up-leftwards).

In terms of flow topology, it can be visualised from the vorticity contours displayed to the right of Fig. 6.7 how positive cambering triggers the onset of LEV formation. For the time instant selected, $t^* = 1.5$, which corresponds to the timing of flow separation at the leading edge for the case where it occurs the latest (baseline case), an incipient LEV is appreciated for all positive flap deflection cases, in a more advanced stage the higher the rate of deflection (from top to bottom). The flow state is very well captured with MDVM, although the predicted size of the vortex being slightly bigger than CFD. This is presumably due to the Reynolds number effect, as commented in §6.2.2 and §5.3.6 in more detail.

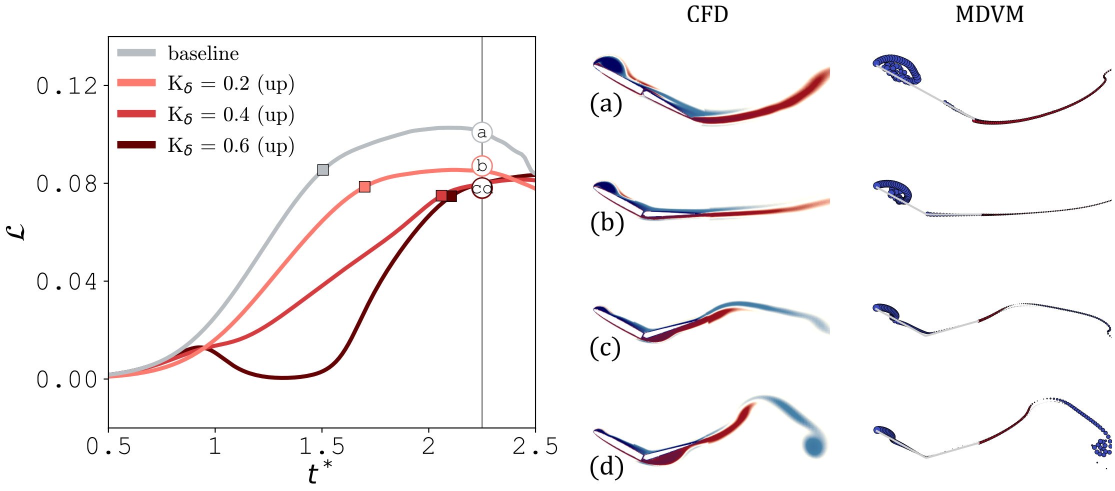

Figure 6.9: LEV formation delayed with negative trailing-edge flexion. Flow separation at the leading edge is marked with squares. A vertical line indicates the time instant at which CFD vorticity contours and MDVM vortex particles are shown for each case.

Contrary to the set of positive camber profiles, Fig. 6.9 showcases how a negative camber delays the occurrence of the leading-edge vortex. The opposite effect is now observed to what has been previously discussed: faster upwards motions of the flap result in larger negative values of the instantaneous flap deflection angle, $\delta(t)$ (see Fig. 6.8*a*), which accentuates the reduction in magnitude of $\mathcal{L}$. Flow separation at the leading edge is delayed in time, and undergone with lower amounts of suction the faster the flap actuation (squares shifted down-rightwards). It is interesting to look at the fastest case, where a drop in $\mathcal{L}$ is noticed at the beginning of the motion. This is due to the instantaneous effective angle of attack, $\alpha_{eff}(t)$, turning negative because the flap rotates sufficiently faster than the aerofoil pitches (see Fig. 6.8(*b*), where this specific case is represented by a dashed line).

Vorticity contours from CFD and vortex particles from MDVM, exhibited to the right of Fig. 6.9, confirm the findings just discussed. At the time instant selected for visualisation in this set of cases, $t^* = 2.25$, the LEV is seen to be already in an advanced stage for the baseline case, while it has barely formed for the fastest deflection case (again, from top to bottom). These results match the opening remarks in this section (Zhao et al., 2010).

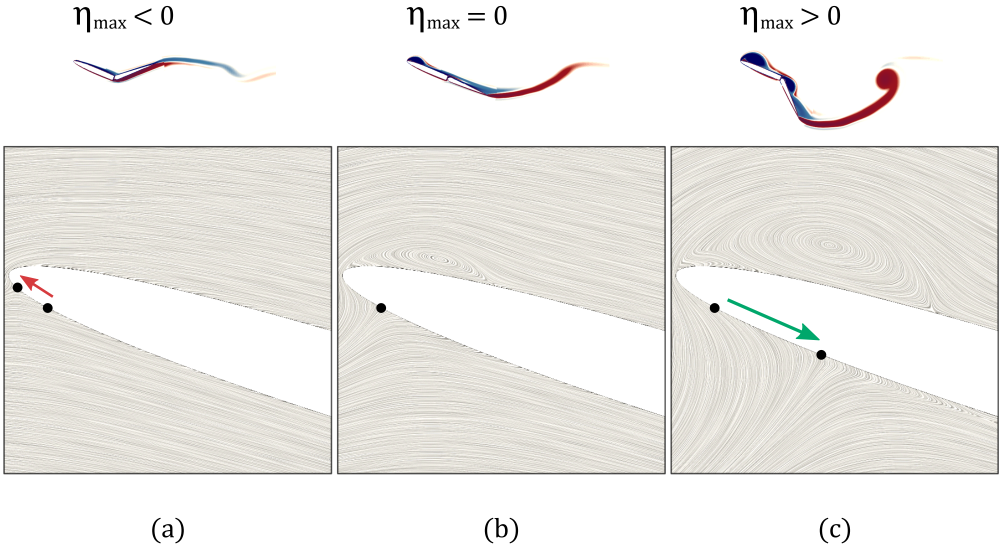

Figure 6.10: Stagnation point movement due to camber variations. Streamlines from CFD show the stage of LEV formation for: (*a*) negative camber, (*b*) no camber and (*c*) positive camber. Red and green arrows indicate the direction of motion.

The mathematical concept of stagnation point can help better understand the observed behaviour of $\mathcal{L}$ in Figs. 6.7 and 6.9. By definition, the local velocity of the fluid is zero at the stagnation point. Since $\mathcal{L}$ is correlated with the velocity at the leading edge, Eq. (5.4), its value becomes null when the stagnation point coincides with the geometric leading edge. Because $\mathcal{L}$ is a measure of the suction in that point, it will also be zero. When the stagnation point is moved away from the leading edge the flow is forced to travel upstream and around the edge, giving rise to a low-pressure region which generates suction force. The longer the distance to travel the larger the magnitude of the force. Flap deflections modify the effective angle of attack of the aerofoil, affecting the location of the stagnation point. Similar to a pitch-up motion, positive deflections increase the effective angle of attack, resulting in the stagnation point moving aftwards (over the pressure side if $\alpha_{eff} > 0$, and over the suction side if $\alpha_{eff} < 0$). This movement is illustrated in Fig. 6.10(*c*) through streamlines extracted from CFD simulations. A green arrow indicates the motion with respect to the baseline case, where no flap deflections are superimposed. Having moved the stagnation point away from the leading edge, the amount of suction will be larger than for the baseline case, reason why the curves for positive camber cases in Fig. 6.7 exhibit larger values of $\mathcal{L}$. Conversely, the stagnation point is moved forwards with negative flap deflections, getting closer to the leading edge and thus reducing the amount of suction. This is depicted in Fig. 6.10(a), where the direction of motion is signalled this time with a red arrow. Accordingly, curves for negative camber cases in Fig. 6.9 show lower values of $\mathcal{L}$ than the baseline case. Similar to how Ramesh (2020) expressed the location of the stagnation point in terms of A_0, it would be possible to derive an equivalent expression for arbitrary flap motions, as suggested in §7.2. This would allow a quantitative analysis to be carried out.

Flow control strategies based on the time-varying camber idea involve to knowingly manipulating the production of leading-edge vorticity by tailoring the shape of the camber line. It therefore seems logical to seek a mathematical relation between A_0 and parameters affecting the camber. Such an expression would enable the separation of the effects of each contributing variable, and quantitatively ascertain their capacity to affect the formation of LEVs. For the study of transient camber variations (non-harmonic), instantaneous shape-defining parameters seem better suited: effective angle of attack, α_{eff}; effective chord length, c_{eff}; camber ratio, $\frac{\eta_{max}}{c}$; and deflected angle, δ. The expression sought can then be attained upon integration of Eq. (3.22) as indicated in Eq. (3.25a). After some rearrangement and recurring to variable transformations, most of the integrals involved are easily computable for the specific case of $\frac{c_f}{c} = 0.5$, and a final expression for A_0 can be derived in a semi-analytical form:

$$A_0 = \left\{ \begin{array}{l} A_{0,w} \\ + \sin(\alpha_{eff}) \\ -2K_h \cos(\alpha_{eff}) \\ +K_\alpha \Big[\frac{c_{eff}}{c} - 2\frac{c_{pvt}}{c} \cos\left(\frac{\delta}{2}\right) \Big] \\ +K_\delta \left[\frac{1}{2}\frac{c_{eff}}{c} + 2\left(\frac{1}{2} - \frac{1}{\pi}\right) \left(4\frac{\eta_{max}}{c} \tan\left(\frac{\delta}{2}\right) - \frac{c_{eff}}{c} \frac{1}{\cos^2\left(\frac{\delta}{2}\right)} \right) \right] \end{array} \right. . \tag{6.1}$$

There is no analytical form for vortices-induced effects, $A_{0,w}$, which are history-dependant, and they have to be treated numerically. The above expression could be further simplified to depend on only the instantaneous pitch angle, $\alpha(t)$, and flap deflection angle, $\delta(t)$, upon substitution of α_{eff} from Eqs. (3.9) and (3.10), c_{eff} from Eq. (3.8), and η_{max} from Eq. (3.13). Coupling of parameters in some terms makes it difficult *a priori* to assess the exact effect of each term on the leading-edge suction. This is analysed in detailed in the following section.

6.3.2 Vortex strength

In Chapter 5 it was shown that the strength of vortex particles entering the flow field at the separation point, in this case located at the leading edge, is directly proportional to the leading-edge suction squared, Eq. (5.6). The dependency of this parameter on shape-defining variables is given by Eq. (6.1) for the case of an aerofoil-flap configuration where the length of the flap is half the total chord length of the aerofoil. The effect of different parameters on the vorticity feeding rate, and thus the strength of the LEV, can therefore be deduced by combining both equations.

The instantaneous strength and growth rate of LEVs are analysed in Fig. 6.11 for the seven cases. The normalised vortex circulation is presented against non-dimensional time of vortex growth, t^*_{LEV}, defined as units of time after flow separates at the leading edge for that case. This variable has been introduced to allow direct comparison between cases. By bringing all curves to the same origin of times, the state of the vortex at any instant during the growth phase can be consistently compared. A distinction has been made between the period of time when both, aerofoil's motion and vortex dynamics, contribute to the LEV growth (continuous curves), and the period following the end of the motion (dashed curves), which is indicated by a diamond for each case. To study the evolution of leading-edge vorticity produced, and hence the vortex strength, it is useful to observe the value of flap deflection at the time instant of flow separation, since it plays a crucial role in the post-separation behaviour. These values are obtained for each case from the coloured squares in Fig. 6.8(a). For positive flap deflection cases, the faster the

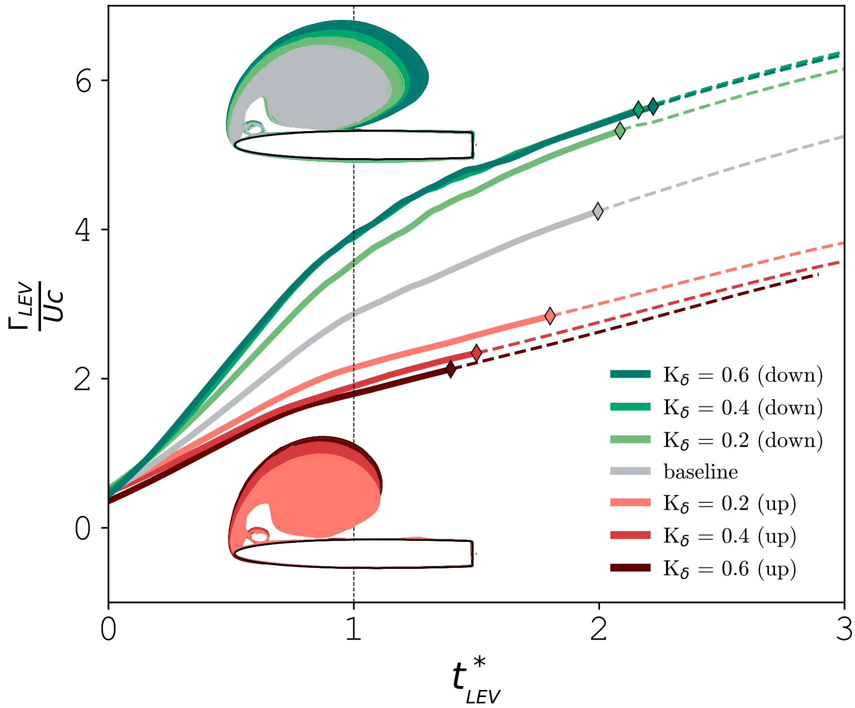

Figure 6.11: Leading-edge vortex strength: normalised vortex circulation vs. non-dimensional time of vortex growth, during aerofoil's motion (—) and after the motion has ceased (- - -). The end of the motion is marked for each case (◇). Inset figures compare the different shapes of the LEV one unit of time after formation.

motion the higher is δ at separation. And for negative deflections, δ will increase in negative value with the rate of deflection. The fastest upwards deflection case (dashed curves in Fig. 6.8) is omitted for the following analyses due to its particular beginning. Having a look now at the other camber-defining parameters involved in Eq. (6.1): the camber ratio, $\frac{\eta_{max}}{c}$, proportional to the deflection angle, δ, and preserving its sign (see Eq. (3.13)), will have at separation a larger value for faster positive deflections; as for the effective angle of attack, α_{eff}, since the pitch angle is the same for all cases, it will follow similar trends to δ.

Upon evaluation of Eq. (6.1) during the first stage, indicated in Fig. 6.11 with continuous curves, the behaviour of each term with increasing values of δ can be estimated as follows: 1^{st}) it needs to be calculated numerically. 2^{nd}) it increases with δ. 3^{rd}) it is null, since no plunge motion has been considered in this study. 4^{th}) the first term inside the parenthesis decreases with δ, meaning that larger values will increase less A_0; the second term also decreases with δ, but having negative sign means that larger values of δ will reduce less A_0. Since the first term scales as $\mathcal{O}(\sqrt{\cos\delta})$ and the second term as $\mathcal{O}(\cos\delta)$, the later contribution has a greater effect, and therefore the whole term increases with δ. 5^{th}) the first term inside the parenthesis decreases with δ; the second one increases; and the third one is made up of a component which increases and a component which decreases. Since the three terms scale, respectively, as $\mathcal{O}(\sqrt{\cos\delta})$, $\mathcal{O}(\sin\delta\tan\delta)$ and $\mathcal{O}(\sqrt{\cos\delta}\cos^{-2}\delta)$, the second term has a greater effect. The contribution of this term to A_0 then increases with δ. In addition, the constant multiplying outside the parenthesis, K_δ, further accentuates the difference between cases. In short, all terms are either independent of δ or increase with it. As remarked in the previous paragraph, the value of δ at separation increases with the rate of deflection. Thus, the faster the flap deflection the higher the initial δ and also the rate of change. This means that A_0 will grow faster, and so will the vortex strength (greater slope in the graph). As for the second stage, indicated in Fig. 6.11 with dashed curves, the motion has ceased already and all cases have reached the same maximum value of δ. The only contribution to A_0 that differs between cases is then due to vortices-induced velocities, $A_{0,w}$. Because this term is expected to be very small compared to the second term in Eq. (6.1), all cases evolve with a very similar slope, meaning the growth rate is nearly the same (parallel curves in the graph).

The shape of the LEV at one unit of non-dimensional time after formation is compared between cases through the inset figures in Fig. 6.11, where vortex-delimiting contours extracted from CFD are overlapped. Shown is only the aerofoil's fore element. It is observed that the vortex size at the selected time is between $\frac{c}{4}$ and $\frac{c}{2}$ for all cases. In consistency with the foregoing analytical discussion on the vortex strength, increasing the positive camber (downwards flap deflections) strengthens the vortex, which therefore grows in size. The faster the deflection the bigger the LEV. It is interesting to note however, that for negative cambers (upwards flap deflections) the vortex extends for all three cases the same length along the suction side of the aerofoil, but the stronger it is the closer to the surface it stays.

Drawn from investigations carried out by Feszty et al. (2004) on rotary-wings, an actuator at the trailing edge, like a flap, could only mitigate the effects of dynamic stall, but not to delay the process. Later studies endorsed the claim observing that actuation of a trailing-edge flap did not affect the timing of DSVs initiation on those cases tested, although it did alter their strength (Gerontakos & Lee, 2006, 2008; Samara & Johnson, 2020). The low-pressure signature of the vortex was reduced with upwards flap deflections, which means the vortex weakened. With downwards deflections the vortex exhibited larger in its transverse direction, indicative of a stronger vortex. Flow conditions (higher Reynolds number), model geometry (thicker aerofoil and shorter flap) and kinematics (different profile, lower rate of motion and deflection) on these works differ from the ones in the current study. This could be the reason why the vortex formation time was not affected in those investigations, whereas it has been demonstrated in §6.3.1 that LEV formation can indeed be affected. Still, findings about the qualitative behaviour of vortex strength are in agreement with the results shown in Fig. 6.11: negative trailing-edge flexion (upwards) reduces the strength of LEVs, and the opposite happens for positive flexion (downwards). Recent research on deformable flapping plates at low Reynolds numbers (C. Li et al., 2015), flow conditions that are closer to the ones analysed here, supports the relations observed between variations in camber and their effect on the strength of the vortex. Studies of camber-morphing wings show that at low speeds, or at high pitch angles, increased camber is systematically beneficial (Cheney et al., 2021). To establish a link with the results from Fig. 6.11, it would not be inconsistent to think that a stronger LEV resulting from larger values of positive camber could help provide the extra lift required in these demanding situations.

6.4 Summary

In this chapter morphing and vortex modelling have been combined with a threefold objective: to assess the performance of the low-order morphing model in more complex scenarios than those studied so far, where the shape of the camber line varies in time and vorticity is produced at the leading edge; to illustrate the capacity of trailing-edge flexion in altering vortex features, like formation time and strength, through modulation of the leading-edge suction parameter history; to provide fundamental insight into this correlation. The expectation is to turn the acquired knowledge from mathematical relations, between morphing-defining parameters and evolution of flow variables, into potential strategies for flow control to enhance biologically-inspired locomotion.

To achieve these goals, a rapid transient manoeuvre has been prescribed on a NACA 0006 aerofoil hinged at the mid chord, to ensure the formation of LEVs. Six different camber profiles have been generated from this baseline case by actuating the trailing-edge flap with different parameters. This set of cases has enabled the examination of the effect of camber modifications on the production of leading-edge vorticity, and hence the vortex formation time and strength.

The occurrence of a hinge vortex has been noticed in CFD simulations due to a gap in that region, which is not modelled in MDVM. This has led to some differences in the aerodynamic coefficients at late stages of the vortex growth. However, since the focus has been on the vortex formation, said hinge vortices have not posed a hindrance in the analysis.

It has been shown that suitable alterations of camber parameters drive the occurrence of LEV, triggering or delaying its formation. The amount of vorticity accumulated into the vortex, this is its strength, can also be affected.

A semi-analytical expression has been derived for the specific case of $\frac{c_f}{c} = 0.5$ which relates the leading-edge suction parameter to the camber-defining variables. This has been done by integrating A_0 from unsteady thin-aerofoil theory, defined in terms of the downwash, where all the variables affecting the camber are included. The resulting expression has allowed a fundamental discussion on the behaviour of LEV strength.

Some progress has been made on the use of physics-based models, like MDVM, to explore the unsteady flow control capability of dynamic cambering. The number of vortex particles in the fluid was around 300 for the cases shown in this chapter, and it took ≈ 3 seconds in a personal laptop to follow the evolution of the fluid from $t^* = 0$ to $t^* = 5$. Besides providing nearly-immediate results (making the model useful as an engineering tool), it enables a fundamental understanding of the relation between dynamic camber variations and unsteady flow response. These results are encouraging for the design of control strategies for vortex flows based on the camber morphing practice.

This dissertation is concluded in the next chapter, suggesting related research questions that could be addressed in future investigations.

The Road goes ever on and on
Out from the door where it began.
Now far ahead the Road has gone,
Let others follow it who can!

— J.R.R. Tolkien

7

CONCLUSIONS AND FUTURE WORK

What is learnt is a handful of sand, whereas the unknown is the size of the world, goes a Tamil proverb. With no more time ahead, this dissertation came to an end. A brief summary of the whole research carried out is given in §7.1, and some research avenues are recommended in §7.2 to be the focus of future investigations, hoping to resume this work where it is left now.

7.1 Concluding remarks

The main goal of Chapter 3 has been the development of a physics-based low-order model to simulate unsteady flow response to arbitrarily large variations of the camber. For this purpose, an adapted potential-flow theory for unsteady aerofoils has been combined with numerical methods using discrete-vortex elements. To extend the range of applicability of UTAT, conceived for small disturbances, the no-through-flow boundary condition has been enforced over a chord line that is allowed to vary with flap deflections. This has enabled large-amplitude deflections to be accurately modelled. The outcome: a low-computational cost physics-based tool, capable of modelling unsteady flows past deforming foils in the order of seconds on a personal laptop. This is a potential tool to explore the capability of trailing-edge flexion in altering vortex characteristics.

The aim in Chapter 4 has been to derive simple analytical forms of all Fourier coefficients for the classic aerodynamic problem of a hinged flat plate oscillating harmonically. To achieve this, an expression for the vortex sheet strength has been adapted from Theodorsen's to UTAT's framework, to allow comparison with the bound vortex sheet strength from UTAT. Previous treatment involved the approximation of some logarithmic terms as a Fourier series, which has been done for the specific case of a flap hinged at the mid-chord. The resultant analytical expressions for the Fourier coefficients serve to validate numerical codes. They can also be used to predict unsteady pressure distributions and stagnation point location for this fundamental aerodynamic problem.

The motivation of Chapter 5 came from the need to address the inaccuracy of current vortex models in predicting the post-separation evolution of flow features. To solve this, an alternative way to estimate the rate at which leading-edge vorticity is produced in vortex methods has been introduced. Expressed now in terms of the velocity at the outer edge of the feeding shear layer, the strength of vortex particles is proportional to the leading-edge suction parameter squared, and inversely proportional to the radius at the leading edge. This allows us to include the effect of thickness in the computation, and to properly capture the evolution of leading-edge suction during vortex formation. As a result, modelling the reattachment process of separated vortex sheets became possible, avoiding the break off observed in previous models.

Finally, the intention in Chapter 6 has been to explore the capability of camber variations in altering the production of leading-edge vorticity, and hence vortex characteristics like the formation time and strength of LEVs. For this purpose, the outcomes of previous chapters have been combined. This has enabled assessment of the performance of the low-order model in complex scenarios which involve both, temporal variations of the camber line and production of vorticity at the leading edge. It has been demonstrated how the occurrence of an LEV can be triggered or delayed in time through suitable variations of the camber line. The strength of the vortex, or amount of vorticity accumulated into it, can also be affected. A semi-analytical expression which relates the leading-edge suction parameter with camber-defining variables has provided fundamental understanding of the vortex formation process.

7.2 Suggested avenues of research

Below are recommended lines of research where some progress has already been made, which are deemed more promising, or that form the logical continuation of each chapter in this dissertation.

7.2.1 Extensions to the discrete-vortex model

Personally, the most interesting paths to take Chapter 3 forwards are:

Compliant trailing edge

Cutting-edge technologies in aerospace structures, materials and manufacturing have now pushed the limits of design far beyond the traditional conception of rigid wings, and even passive flexibility, offering diverse solutions to exploit the camber morphing concept. Hinge-less architectures like the belt-rib (Campanile & Sachau, 2000), the fish bone geometry (Woods & Friswell, 2012), or other compliant structures (Moulton & Hunsaker, 2021), have increase the achievable level of compliance, allowing for smooth and continuous large camber variations to be created (around 18% camber ratio reported in Woods et al. (2015)). This has an added benefit over conventional trailing-edge flaps, where the adverse pressure gradient due to the camber slope discontinuity at the hinge point may trigger flow separation in this region. Thus, a higher degree of control with the morphing low-order model is to be pursued.

Trying to implement the idea of compliance into MDVM using simple maths, an elliptic flap was my first idea. However, the 90° value of the camber slope at the trailing edge could more easily prompt separation in this region than for the hinged flap. Having discarded this approach, I considered a parabolic flap. There is a well detailed formulation for this in Hunsaker et al. (2019). The parabolic flap has been used in other research papers, and its effectiveness has been proven to outperform that of the traditional flap, requiring a lower deflection to produce

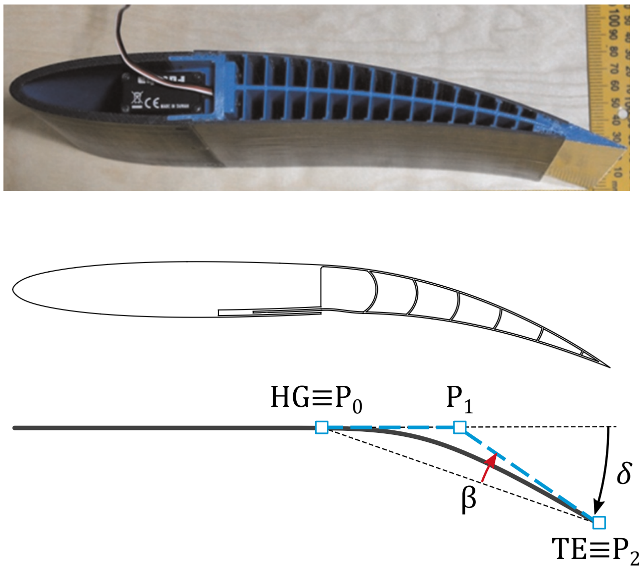

Figure 7.1: Bio-inspired compliant trailing edge: (top) Fish Bone Active Camber concept, reproduced from Woods et al. (2014) with permission; (centre) Aerofoil Recambering Compliant System geometry, reproduced from Moulton and Hunsaker (2021) with permission; (bottom) quadratic Bézier curve approach. Drawn in blue is the control polygon defining the curve, $P_0 - P_1 - P_2$. The control parameter, β, is also indicated.

the same lift increment. However, if the goal is to extend the scope of the control strategy applied, one would ideally handle a camber line with a higher degree of morphing. A promising alternative, due to the degree of manipulation offered, is the use of Bézier curves to define the flap's camber line, as illustrated by the schematic in Fig. 7.1. These polynomial curves are very user friendly, they allow modelling of more complex shapes by adding control points and different weights to each control point if desired (Farin, 2014). More interesting yet, the derivative of a Bézier curve is given by another Bézier curve of degree $n - 1$. Bearing in mind that adapting the current model for these curves to be used, would only require information on the camber distribution and its derivative, the said property should make the implementation much easier. As a first attempt, a quadratic curve $n = 2$ could be pursued. This way, two of the three control points are directly obtained in the desired frame of reference, since the coordinates of the hinge and the trailing edge are already known. As for the third point, its position would be determined by the tangents to both edges. If continuity of the camber slope at the hinge point is sought, the first tangent is predetermined by the direction of the fore-element symmetry line. This provides an extra control parameter: the angle formed between the line connecting the hinge and trailing edge, and the line linking the last two control points, β (see Fig. 7.1 for a detailed definition of the curve). For a value of $\beta = 0$ the rigid flap is retrieved, whereas for $\beta = \delta$ the parabolic flap is obtained. This could be used to evaluate the implementation with available data in the literature (Hunsaker et al., 2019). Having developed the required maths to get to this point, an added difficulty was found in mapping points along the curve with their corresponding point over the discretised chord line. Different points are obtained along a Bézier curve in parametric form by increasing the value of the parametrisation variable, t, as expressed in:

$$\begin{aligned} x(t) &= \xi_{hg}\Big((1-t)^2 + 2t(1-t)\Big) + c_f \tfrac{\sin\beta}{\sin(\delta+\beta)} \cos\alpha_\delta 2t(1-t) + c_{eff} t^2 \quad , \\ y(t) &= \eta_{hg}\Big((1-t)^2 + 2t(1-t)\Big) + c_f \tfrac{\sin\beta}{\sin(\delta+\beta)} \sin\alpha_\delta 2t(1-t) \quad . \end{aligned} \tag{7.1}$$

However, there is no fixed increment for this variable, t, that provides all the points wanted. To get those points matching with the chord line discretisation, chordwise coordinates need to be replaced in the expression of the Bézier curve, so that a value for the variable t is obtained, which is then used to provide the normal coordinate or camber. A plausible alternative might be the use of Bézier curves in their non-parametric form (Sanchez-Reyes & Chacón, 2018). However, more progress has to be made in this direction to assess its feasibility.

Chordwise flexibility

By coupling the discrete-vortex model with a structural model, aeroelasticity effects would be taken into account. This would give MDVM the opportunity to be exploited for the simulation of problems involving fluid-structure interactions. It has been demonstrated qualitatively in §3.4 the great performance of MDVM in capturing wake patterns. There exist several vortex identification methods (Graftieaux et al., 2001; Huang & Green, 2015) that could be implemented to easily locate the core of wake vortices in the model. This would open the doors to explore a multitude of current interest research topics in the field of flapping-based propulsion, where engineering is seeing great progress with the development of Autonomous Underwater Vehicles (AUV). Chordwise flexibility has a determinant role in optimal thrust production, efficiency enhancement (Han et al., 2022) and wake stabilisation among other effects, having been shown to inhibit the symmetry breaking of propulsive wakes (Marais et al., 2012).

7.2.2 Generalisation of analytical expressions

Fourier coefficients

The analytical expressions presented in Chapter 4 have been derived only for the aerodynamic problem of Theodorsen and the specific case of a flap whose length is half the total chord. Extension to other flap lengths has not been done due to a lack of time, combined with the mathematical difficulty encountered in approximating logarithmic terms as Fourier series. It would be interesting to resume those efforts, in order to obtain expressions of the Fourier coefficients which are of general application, regardless of the flap length. Furthermore, other classical aerodynamic problems involving non-harmonic motions of a flap could be studied to derive equivalent expressions.

Unsteady pressure distribution and stagnation point

From the analytical forms of Fourier coefficients derived in that chapter, obtaining an expression for the unsteady pressure distribution over the aerofoil, as well as for the location of the stagnation point, should be straightforward following guidelines by Ramesh (2020), who derived these expressions for Theodorsen's problem without flap actuation.

7.2.3 Variations of shear-layer thickness

The onset of leading-edge flow separation is a very active matter of research within the field of unsteady aerodynamics. Multiple attempts are being made to find a universally applicable criterion to determine the onset of separation. Following recent findings of other researchers about the effect of Reynolds number on the post-separation evolution of the leading-edge suction parameter (Narsipur, 2022), the assessment of the real scope in which the criterion proposed in Chapter 5 is valid deserves further exploration. The following direction of research is suggested: since the thickness of the feeding shear layer is determinant in calculating the flux of vorticity, and its magnitude is expected to vary with the Reynolds number, efforts could be addressed towards including this parameter in the computation of leading-edge vorticity shedding, perhaps through the velocity at the inner edge of the shear layer, which has been neglected in the current model.

7.2.4 Exploration of camber morphing capabilities

With the low-order model extensively validated, and some of its capabilities already demonstrated, there are many interesting challenges for which MDVM could be applied. A few of them are summarised next.

Flow reattachment modulation

Similarly to how the leading-edge suction parameter has been used to modulate vortex formation time and strength in Chapter 6, another interesting unsteady flow feature to look at is the reattachment phase of the separated shear layer.

Closed-loop control design

Closed-loop control strategies with discrete-vortex models as plant have been designed for different objectives. For example, Sedky et al. (2020) investigated the impact of the closed-loop control on gust mitigation, seeking to regulate lift during a gust encounter with pitching kinematics as the input. Stimulated by that research, the morphing discrete-vortex model developed in this work could be used to design a closed-loop control with camber variation as the input and the formation time or desired strength of the LEV as the objective.

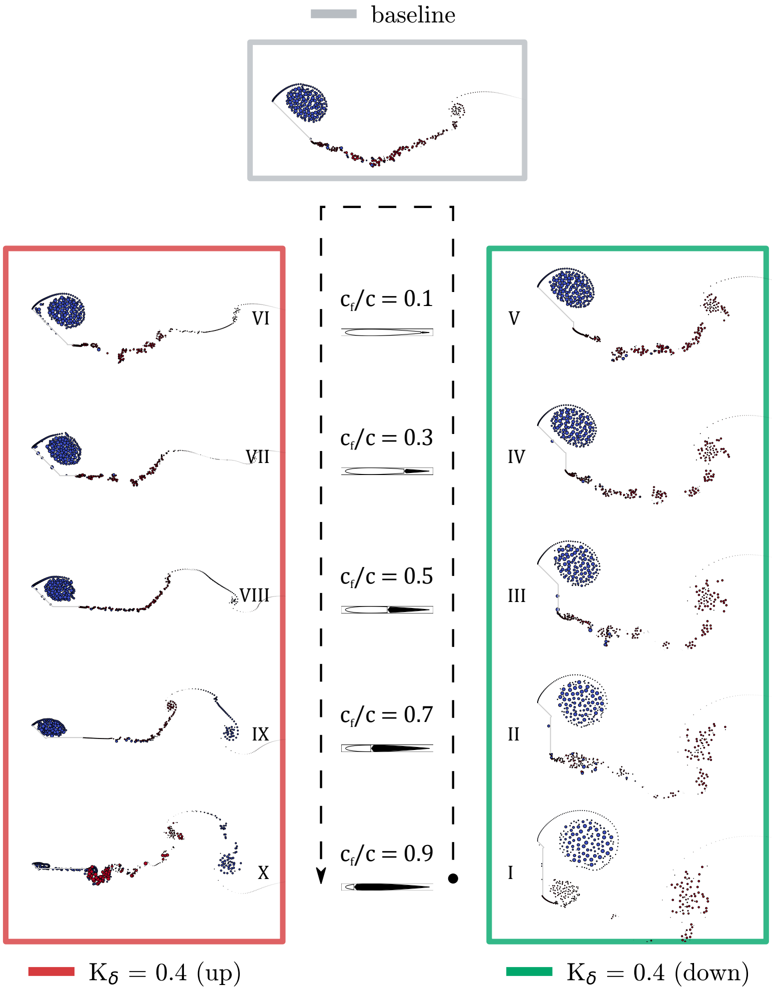

Figure 7.2: Alteration of LEV formation time with various combinations of flexion ratio and flexion rate. Distribution of vortex particles is shown for all cases at the same time instant during vortex growth. A dashed line traces the order in which the LEV forms.

Flexion ratio effect

Finally, the effect of flexion ratio, $\frac{c_f}{c}$, could be further explored as a continuation of the work presented in Chapter 6, where results shown were for $\frac{c_f}{c} = 0.5$. As a proof of concept, preliminary results of the notable effect this parameter has on the formation of LEVs are displayed in Fig. 7.2. For the same pitching motion, two different flap deflection profiles are prescribed (downwards and its equivalent upwards), and five different values of the flexion ratio are compared. The distribution of vortex particles shows a remarkable difference in LEV size, and hence in vortex strength, attainable with variations of the length deflected.

Appendices

Time is a sort of river of passing events, and strong is its current; no sooner is a thing brought to sight than it is swept by and another takes its place, and this too will be swept away.

— Marcus Aurelius

A

Low-order model post-processing

A.1 Scaling vorticity plots

PLOTS of vorticity from low-order simulations can be post-processed to aid identifying regions in the flow field with higher concentrations of vorticity, like vortices. The strength of discrete elements is normalised with the circulation value of the strongest particle in the flow field for that specific simulation, excluding the starting vortex (because of its theoretically infinite value). The strongest particle will then have assigned a non-dimensional vorticity value of 1 or -1 (depending on its sense of rotation). Consequently, the particles in the flow field have normalised vorticity in the bounds $[-1,1]$. With these bounds established, the radii of vortex particles is defined with the square of the vorticity, in order to make the distinction easier between very strong and very weak particles, since a parabolic distribution accentuates these differences. To visualise this, the vorticity plot from a simulation of a foil undergoing harmonic trailing-edge flexion is shown in Fig. A.1. This case has been chosen because the generated wake pattern of alternate vortices illustrates nicely how those point vortices located close to the core of a vortex are much bigger than those in between vortex pairs. Lines in the background represent limits of each vortex according to CFD results.

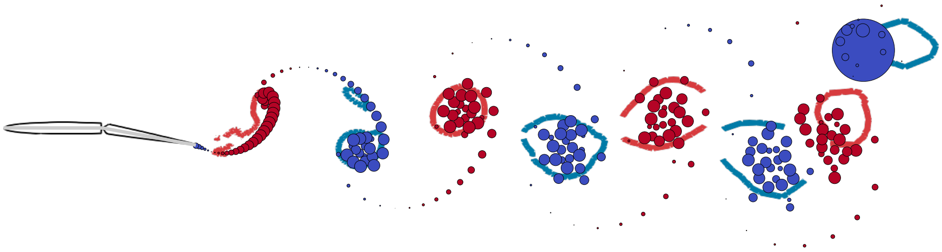

Figure A.1: Identification of vortices in the LOM through the biggest particles in the flow field, which represent the highest concentrations of vorticity. Q contours used to delimit vortices in CFD (red and blue lines) are overlaid for comparison.

It is important to emphasise that the process of vorticity scaling presented in this appendix has only visual purposes, and that the radii used to compute mutual interactions between particles through Eq. (3.27) is not modified. Also, note that visualisation from different simulations cannot be directly compared due to the per-solution normalisation (it can vary dramatically depending on the unsteadiness of each particular case).

The past remains hidden in clouds of memory.

— Matsuo Bashō

B

CFD model post-processing

REFERENCE data is necessary to validate the performance of mathematical models, and the accuracy on estimating diverse flow quantities can be assessed with this data. This appendix describes post-processing techniques developed to extract variables of interest from CFD simulations, used to characterise vortex dynamics in Chapter 5. These are: the edge velocity of a shear layer in §B.1, the vortex circulation in §B.2 and the slope of a separated shear layer in §B.3.

B.1 Extracting the edge velocity of a shear layer

In §5.3.3 the edge velocity of the shear layer at the leading edge, u_{LE}, was needed to compute the leading-edge suction parameter, $\mathcal{L}$. A monitor line over which to extract the velocity profile was drawn in the chordwise direction, extending upstream far enough from the surface to cover the entire boundary layer. The thickness of the boundary layer is given by the distance from the wall to a point where the flow velocity has essentially the free stream velocity value. Its maximum value can be closely approximated by $\frac{\delta}{c} \approx \frac{5}{\sqrt{Re}}$, which for the current setup resulted in 5% of the total chord length. Over this reference line 100 equally spaced probes were positioned to compute the velocity (results obtained with 100 and 500 probes did not show significant differences). The tangential velocity, normal to this monitor line, was composed from the data recorded, and ultimately used to derive $\mathcal{L}$. Alternatively, other researchers calculated this parameter by integration of pressure distribution (Narsipur et al., 2020).

B.2 Extracting the circulation of a vortex

In §5.3.4 the strength of the leading-edge vortex was examined through its total circulation, Γ_{LEV}. The complex nature of vortices makes it difficult to give an unambiguous definition of what a vortex is (Haller, 2005; Jeong & Hussain, 1995). In the absence of universal consensus within the fluid mechanics community, several identification methods are available in the literature and exhaustively reviewed by Epps (2017). One of the most commonly adopted techniques to delimit vortices is the Q-criterion. Vortices are defined through positive levels of Q contours, with larger values for stronger vortices. Menon and Mittal (2021) demonstrated however that the effect on unsteady loading of strain-dominated regions surrounding rotational vortex cores (negative levels of Q contours) can be as important, and should not be carelessly ignored when studying vortex-dominated problems. In such scenarios there are some important phenomena to contemplate: the boundary-layer eruption caused by the advecting LEV above leads to fluid entrainment into the vortex; also the LEV interacts with the surrounding irrotational strain field. These vorticity transport mechanisms make it challenging to disentangle the contribution associated with swirl from that due to shear. Moreover, too low a threshold for the Q-criterion visualisation contour might result in large fluid regions identified as vortices without any physical significance. By comparison, neither the strain fluid surrounding vortices is simulated in the vortex method, nor the boundary layer is captured with the potential model it builds upon. In this sense, the strength of the LEV as defined in this work comes from only the vorticity generated at the separation point and transported through the shear layer, without alterations due to the earlier phenomena. It could therefore be more precise to think of it as the rate of circulation at the separation point, rather than the total strength of the vortex.

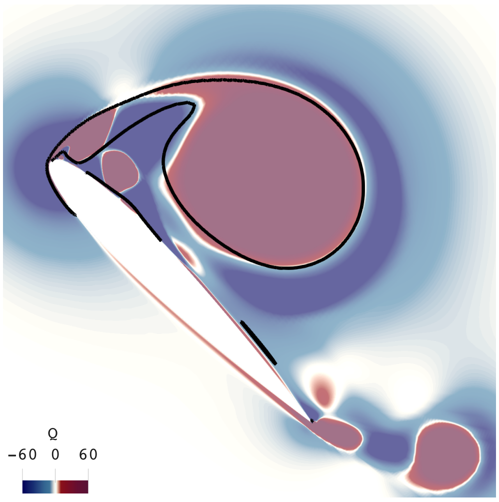

Figure B.1: Vortex boundary defined by iso-contour of vorticity (black line), encompassing rotational fluid (red contours) and strain fluid (blue contours).

To provide a meaningful comparison between the LOM and CFD, out-of-plane vorticity was filtered for the latter to only clockwise values (negative values); the bound vorticity, or layer over the upper surface, was masked; and an iso-contour of vorticity $\frac{\omega_z c}{U_\infty} = -7$ was taken as the boundary within which the circulation of the LEV, Γ_{LEV}, was computed. This contour, shown as a black line in Fig. B.1, contains vortical fluid (positive Q values) and entrained strain fluid (negative Q values) that progressively mix. This merge of rotational fluid and regions with zero vorticity is also seen in vortex rings (de Guyon & Mulleners, 2021), which are produced by many sea creatures, like squid or jellyfish, to propel themselves.

B.3 Extracting the slope of a shear layer

In §5.3.5 the slope of the separated shear layer at the leading edge, λ_{sl}, was introduced. Because the shear layer curves close to the leading edge, evaluation of this angle is inevitably influenced by the size of the fluid region considered. Hence, a direct comparison between modelling approaches requires the length of this area to be similar for both. In the low-order model the slope of the vortex sheet was estimated using the last two vortex particles released, with the distance between their cores observed to be within the range 0.01-0.02 chord lengths for all time steps. This is a physically reasonable value bearing in mind that $\Delta t^* = 0.015$

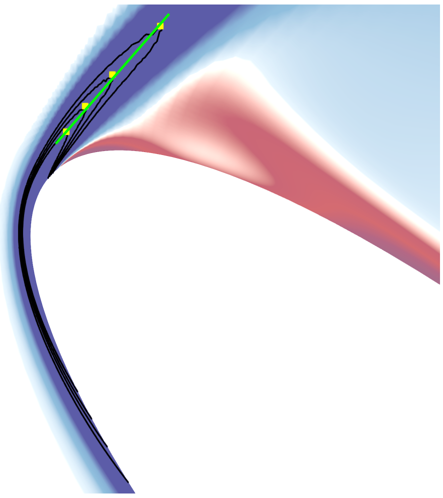

Figure B.2: Shear layer slope from CFD using linear regression. Black lines represent vorticity iso-contours, where yellow dots indicate the farthest point of the contour from the leading edge. The green line is fitted using these points to provide the slope.

in the simulations (see §3.2.2), and particles move with the free stream velocity, $U = 1$. The equivalent length of shear layer taken into account for CFD calculations should then be somewhere around 1% to 2% of the aerofoil's chord length. As a reference, the thickness of the NACA 0004 at one third of the chord is 4% of the chord length. Therefore, from one quarter to the half of this length makes a good approximation. Out-of-plane vorticity iso-contours spanning up to this length within the shear layer were traced. Linear regression was then applied over the furthest point of each contour from the leading edge, as exemplified in Fig. B.2, to calculate the shear layer angle.

The dry river-bed finds no thanks for its past.

— Rabindranath Tagore

Bibliography

Ajanic, E., Paolini, A., Coster, C., Floreano, D., & Johansson, C. (2022). Robotic avian wing explains aerodynamic advantages of wing folding and stroke tilting in flapping flight. *Advanced Intelligent Systems*, 2200148.

Akkala, J., & Buchholz, J. (2017). Vorticity transport mechanisms governing the development of leading-edge vortices. *Journal of Fluid Mechanics*, *829*, 512–537.

Alexander, D. (2015). *On the wing: Insects, pterosaurs, birds, bats and the evolution of animal flight*. Oxford University Press.

Alvarez, J., Meseguer, J., Meseguer, E., & Pérez, A. (2001). On the role of the alula in the steady flight of birds. *Ardeola*, *48*(2), 161–173.

Ansari, S., Żbikowski, R., & Knowles, K. (2006). Non-linear unsteady aerodynamic model for insect-like flapping wings in the hover. part 2: Implementation and validation. *Proceedings of the Institution of Mechanical Engineers, Part G: Journal of Aerospace Engineering*, *220*(3), 169–186.

Bechert, D., Bruse, M., Hage, W., & Meyer, R. (2000). Fluid mechanics of biological surfaces and their technological application. *Naturwissenschaften*, *87*(4), 157–171.

Beddoes, T. (1978). Onset of leading edge separation effects under dynamic conditions and low mach number. *34th Annual Forum of the American Helicopter Society*, *15*(17).

Benton, S., & Visbal, M. (2019). The onset of dynamic stall at a high, transitional reynolds number. *Journal of Fluid Mechanics*, *861*, 860–885.

Birch, J., & Dickinson, M. (2003). The influence of wing–wake interactions on the production of aerodynamic forces in flapping flight. *Journal of Experimental Biology*, *206*(13), 2257–2272.

Bird, H., Ramesh, K., Otomo, S., & Viola, I. (2021). Leading edge vortex formation on finite wings using vortex particles. *AIAA Scitech 2021 Forum*, 1196.

Birnbaum, W. (1924). Das ebene problem des schlagenden flügels. *ZAMM-Journal of Applied Mathematics and Mechanics/Zeitschrift für Angewandte Mathematik und Mechanik*, *4*(4), 277–292.

Bomphrey, R., Lawson, N., Harding, N., Taylor, G., & Thomas, A. (2005). The aerodynamics of manduca sexta: Digital particle image velocimetry analysis of the leading-edge vortex. *Journal of Experimental Biology*, *208*(6), 1079–1094.

Bomphrey, R., Taylor, G., & Thomas, A. (2009). Smoke visualization of free-flying bumblebees indicates independent leading-edge vortices on each wing pair. *Experiments in Fluids*, *46*(5), 811–821.

Borazjani, I., & Daghooghi, M. (2013). The fish tail motion forms an attached leading edge vortex. *Proceedings of the Royal Society B: Biological Sciences*, *280*(1756), 20122071.

Bottom II, R., Borazjani, I., Blevins, E., & Lauder, G. (2016). Hydrodynamics of swimming in stingrays: Numerical simulations and the role of the leading-edge vortex. *Journal of Fluid Mechanics*, *788*, 407–443.

Brücker, C., & Weidner, C. (2014). Influence of self-adaptive hairy flaps on the stall delay of an airfoil in ramp-up motion. *Journal of Fluids and Structures*, *47*, 31–40.

Campanile, L., & Sachau, D. (2000). The belt-rib concept: A structronic approach to variable camber. *Journal of Intelligent Material Systems and Structures*, *11*(3), 215–224.

Carr, L. (1988). Progress in analysis and prediction of dynamic stall. *Journal of Aircraft*, *25*(1), 6–17.

Carrell, S. (2022). Flying to the rescue: Scottish mountain teams are turning to drones. *The Guardian*. shorturl.at/bEOZ3

Carruthers, A., Thomas, A., & Taylor, G. (2007). Automatic aeroelastic devices in the wings of a steppe eagle aquila nipalensis. *Journal of Experimental Biology*, *210*(23), 4136–4149.

Carruthers, A., Walker, S., Thomas, A., & Taylor, G. (2010). Aerodynamics of aerofoil sections measured on a free-flying bird. *Proceedings of the Institution of Mechanical Engineers, Part G: Journal of Aerospace Engineering*, *224*(8), 855–864.

Chang, E., Matloff, L., Stowers, A., & Lentink, D. (2020). Soft biohybrid morphing wings with feathers underactuated by wrist and finger motion. *Science Robotics*, *5*(38), eaay1246.

Cheney, J., Rehm, J., Swartz, S., & Breuer, K. (2022). Bats actively modulate membrane compliance to control camber and reduce drag. *Journal of Experimental Biology*, *225*(14), 1–6.

Cheney, J., Stevenson, J., Durston, N., Maeda, M., Song, J., Megson-Smith, D., Windsor, S., Usherwood, J., & Bomphrey, R. (2021). Raptor wing morphing with flight speed. *Journal of the Royal Society Interface*, *18*(180), 20210349.

Chin, D., & Lentink, D. (2016). Flapping wing aerodynamics: From insects to vertebrates. *Journal of Experimental Biology*, *219*(7), 920–932.

Chorin, A. (1973). Numerical study of slightly viscous flow. *Journal of Fluid Mechanics*, *57*(4), 785–796.

Chorin, A., & Bernard, P. (1973). Discretization of a vortex sheet, with an example of roll-up. *Journal of Computational Physics*, *13*(3), 423–429.

Clements, R. (1973). An inviscid model of two-dimensional vortex shedding. *Journal of Fluid Mechanics*, *57*(2), 321–336.

Clements, R., & Maull, D. (1975). The representation of sheets of vorticity by discrete vortices. *Progress in Aerospace Sciences*, *16*(2), 129–146.

Colorado, J., Barrientos, A., Rossi, C., & Breuer, K. S. (2012). Biomechanics of smart wings in a bat robot: Morphing wings using sma actuators. *Bioinspiration & biomimetics*, *7*(3), 036006.

Cottet, G.-H., & Koumoutsakos, P. (2000). *Vortex methods: Theory and practice* (Vol. 8). Cambridge University Press.

Dalton, S. (1999). *The miracle of flight*. Firefly Books Ltd.

Darakananda, D., & Eldredge, J. (2019). A versatile taxonomy of low-dimensional vortex models for unsteady aerodynamics. *Journal of Fluid Mechanics*, *858*, 917–948.

de Guyon, G., & Mulleners, K. (2021). Scaling of the translational velocity of vortex rings behind conical objects. *Physical Review Fluids*, *6*(2), 024701.

Deparday, J., He, X., Eldredge, J., Mulleners, K., & Williams, D. (2022). Experimental quantification of unsteady leading-edge flow separation. *Journal of Fluid Mechanics*, *941*, A60.

Deparday, J., & Mulleners, K. (2019). Modeling the interplay between the shear layer and leading edge suction during dynamic stall. *Physics of Fluids*, *31*(10), 107104.

Dickinson, M., Lehmann, F.-O., & Sane, S. (1999). Wing rotation and the aerodynamic basis of insect flight. *Science*, *284*(5422), 1954–1960.

dos Santos, C., Rezaei, A., & Taha, H. (2021). Viscous extension of vortex methods for unsteady aerodynamics. *Physics of Fluids*, *33*(10), 103606.

Ekaterinaris, J., & Platzer, M. (1998). Computational prediction of airfoil dynamic stall. *Progress in Aerospace Sciences*, *33*(11-12), 759–846.

Eldredge, J., & Jones, A. (2019). Leading-edge vortices: Mechanics and modeling. *Annual Review of Fluid Mechanics*, *51*(1), 75–104.

Eldredge, J., Wang, C., & Ol, M. (2009). A computational study of a canonical pitch-up, pitch-down wing maneuver. *39th AIAA fluid dynamics conference*, 3687.

Ellington, C., Van Den Berg, C., Willmott, A., & Thomas, A. (1996). Leading-edge vortices in insect flight. *Nature*, *384*(6610), 626–630.

Epps, B. (2017). Review of vortex identification methods. *55th AIAA Aerospace Sciences Meeting*, 0989.

Epps, B., & Roesler, B. (2018). Vortex sheet strength in the sears, küssner, theodorsen, and wagner aerodynamics problems. *AIAA Journal*, *56*(3), 889–904.

Evans, W., & Mort, K. (1959). *Analysis of computed flow parameters for a set of sudden stalls in low-speed two-dimensional flow* (Vol. 85). National Aeronautics & Space Administration.

Fage, A., & Johansen, F. (1927). On the flow of air behind an inclined flat plate of infinite span. *Proceedings of the Royal Society of London*, *116*(773), 170–197.

Farin, G. (2014). *Curves and surfaces for computer-aided geometric design: A practical guide*. Elsevier.

Faure, T., Roncin, K., Viaud, B., Simonet, T., & Daridon, L. (2022). Flapping wing propulsion: Comparison between discrete vortex method and other models. *Physics of Fluids*, *34*(3), 034108.

Faure, T., Dumas, L., & Montagnier, O. (2020). Numerical study of two-airfoil arrangements by a discrete vortex method. *Theoretical and Computational Fluid Dynamics*, *34*(1), 79–103.

Feszty, D., Gillies, E., & Vezza, M. (2004). Alleviation of airfoil dynamic stall moments via trailing-edge flap flow control. *AIAA Journal*, *42*(1), 17–25.

Ford, P., & Babinsky, H. (2013). Lift and the leading-edge vortex. *Journal of Fluid Mechanics*, *720*, 280–313.

Freymuth, P. (1988). Propulsive vortical signature of plunging and pitching airfoils. *AIAA Journal*, *26*(7), 881–883.

Fuchiwaki, M., Kuroki, T., Tanaka, K., & Tababa, T. (2013). Dynamic behavior of the vortex ring formed on a butterfly wing. *Experiments in Fluids*, *54*(1), 1–12.

Gad-el-Hak, M. (2000). *Flow control*. Cambridge University Press.

Gerontakos, P., & Lee, T. (2006). Dynamic stall flow control via a trailing-edge flap. *AIAA Journal*, *44*(3), 469–480.

Gerontakos, P., & Lee, T. (2008). Piv study of flow around unsteady airfoil with dynamic trailing-edge flap deflection. *Experiments in Fluids*, *45*(6), 955–972.

Glauert, H. (1927). *Theoretical relationships for an aerofoil with hinged flap* (tech. rep.). HM Stationery Office.

Graftieaux, L., Michard, M., & Grosjean, N. (2001). Combining piv, pod and vortex identification algorithms for the study of unsteady turbulent swirling flows. *Measurement Science and Technology*, *12*(9), 1422.

Granlund, K., Ol, M., & Bernal, L. (2013). Unsteady pitching flat plates. *Journal of Fluid Mechanics*, *733*, R5.

Green, R., Gillies, E., & Wang, Y. (2011). Trailing-edge flap flow control for dynamic stall. *The Aeronautical Journal*, *115*(1170), 493–503.

Greengard, L., & Rokhlin, V. (1987). A fast algorithm for particle simulations. *Journal of Computational Physics*, *73*(2), 325–348.

Hald, O. (1979). Convergence of vortex methods for euler's equations. *SIAM Journal on Numerical Analysis*, *16*(5), 726–755.

Haller, G. (2005). An objective definition of a vortex. *Journal of Fluid Mechanics*, *525*, 1–26.

Hammer, P., Altman, A., & Eastep, F. (2014). Validation of a discrete vortex method for low reynolds number unsteady flows. *AIAA Journal*, *52*(3), 643–649.

Han, T., Mivehchi, A., Kurt, M., & Moored, K. (2022). Tailoring the bending pattern of non-uniformly flexible pitching hydrofoils enhances propulsive efficiency. *Bioinspiration & Biomimetics*, *17*(6), 065003.

Hang, H., Heydari, S., Costello, J., & Kanso, E. (2022). Active tail flexion in concert with passive hydrodynamic forces improves swimming speed and efficiency. *Journal of Fluid Mechanics*, *932*, A35.

Harbig, R., Sheridan, J., & Thompson, M. (2013). Relationship between aerodynamic forces, flow structures and wing camber for rotating insect wing planforms. *Journal of Fluid Mechanics*, *730*, 52–75.

Harvey, C., Gamble, L., Bolander, C., Hunsaker, D., Joo, J., & Inman, D. (2022). A review of avian-inspired morphing for uav flight control. *Progress in Aerospace Sciences*, *132*, 100825.

He, G., Deparday, J., Siegel, L., Henning, A., & Mulleners, K. (2020). Stall delay and leading-edge suction for a pitching airfoil with trailing-edge flap. *AIAA Journal*, *58*(12), 5146–5155.

Hirato, Y., Shen, M., Gopalarathnam, A., & Edwards, J. (2021). Flow criticality governs leading-edge-vortex initiation on finite wings in unsteady flow. *Journal of Fluid Mechanics*, *910*, A1.

Huang, Y., & Green, M. (2015). Detection and tracking of vortex phenomena using lagrangian coherent structures. *Experiments in Fluids*, *56*(7), 1–12.

Hubel, T., & Tropea, C. (2010). The importance of leading edge vortices under simplified flapping flight conditions at the size scale of birds. *Journal of Experimental Biology*, *213*(11), 1930–1939.

Hunsaker, D., Reid, J., & Joo, J. (2019). Geometric definition and ideal aerodynamic performance of parabolic trailing-edge flaps. *International Journal of Astronautics and Aeronautical Engineering*, *4*(1), 1–17.

Jafferis, N., Helbling, E., Karpelson, M., & Wood, R. (2019). Untethered flight of an insect-sized flapping-wing microscale aerial vehicle. *Nature*, *570*(7762), 491–495.

Jeong, J., & Hussain, F. (1995). On the identification of a vortex. *Journal of Fluid Mechanics*, *285*, 69–94.

Johansson, C., Wolf, M., Von Busse, R., Winter, Y., Spedding, G., & Hedenström, A. (2008). The near and far wake of pallas' long tongued bat (glossophaga soricina). *Journal of Experimental Biology*, *211*(18), 2909–2918.

Johnston, J., & Gopalarathnam, A. (2012). Investigation of a bio-inspired lift-enhancing effector on a 2d airfoil. *Bioinspiration & Biomimetics*, *7*(3), 036003.

Jones, K., Dohring, C., & Platzer, M. (1998). Experimental and computational investigation of the knoller-betz effect. *AIAA Journal*, *36*(7), 1240–1246.

Kamrani-Fard, K., Ngo, V., & Liburdy, J. (2021). A leading-edge vortex initiation criteria for large amplitude foil oscillations using a discrete vortex model. *Physics of Fluids*, *33*(11), 115123.

Katz, J. (1981). A discrete vortex method for the non-steady separated flow over an airfoil. *Journal of Fluid Mechanics*, *102*, 315–328.

Katz, J., & Plotkin, A. (2001). *Low-speed aerodynamics* (Vol. 13). Cambridge University Press.

Kissing, J., Kriegseis, J., Li, Z., Feng, L., Hussong, J., & Tropea, C. (2020). Insights into leading edge vortex formation and detachment on a pitching and plunging flat plate. *Experiments in Fluids*, *61*, 1–18.

Kiya, M., & Arie, M. (1977). A contribution to an inviscid vortex-shedding model for an inclined flat plate in uniform flow. *Journal of Fluid Mechanics*, *82*(2), 223–240.

Küssner, H. (1936). Zusammenfassender bericht über den instationären auftrieb von flügeln. *Luftfahrtforschung*, *13*(12), 410–424.

Kuwahara, K. (1973). Numerical study of flow past an inclined flat plate by an inviscid model. *Journal of the Physical Society of Japan*, *35*(5), 1545–1551.

Lee, S., Kim, J., Park, H., Jabłoński, P., & Choi, H. (2015). The function of the alula in avian flight. *Scientific Reports*, *5*(1), 1–5.

Lee, T., & Su, Y. (2011). Unsteady airfoil with a harmonically deflected trailing-edge flap. *Journal of Fluids and Structures*, *27*(8), 1411–1424.

Lehmann, F.-O., Wang, H., & Engels, T. (2021). Vortex trapping recaptures energy in flying fruit flies. *Scientific Reports*, *11*(1), 1–7.

Leishman, G. (2006). *Principles of helicopter aerodynamics*. Cambridge University Press.

Lentink, D., Dickson, W., Van Leeuwen, J., & Dickinson, M. (2009). Leading-edge vortices elevate lift of autorotating plant seeds. *Science*, *324*(5933), 1438–1440.

Leonard, A. (1980). Vortex methods for flow simulation. *Journal of Computational Physics*, *37*(3), 289–335.

Li, C., Dong, H., & Liu, G. (2015). Effects of a dynamic trailing-edge flap on the aerodynamic performance and flow structures in hovering flight. *Journal of Fluids and Structures*, *58*, 49–65.

Li, D., Zhao, S., Da Ronch, A., Xiang, J., Drofelnik, J., Li, Y., Zhang, L., Wu, Y., Kintscher, M., Monner, H. P., et al. (2018). A review of modelling and analysis of morphing wings. *Progress in Aerospace Sciences*, *100*, 46–62.

Liao, J., Beal, D., Lauder, G., & Triantafyllou, M. (2003). Fish exploiting vortices decrease muscle activity. *Science*, *302*(5650), 1566–1569.

Lighthill, M. (1973). On the weis-fogh mechanism of lift generation. *Journal of Fluid Mechanics*, *60*(1), 1–17.

Liu, Y., Cheng, B., Sane, S., & Deng, X. (2015). Aerodynamics of dynamic wing flexion in translating wings. *Experiments in Fluids*, *56*(6), 1–15.

Liu, Z., Lai, J., Young, J., & Tian, F.-B. (2017). Discrete vortex method with flow separation corrections for flapping-foil power generators. *AIAA Journal*, *55*(2), 410–418.

Lucas, K., Johnson, N., Beaulieu, W., Cathcart, E., Tirrell, G., Colin, S., Gemmell, B., Dabiri, J., & Costello, J. (2014). Bending rules for animal propulsion. *Nature communications*, *5*(1), 1–7.

Lugt, H. J. (1983). *Vortex flow in nature and technology.* John Wiley & Sons.

Maeda, M., Nakata, T., Kitamura, I., Tanaka, H., & Liu, H. (2017). Quantifying the dynamic wing morphing of hovering hummingbird. *Royal Society Open Science*, *4*(9), 170307.

Manar, F., & Jones, A. (2019). Evaluation of potential flow models for unsteady separated flow with respect to experimental data. *Physical Review Fluids*, *4*(3), 034702.

Mancini, P., Medina, A., & Jones, A. (2019). Experimental and analytical investigation into lift prediction on large trailing-edge flaps. *Physics of Fluids*, *31*(1), 013106.

Marais, C., Thiria, B., Wesfreid, J., & Godoy-Diana, R. (2012). Stabilizing effect of flexibility in the wake of a flapping foil. *Journal of Fluid Mechanics*, *710*, 659–669.

Martínez, A., He, G., Mulleners, K., & Ramesh, K. (2022). Modulation of the leading-edge vortex shedding rate in discrete-vortex methods. *AIAA SCITECH 2022 Forum*, 2416.

Maxworthy, T. (1979). Experiments on the weis-fogh mechanism of lift generation by insects in hovering flight. part 1. dynamics of the 'fling'. *Journal of Fluid Mechanics*, *93*(1), 47–63.

McCroskey, W. (1981). *The phenomenon of dynamic stall.* (tech. rep.). NASA.

McCroskey, W. (1982). Unsteady airfoils. *Annual Review of Fluid Mechanics*, *14*(1), 285–311.

Medina, A., & Hemati, M. (2021). Lift disturbance cancellation with rapid-flap actuation. *AIAA Journal*, *59*(11), 4367–4379.

Medina, A., Hemati, M., & Rockwood, M. (2020). Separated flow response to rapid flap deflection. *AIAA Journal*, *58*(4), 1446–1457.

Medina, A., Ol, M., Mancini, P., & Jones, A. (2017). Revisiting conventional flaps at high deflection rate. *AIAA Journal*, *55*(8), 2676–2685.

Menon, K., & Mittal, R. (2021). Significance of the strain-dominated region around a vortex on induced aerodynamic loads. *Journal of Fluid Mechanics*, *918*, R3.

Meseguer, J., & Sanz-Andrés, A. (2012). *Aerodinámica básica 2a edición.* Ibergarceta publications, SL.

Moore, D. (1971). *The discrete vortex approximation of a finite vortex sheet* (tech. rep.). California Institute of Technology.

Moulton, B., & Hunsaker, D. (2021). 3d-printed wings with morphing trailing-edge technology. *AIAA Scitech 2021 Forum*, 0351.

Mueller, T. (2001). *Fixed and flapping wing aerodynamics for micro air vehicle applications.* AIAA.

Muijres, F., Johansson, C., Barfield, R., Wolf, M., Spedding, G., & Hedenström, A. (2008). Leading-edge vortex improves lift in slow-flying bats. *Science*, *319*(5867), 1250–1253.

Muijres, F., Johansson, C., & Hedenström, A. (2012). Leading edge vortex in a slow-flying passerine. *Biology letters*, *8*(4), 554–557.

Muijres, F., Johansson, C., Winter, Y., & Hedenström, A. (2014). Leading edge vortices in lesser long-nosed bats occurring at slow but not fast flight speeds. *Bioinspiration & Biomimetics*, *9*(2), 025006.

Mulleners, K., & Raffel, M. (2013). Dynamic stall development. *Experiments in Fluids*, *54*(2), 1–9.

Munk, M. (1923). *General theory of thin wing sections* (tech. rep.).

Murray, R. O., & Gallego, A. (2017). A modelling study of the tidal stream resource of the pentland firth, scotland. *Renewable energy*, *102*, 326–340.

Nair, N., Flynn, Z., & Goza, A. (2022). Numerical study of multiple bio-inspired torsionally hinged flaps for passive flow control. *Fluids*, *7*(2), 44.

Narsipur, S. (2022). Effect of reynolds number and airfoil thickness on the leading-edge suction in unsteady flows. *Theoretical and Computational Fluid Dynamics*, *36*(5), 845–863.

Narsipur, S., Hosangadi, P., Gopalarathnam, A., & Edwards, J. (2020). Variation of leading-edge suction during stall for unsteady aerofoil motions. *Journal of Fluid Mechanics*, *900*, A25.

Neate, R. (2020). Drone deliveries soar in rural scotland during coronavirus outbreak. *The Guardian*. shorturl.at/BKOVY

Ol, M., Altman, A., Eldredge, J., Garmann, D., & Lian, Y. (2010). Resume of the aiaa fdtc low reynolds number discussion group's canonical cases. *48th AIAA Aerospace Sciences Meeting Including the New Horizons Forum and Aerospace Exposition*, 1085.

Ol, M., Eldredge, J., & Wang, C. (2009). High-amplitude pitch of a flat plate: An abstraction of perching and flapping. *International Journal of Micro Air Vehicles*, *1*(3), 203–216.

Polet, D., Rival, D., & Weymouth, G. (2015). Unsteady dynamics of rapid perching manoeuvres. *Journal of Fluid Mechanics*, *767*, 323–341.

Ramanathan, H., Narsipur, S., & Gopalarathnam, A. (2019). Boundary-layer characteristics at the onset of leading-edge vortex formation on unsteady airfoils. *AIAA Aviation 2019 Forum*, 3590.

Ramesh, K. (2020). On the leading-edge suction and stagnation-point location in unsteady flows past thin aerofoils. *Journal of Fluid Mechanics*, *886*, A13.

Ramesh, K. (2022). On satisfying the kutta condition in unsteady thin aerofoil theory. *arXiv preprint arXiv:2205.08647*.

Ramesh, K., Gopalarathnam, A., Edwards, J., Ol, M., & Granlund, K. (2013). An unsteady airfoil theory applied to pitching motions validated against experiment and computation. *Theoretical and Computational Fluid Dynamics*, *27*(6), 843–864.

Ramesh, K., Gopalarathnam, A., Granlund, K., Ol, M., & Edwards, J. (2014). Discrete-vortex method with novel shedding criterion for unsteady aerofoil flows with intermittent leading-edge vortex shedding. *Journal of Fluid Mechanics*, *751*, 500–538.

Ramesh, K., Granlund, K., Ol, M., Gopalarathnam, A., & Edwards, J. (2018). Leading-edge flow criticality as a governing factor in leading-edge vortex initiation in unsteady airfoil flows. *Theoretical and Computational Fluid Dynamics*, *32*(2), 109–136.

Ramesh, K., Murua, J., & Gopalarathnam, A. (2015). Limit-cycle oscillations in unsteady flows dominated by intermittent leading-edge vortex shedding. *Journal of Fluids and Structures*, *55*, 84–105.

Rennie, R., & Jumper, E. (1996). Experimental measurements of dynamic control surface effectiveness. *Journal of Aircraft*, *33*(5), 880–887.

Rennie, R., & Jumper, E. (1999). Gust alleviation using trailing-edge flaps. *37th Aerospace Sciences Meeting and Exhibit*, 649.

Rival, D., Kriegseis, J., Schaub, P., Widmann, A., & Tropea, C. (2014). Characteristic length scales for vortex detachment on plunging profiles with varying leading-edge geometry. *Experiments in Fluids*, *55*, 1–8.

Rosenhead, L. (1931). The formation of vortices from a surface of discontinuity. *Proceedings of the Royal Society of London*, *134*(823), 170–192.

Rosti, M., Omidyeganeh, M., & Pinelli, A. (2018). Numerical simulation of a passive control of the flow around an aerofoil using a flexible, self adaptive flaplet. *Flow, Turbulence and Combustion*, *100*(4), 1111–1143.

Saffman, P., & Baker, G. (1979). Vortex interactions. *Annual Review of Fluid Mechanics*, *11*(1), 95–121.

Saffman, P. (1995). *Vortex dynamics*. Cambridge University Press.

Samara, F., & Johnson, D. (2020). Dynamic stall on pitching cambered airfoil with phase offset trailing edge flap. *AIAA Journal*, *58*(7), 2844–2856.

Sanchez-Reyes, J., & Chacón, J. (2018). Nonparametric bézier representation of polynomial transition curves. *Journal of Surveying Engineering*, *144*(2), 04018001.

Sane, S. (2003). The aerodynamics of insect flight. *Journal of Experimental Biology*, *206*(23), 4191–4208.

Sane, S., & Dickinson, M. (2002). The aerodynamic effects of wing rotation and a revised quasi-steady model of flapping flight. *Journal of Experimental Biology*, *205*(8), 1087–1096.

Sarpkaya, T. (1968). An analytical study of separated flow about circular cylinders. *Journal of Basic Engineering*, *90*(4), 511–518.

Sarpkaya, T. (1975). An inviscid model of two-dimensional vortex shedding for transient and asymptotically steady separated flow over an inclined plate. *Journal of Fluid Mechanics*, *68*(1), 109–128.

Sears, W. (1941). Some aspects of non-stationary airfoil theory and its practical application. *Journal of the Aeronautical Sciences*, *8*(3), 104–108.

Sears, W. (1956). Some recent developments in airfoil theory. *Journal of the Aeronautical Sciences*, *23*(5), 490–499.

Sedky, G., Lagor, F., & Jones, A. (2020). Unsteady aerodynamics of lift regulation during a transverse gust encounter. *Physical Review Fluids*, *5*(7), 074701.

Shih, C., Lourenco, L., & Krothapalli, A. (1995). Investigation of flow at leading and trailing edges of pitching-up airfoil. *AIAA Journal*, *33*(8), 1369–1376.

Shyy, W., Aono, H., Kang, C.-k., & Liu, H. (2013). *An introduction to flapping wing aerodynamics* (Vol. 37). Cambridge University Press.

Shyy, W., Lian, Y., Tang, J., Viieru, D., & Liu, H. (2008). *Aerodynamics of low reynolds number flyers*. Cambridge University Press.

Shyy, W., & Liu, H. (2007). Flapping wings and aerodynamic lift: The role of leading-edge vortices. *AIAA Journal*, *45*(12), 2817–2819.

Spalart, P. (1988). Vortex methods for separated flows. *VKI, Computational Fluid Dynamics, Volume 1.*

Spalart, P., & Allmaras, S. (1992). A one-equation turbulence model for aerodynamic flows. *30th Aerospace Sciences Meeting and Exhibit*, 439.

Srygley, R., & Thomas, A. (2002). Unconventional lift-generating mechanisms in free-flying butterflies. *Nature*, *420*(6916), 660–664.

Su, X., Yin, Z., Cao, Y., & Zhao, Y. (2017). Numerical investigations on aerodynamic forces of deformable foils in hovering motions. *Physics of Fluids*, *29*(4), 041902.

Suresh-Babu, A., Medina, A., Rockwood, M., Bryant, M., & Gopalarathnam, A. (2021). Theoretical and experimental investigation of an unsteady airfoil in the presence of external flow disturbances. *Journal of Fluid Mechanics*, *921*, A21.

Suresh-Babu, A., Narsipur, S., Bryant, M., & Gopalarathnam, A. (2022). Leading-edge-vortex tailoring on unsteady airfoils using an inverse aerodynamic approach. *Physics of Fluids*, *34*(5), 057107.

Swanton, E., Vanier, B., & Mohseni, K. (2010). Flow visualization and wall shear stress of a flapping model hummingbird wing. *Experiments in Fluids*, *49*(3), 657–671.

Taha, H., & Rezaei, A. (2019). Viscous extension of potential-flow unsteady aerodynamics: The lift frequency response problem. *Journal of Fluid Mechanics*, *868*, 141–175.

Takami, H. (1964). *Numerical experiment with discrete vortex approximation, with reference to the rolling up of a vortex sheet* (tech. rep.). Stanford University.

Taylor, G., Nudds, R., & Thomas, A. (2003). Flying and swimming animals cruise at a strouhal number tuned for high power efficiency. *Nature*, *425*(6959), 707–711.

Theodorsen, T. (1935). *General theory of aerodynamic instability and the mechanism of flutter* (tech. rep.). National Advisory Committee for Aeronautics.

Thomas, A., Taylor, G., Srygley, R., Nudds, R., & Bomphrey, R. (2004). Dragonfly flight: Free-flight and tethered flow visualizations reveal a diverse array of unsteady lift-generating mechanisms, controlled primarily via angle of attack. *Journal of Experimental Biology*, *207*(24), 4299–4323.

Triantafyllou, G., Triantafyllou, M., & Grosenbaugh, M. (1993). Optimal thrust development in oscillating foils with application to fish propulsion. *Journal of Fluids and Structures*, *7*(2), 205–224.

Van Den Berg, C., & Ellington, C. (1997). The three-dimensional leading-edge vortex of a ‘hovering’ model hawkmoth. *Philosophical Transactions of the Royal Society of London. Series B: Biological Sciences*, *352*(1351), 329–340.

Van Dyke, M. (1964). *Perturbation methods in fluid mechanics* (Vol. 136). Academic Press.

Vatistas, G., Kozel, V., & Mih, W. (1991). A simpler model for concentrated vortices. *Experiments in Fluids*, *11*(1), 73–76.

Videler, J., Stamhuis, E., & Povel, G. (2004). Leading-edge vortex lifts swifts. *Science*, *306*(5703), 1960–1962.

Videler, J. (2006). *Avian flight*. Oxford University Press.

Von Busse, R., Hedenström, A., Winter, Y., & Johansson, C. (2012). Kinematics and wing shape across flight speed in the bat, leptonycteris yerbabuenae. *Biology open*, *1*(12), 1226–1238.

Von Karman, T., & Sears, W. (1938). Airfoil theory for non-uniform motion. *Journal of the Aeronautical Sciences*, *5*(10), 379–390.

Wagner, H. (1925). Über die entstehung des dynamischen auftriebes von tragflügeln. *Zeitschrift für Angewandte Mathematik und Mechanik*, *5*(1), 17–35.

Walker, S., Thomas, A., & Taylor, G. (2009). Deformable wing kinematics in the desert locust: How and why do camber, twist and topography vary through the stroke? *Journal of the Royal Society Interface*, *6*(38), 735–747.

Walker, S., Thomas, A., & Taylor, G. (2010). Deformable wing kinematics in free-flying hoverflies. *Journal of the Royal Society Interface*, *7*(42), 131–142.

Wang, C., & Eldredge, J. (2013). Low-order phenomenological modeling of leading-edge vortex formation. *Theoretical and Computational Fluid Dynamics*, *27*(5), 577–598.

Wang, J. (2005). Dissecting insect flight. *Annual Review of Fluid Mechanics*, *37*(1), 183–210.

Wang, S., Zhang, X., He, G., & Liu, T. (2014). Lift enhancement by dynamically changing wingspan in forward flapping flight. *Physics of Fluids*, *26*(6), 061903.

Wang, S., Zhang, X., He, G., & Liu, T. (2015). Lift enhancement by bats' dynamically changing wingspan. *Journal of the Royal Society Interface*, *12*(113), 20150821.

Warrick, D., Tobalske, B., & Powers, D. (2009). Lift production in the hovering hummingbird. *Proceedings of the Royal Society B: Biological Sciences*, *276*(1674), 3747–3752.

Weis-Fogh, T. (1973). Quick estimates of flight fitness in hovering animals, including novel mechanisms for lift production. *Journal of Experimental Biology*, *59*(1), 169–230.

Widmann, A., & Tropea, C. (2015). Parameters influencing vortex growth and detachment on unsteady aerodynamic profiles. *Journal of Fluid Mechanics*, *773*, 432–459.

Williamson, C., & Roshko, A. (1988). Vortex formation in the wake of an oscillating cylinder. *Journal of Fluids and Structures*, *2*(4), 355–381.

Willmott, A., Ellington, C., & Thomas, A. (1997). Flow visualization and unsteady aerodynamics in the flight of the hawkmoth, manduca sexta. *Philosophical Transactions of the Royal Society of London. Series B: Biological Sciences*, *352*(1351), 303–316.

Wolf, M., Johansson, C., Von Busse, R., Winter, Y., & Hedenström, A. (2010). Kinematics of flight and the relationship to the vortex wake of a pallas' long tongued bat (glossophaga soricina). *Journal of Experimental Biology*, *213*(12), 2142–2153.

Wolf, T., & Konrath, R. (2015). Avian wing geometry and kinematics of a free-flying barn owl in flapping flight. *Experiments in Fluids*, *56*(2), 1–18.

Woods, B., Bilgen, O., & Friswell, M. (2014). Wind tunnel testing of the fish-bone-active-camber morphing concept. *Journal of Intelligent Material Systems and Structures*, *25*(7), 772–785.

Woods, B., Dayyani, I., & Friswell, M. (2015). Fluid/structure-interaction analysis of the fish-bone-active-camber morphing concept. *Journal of Aircraft*, *52*(1), 307–319.

Woods, B., & Friswell, M. (2012). Preliminary investigation of a fish-bone-active-camber concept. *Smart Materials, Adaptive Structures and Intelligent Systems*, *45103*, 555–563.

Xia, X., & Mohseni, K. (2013). Lift evaluation of a two-dimensional pitching flat plate. *Physics of Fluids*, *25*(9), 091901.

Xia, X., & Mohseni, K. (2017). Unsteady aerodynamics and vortex-sheet formation of a two-dimensional airfoil. *Journal of Fluid Mechanics*, *830*, 439–478.

Xu, M., Wei, M., Li, C., & Dong, H. (2015). Adjoint-based optimization of flapping plates hinged with a trailing-edge flap. *Theoretical and Applied Mechanics Letters*, *5*(1), 1–4.

Yu, H.-T., & Bernal, L. (2017). Effects of pivot location and reduced pitch rate on pitching rectangular flat plates. *AIAA Journal*, *55*(3), 702–718.

Zhao, L., Deng, X., & Sane, S. (2011). Modulation of leading edge vorticity and aerodynamic forces in flexible flapping wings. *Bioinspiration & Biomimetics*, *6*(3), 1–7.

Zhao, L., Huang, Q., Deng, X., & Sane, S. (2010). Aerodynamic effects of flexibility in flapping wings. *Journal of the Royal Society Interface*, *7*(44), 485–497.

Zheng, L., Hedrick, T., & Mittal, R. (2013). Time-varying wing-twist improves aerodynamic efficiency of forward flight in butterflies. *PloS one*, *8*(1), e53060.

List of research outputs

Journal Articles

- Martinez, A., Mulleners, K. and Ramesh, K. (in preparation 2023). Vorticity feeding rate modelling: effect on vortex sheet dynamics. *Journal of Fluid Mechanics.*
- Martinez, A. and Ramesh, K. (in review 2023). Inviscid modeling of unsteady morphing airfoils using a discrete-vortex method. *Theoretical and Computational Fluid Dynamics.*

Conference Proceedings

- Martinez, A., He, G., Mulleners, K. and Ramesh, K. (2022). Modulation of the leading-edge vortex shedding rate in discrete-vortex methods. *AIAA SciTech Forum* (San Diego, CA, USA). DOI:10.2514/6.2022-2416.

Oral Presentations

- Martinez, A. and Ramesh, K. (2021). Modulation of leading-edge vortex shedding with chordwise deformation. *UK Fluids* (Southampton, UK – online).
- Martinez, A. and Ramesh, K. (2021). Bio-inspired flow control through camber morphing. *Scottish Fluid Mechanics Meeting* (Aberdeen, UK – online).
- Martinez, A. and Ramesh, K. (2019). Control of leading-edge vortex formation using trailing-edge flap deflection. *Advances in Aerospace Structures, Systems & Technology* (London, UK).

Posters

- Martinez, A. and Ramesh, K. (2022). Vortex-dominated flows around morphing bodies. *Colloquium on Vortex Dominated Flows – DisCoVor* (Villars-sur-Ollon, Switzerland).
- Martinez, A. and Ramesh, K. (2019). Deformable bodies for leading-edge vortices control. *Scottish Fluid Mechanics Meeting* (Dundee, UK).